DNA MEDIATED PARTICLE ADHESION

Christopher L. Porter

A DISSERTATION

in

Chemical and Biomolecular Engineering

Presented to the Faculties of the University of Pennsylvania

in

Partial Fulfillment of the Requirements for the

Degree of Doctor of Philosophy

2020

Supervisor of Dissertation

_ _____

John C. Crocker

Professor, Chemical and Biomolecular Engineering

Graduate Group Chairperson

- _____

John C. Crocker, Professor, Chemical and Biomolecular Engineering

Dissertation Committee

Scott Diamond, Arthur E. Humphrey Professor, Chemical and Biomolecular Engineering

Talid Sinno, Professor, Chemical and Biomolecular Engineering

Daniel A. Hammer, Alfred G. and Meta A. Ennis Professor, Bioengineering

DNA MEDIATED PARTICLE ADHESION

To mom and dad

Acknowledgments

I would like to thank my advisor, John, for providing guidance and advice throughout my experience at Penn. You really fostered a wonderful environment in our lab and always had good ideas and suggestions for ways I could tackle problems I encountered. I appreciate the way you always injected humor and passion into our work, and I looked forward to our meetings. I have grown a lot under your tutelage and thank you for giving me a great deal of freedom to explore my own interests in these projects. I would also like to thank my thesis committee, Scott, Talid, and Dan for providing guidance on my work along with suggestions and feedback on my progress.

I would also like to thank all the members of the Crocker lab, current and past who have provided advice, friendship, and just someone to vent to when I have been stuck in a rut. James McGinley mentored me when I first joined the lab and really helped me hit the ground running with my projects. Yifan Wang and Mehdi Molaei for always helping me and making coming to lab every day enjoyable. Working alongside them a huge benefit of this program. Thank you, Tae Soup Shim, for teaching me how to make nanoparticles and how to use the UV/Vis. I would also like to thank Ehsan Atefi, Clary Rodriguez, Steven Henry, Amruthesh Thirumalaiswamy, Jennifer Wang, Tianyu Liu, Charlie Tang and Andrew Langalis. I would also like to thank the Diamond lab for helping me and letting me work in their lab. Jason Rossi, Xinren and Richard Li really taught me everything I know about microfluidics and were a huge help in troubleshooting my problems in that area. Thanks also go out to Evan Tsiklidis, Brad Herbig, Chris Verni, Shu Zhu, Yichen Lu. And thank you to the Chenoweth lab for letting me use their equipment, especially Alex Kasznel and Sam Melton, and to the Pine Lab in New York for giving us a crash course on their process. I would also like to thank the CBE department.

I also need to thank all my teachers I had throughout the twenty plus years I have been in school. Mrs. Bowers sparked my interest in math, and everyone loves candy Friday. Your class really was the first time I considered going to school for engineering. Dr. Zawacky, thank you for

putting up with me in your chemistry class. Professor Snyder, thank you for introducing me to research at Bucknell and providing great mentorship and guidance when I was thinking about going to graduate school. Without you, I do not know if I ever would have gotten into computer programming. Professor Gross, Professor Raymond, Professor Prince, Professor Vogel, Professor Waka, Professor Jablonski, and Professor Csernica for making the chemical engineering department so fun. Looking back, I would not be where I am without all the lab experience and problem-solving skills you all put into the curriculum. I also need to thank the math and chemistry departments at Bucknell, and my professors at Penn.

I also need to thank my friends for supporting me throughout this process and providing me an escape when I need it. Chang, Mozur, Jonzy, and Paul, always look forward to hanging out with you guys back in Pittsburgh. Kemley thanks for letting me come crash in DC on occasion and teaching me a thing or two in Smash Bros. To the Philly friends, Sean and Ellie, Kathleen, Jim, Scott and Megan, and Amy and Better, thanks for keeping me sane. Had a great time exploring this city with you all. Also, thanks to the rugby team for giving me an outlet to release some aggression. Go Hogs! And thank you to the Rothsteins for being so welcoming and inclusive even when Judson was not around.

Lastly, I want to thank my family for all the support and love you have given throughout the years. Jamie, Judson, Sarah, and Hannah, I always look forward to coming home over the holidays and binging board games with you guys and hanging with your kids has been a welcome respite from school. Mom and Dad, you guys have been the best parents I could have asked for. Thanks for always pushing me, supporting me, and helping me navigate whatever life throws at me. It has really a huge comfort to know you have my back and are always there when I need help with anything. I love you all.

ABSTRACT

DNA MEDIATED PARTICLE ADHESION

Christopher L. Porter

John C. Crocker

Many biological systems exhibit cell or particle adhesion to other cells and substrates through discrete multivalent ligand bridges. These systems are inherently complex as they exist at the intersection of fluid dynamics, cell-signaling pathways, reaction kinetics, and force extension response of the bridges. The interplay of these factors can lead to a range of behaviors including free advection, strong adhesion, and intermittent regimes where the particles bind transiently or roll along the surface at a nonzero velocity significantly less than the free stream velocity. Here, we study the underlying physics of such systems using a dual experimental and computational modeling approach. Experimentally, we develop a cell free microfluidic system where DNA functionalized plastic beads are perfused over a complementarily DNA functionalized glass surface. By tuning the DNA thermodynamics of the system and shear rate, we can elicit a variety of particle responses. In one instance, we use a strong binding DNA system to study the monolayer deposition of particles in a flow field, discovering that the particle-particle collision hydrodynamics play a key role in the kinetics and morphological structure of the monolayer. Then, by using more weakly binding DNA systems, we find a regime in shear rate where particles transition from strongly adhered, to rolling, to freely advecting. We then use simulations to model the

rolling system and to understand the particle-to-particle variation seen in the experiments. We find that the model predicts the experimental results well, capturing not only the domain where rolling is found and the particle rolling velocity, but also the lateral diffusivity caused by the stochastic formation and rupture of DNA bridges and the distribution of rolling velocities of an individual particle. This model illuminates potential sources of particle-to-particle variation seen in the experiment, particularly in the sensitivity of rolling velocity to particle-to-wall distance. Together, these results further our understanding of adhesion through multivalent ligand binding and will help in the engineering and design of new systems.

Table of Contents

List of Tables

List of Illustrations

Chapter 1 Introduction

1.1 Sticky Particles in Flow Fields

Flows containing particles which are adhesive either to the surface which they flow over, or to each other appear in a wide range of scientific and natural problems. In biology, such systems are evident in clot formation (1), leukocyte migration (2), and liposomal targeted drug delivery (3). In these instances, it is important that the particles adhere and aggregate only at an appropriate location and time and not everywhere. Clots should only form at sites of blood vessel damage, leukocytes should migrate to sites of infection, and drugs should be delivered where they can provide a therapeutic benefit. These systems discriminate between surfaces through ligand-receptor binding modality, where ligands on the cell or particle surface bind to receptors presented by the surface they bind to.

These problems are fundamentally challenging to understand completely because they combine fluid dynamics (often in a time varying manner), complex biological intercellular and intracellular signaling pathways, deformable cell membranes and morphological changes. George Bell (4) developed a theoretical framework for understanding the thermodynamics of cell-to-cell and cell-to-surface adhesion. In his formulation, the adhesion is mediated by the reversible binding of ligand-receptor pairs. His model includes the ligand and receptor concentrations and the relevant reaction

rates to predict the force required to peel a cell from a surface. One of the key features of the model is the inclusion of the force induced unbinding rate of the molecular bridge, modeled using $k_b = k_b^O * \exp(\gamma F/k_B T)$, where k_b, is the unbinding rate, k_b^O is the unforced unbinding rate, F is the force exerted on the bridge, $k_B T$ is the Boltzmann constant, and γ is the reactive compliance, an empirically derived parameter related to the distance to the transition state. Evans (5, 6) extended this model to apply to single molecule dynamic force spectroscopy experiments.

Dembo and Bell (7) considered several variations of the original thermodynamic model, including multiplicity of receptors (multiple types of bridges being formed with their own kinetics and force sensitivity) and elastic deformation of the cell. Dembo and Hammer (8) introduced the idea of “slip” and “catch” bonds. In the case of slip bonds, the reactive compliance is positive, such that a force exerted on the bond accelerates its rupture. For a catch bond, the reactive compliance is negative, so that forces exerted on the bond stabilize it. Dembo (9) showed that for systems containing catch bonds, the adhesion of a cell cannot be reversed by the application of force. Lauffenberger and Hammer (10) extended the models further to include the kinetics of the system. They predicted the presence of different regimes of adhesiveness, the rate-controlled regime, where adhesion was controlled by the rate of initial bridge formation, and the affinity-controlled regime, were it is the total strength of the bonds that determines if a cell will adhere.

Experimentally, there have been many studies on the adhesion of cells and particles to surfaces through ligand-receptor binding. Parallel plate assays were done to study the effect of shear rate on neutrophil adhesion (11). Chromatographic techniques have been used to separate subpopulations of cells based on their adhesion characteristics (12). Additionally, cell-free assays have been developed (13-15) using a variety of microfluidic channel geometries and biomolecules to explore this class of problem. However, due to the inherent complexity of these systems, and large number of parameters in the experimental systems with known values of varying degrees of certainty, the bridging between experimental and model results has remained a challenge.

1.2 Adhesive Dynamics

One well-developed method for modeling and studying the adhesion of cells and particles to surfaces through discrete ligand-receptor bridges is adhesive dynamics. Initially used to study leukocyte rolling behavior (16), adhesive dynamics has expanded to include blood cells (17, 18), viruses (19), and cell-free models (20).

In these models a cell or particle is represented with its hydrodynamics being a function of the particles shape and orientation and distance to other solid surfaces, described by a mobility matrix. The mobility matrix considers the drag on the particle, which can vary depending on how far the particle is from surface, and its orientation to the surface, and includes the force and torque couplings. For the case of a spherical

particle, the solutions to the hydrodynamics of a particle near a planar wall were solved by Goldman, Cox and Brenner, (21-23), while De Corato (24) described a methodology for determining the hydrodynamic response of an arbitrarily shaped solid. Additionally, the De Corato methodology solved the Langevin equation to determine the Brownian rotational and translational motion for an arbitrary shaped particle near a wall.

The particle and nearby surface are coated in complementary ligands, and the binding kinetics can be determined based on the local ligand concentration fields. Then, bridges can stochastically form between the particle and surface, with the location of the bridge being known explicitly. Once formed, the bridges exert forces and torques on the particle, affecting its motion. Additionally, these models include the force induced rupturing of the bridges, typically using Bell's model. In this way, particle trajectories are stochastically generated by Euler stepping the system, and at each time point, recalculating the mobility matrix, the forces and torques on the particle, and the formation and rupture of bridges.

While this methodology is more computationally intensive than a model which would include the bridges as an energy potential, it is powerful in its ability to capture the behavior of systems in which a small number of binding events dictate the systems behavior.

1.3 DNA as a Model Ligand

As mentioned, in the case of cell adhesion, intra and inter cellular signaling, and unknown ligand properties make it challenging to compare model and experimental results. For this reason, it is desirable to use a ligand with well-known properties. In this thesis we use deoxyribonucleic acid (DNA) as a model ligand to study the underlying physics of adhesive particles in a shear flow. DNA is a polymer composed of repeating nucleotides, with each nucleotide consisting of a phosphate sugar backbone and a nucleobase linked to the sugar group (25, 26). There are four types of nucleotides, adenine (A), thymine (T), cytosine (C), and guanine (G). When two single stranded DNA molecules come together, they can bind to each other through the hydrogen bonding of the nucleobases, which generally follow the rules of A's binding to T's and C's binding to G's, known as Watson-Crick base pairing, which makes it remarkably designable. This binding of two single stranded DNA molecules forms the famous double helix structure discovered by Watson and Crick (27).

Because of the important role DNA plays in biology as a genetic information carrier, its thermodynamic, kinetic, and structural properties have been studied extensively. For the short base pair overlaps used in this thesis (<20 base pairs), the thermodynamics of DNA is typically considered as a two-state model, with one state being two single stranded DNA molecules, and the second state being the fully hybridized double stranded DNA complex, ignoring any partially hybridized states. Using

this two-state model, SantaLucia and others (28-31) measured the thermodynamic properties (ΔG, ΔS, ΔH) of many DNA strands, and used this data to fit a thermodynamic model, known as the nearest neighbor model, to predict the thermodynamic properties of any arbitrary DNA strand. In this model the Gibb's Free Energy (ΔG) of hybridization is computed by summing over the strands individual base pair, with that base pair's contribution being dependent on its nearest neighbor nucleotides. In this way, the ΔG of hybridization is dependent both on the A, T, G, C composition and the specific order in which these bases appear. Additionally, this model incorporates the temperature and ionic concentration dependence of the hybridization energy. In general, this model accurately predicts the ΔG within 4%. This high degree of predictability makes DNA an attractive model molecule as its equilibrium properties can be designed for a priori, and then tuned further with the salt concentration, making it highly engineerable, a property taken advantage of extensively in self-assembly applications, particularly DNA origami (32, 33).

The binding kinetics of DNA have also been studied extensively. These measurements are typically done using DNA strands to which one is modified with a terminal fluorescent group, and its complement is modified with a terminal quencher group (34). Then, the overall fluorescence is measured, and as the strands hybridize, and the quencher comes into proximity with the fluorophore, the fluorescence decreases, allowing for the single strand and double strand concentrations, and thus the hybridization kinetics, to be calculated over time. Our group has used a different

approach for measuring the DNA hybridization kinetics (35). In this method, plastic microspheres where coated with complementary single stranded DNA, allowing for the microspheres to interact and bind to each other through the DNA hybridization. Then using an optical tweezers, two complementary particles where held near each other and their separation was measured. In the unbound state, the particles were free to diffuse away from each other, but in the bound state, where DNA bridges were formed, the particles were forced to be in contact. Using the known DNA densities and the lifetimes of the bound states, the overall DNA hybridization rate constant was able to be inferred, agreeing with previous methods of measurement. This indicates that in general, the DNA strand being tethered to a surface, in this case the particles, does not significantly affect its reactivity.

As DNA is a polymer, many of the same results from polymer physics have been applied to DNA. Several methods have been used to measure the persistence length and force extension curves of both single and double stranded DNA. In one method, fluorescence recovery after photobleaching experiments were done using fluorophore modified single stranded DNA of various lengths (36). This method allowed the authors to determine the diffusivity of the single stranded DNA molecule. Then assuming an Einstein diffusivity, the radius of gyration of the molecules and the persistence length of the molecule were calculated. Using this data, they found that the persistence length of DNA was effectively the sum of two terms: the intrinsic rigidity of the chain, and an electrostatic contribution, which is strongly dependent on the solution's ionic strength.

Otherer groups have used single molecule force spectroscopy measurements to probe the force extension curve of ssDNA (37, 38). In these studies, they found that ssDNA could be modeled well using either the freely jointed chain model with an added stretching modulus, or by using the worm like chain model. Again, they also found the force-extension curve to be dependent on the solution's ionic strength. Interestingly, they found that at extremely high salt concentrations, the models failed, speculating this is due to possible hairpin formation, while at extremely low salt conditions, the model also fails, perhaps due to excluded volume effects. Complementary studies of dsDNA found similar results, showing that dsDNA can be modeled well using the worm like chain model (37, 39, 40), however because of the double helix formation in dsDNA, it has a persistence length of ~10 times that of its single stranded counterpart. There have also been experiments probing the force required to scission the DNA molecule itself, with results ranging from ~100 pN to 2000 pN depending on the loading rate and solvent factors (41, 42).

There have also been studies to probe the force induced melting of DNA, that is, how much force is required to cause a dsDNA molecule to dehybridize into its ssDNA constituents. These studies have been done using DNA hairpins (43) and atomic force microscopy (44-47), and DNA functionalized microbeads (14, 15). These experiments showed that the force induced dehybridization of DNA could be modeled using Bell's model (4, 7), where the rate of dehybridization is an exponential function of the force, and the scaling factor is a linear function of the degree of base pair overlap.

Since DNA has been so well studied; its kinetics, thermodynamic, and behavior under force have been experimentally measured and modeled well, it makes for an ideal molecule to use for studying the underlying physics of various systems. Additionally, its high degree of selectivity and predictability in binding, i.e. strands bind strands with complementary sequences, makes it easy to engineer a system with. On top of this, short (<100 BP) are commercially available, with companies able to synthesize any arbitrary sequence with various modifications to allow for the covalent linking of the DNA strand to a wide array of surfaces. For these reasons, throughout this thesis, we use DNA for our studies.

1.4 Microfluidic Devices

Microfluidics are fluidic systems in which the height or width of the channel is on the order of 1-1000 microns, through which fluids can be pumped through. For a detailed review of microfluidic devices and some of their applications I suggest the reviews by George Whiteside (48), Glenn Walker (49) and Gadegaard (50). Briefly, microfluidic devices have been used in a variety of applications and have promised to revolutionize how much of biology is done, with so called labs-on-a-chip. Microfluidics offer several benefits for experimentation that we take advantage of in this thesis. Firstly, microfluidic devices can be easily fabricated. Typically, a device can be designed on a computer using computer-aided design (CAD) software, and the design sent to commercial companies to produce a SU-8 master wafer using photolithographic

techniques. Using this master, a polydimethylsiloxane (PDMS) device can be created using soft lithography techniques, resulting in a device with high fidelity to the original design. Using this method for producing devices is quick (devices take a couple hours to make once a master is acquired), relatively cheap (the master can be used repeatedly), the device self-seals to a glass slide (and can be plasma treated or designed to allow for vacuum sealing if required), and is transparent allowing for microscopy and data acquisition throughout the experiment. Additionally, because of the small geometries involved in these devices, the flow dynamics during experiments can be modeled well using laminar flow and other models (Reynold's Number <<1). For these reasons, throughout this thesis, we use microfluidic devices to study different experimental systems.

1.5 Thesis Overview

In this thesis we aim to study the underlying physics surrounding particle adhesion using a model system composed of microspheres grafted with single stranded DNA which are perfused over a glass slide grafted with commentary single stranded DNA. Through the DNA hybridization reaction, the particles interact with the glass slide and, depending on the experimental design can either bind firmly to the slide, or roll along the surface. In Chapter 2 we explore the monolayer deposition of particles onto a surface in a shear flow. For this experiment, we design a DNA architecture which allows for particle-to-glass binding as well as particle-to-particle interactions which can be

turned on and off via a “blocker” DNA strand. Having the particle-to-particle interactions turned off, we observe the kinetics of particle deposition and the overall structure of the resulting monolayer. We observe a reduced likelihood of particles to deposit directly behind an already deposited particle, and that this “depleted region” becomes more pronounced with increasing shear rate. This suggests a breaking of the time-symmetry for a particle flowing over another particle, despite the low Reynold’s number flow used. Then, our collaborators created several Brownian dynamics simulations with various effects included to model the experiment. We found that the model could only capture the experimental results kinetically and structurally if the particle-to-particle collision hydrodynamics were accurately included.

In Chapter 3 we explore why the system used in the monolayer experiments was not successful when being used for multilayer “clotting” experiments. In those experiments, the particles were again perfused through a channel, and allowed to bind to the glass. However, in this case, once a particle was stuck to the surface, its particle-particle interactions were turned on by removing the blocker strand, in theory, allowing for the capture of free stream particles, and thus build up the aggregate on the surface. However, we did not observe any significant aggregate formation in flow conditions, despite the particles ability to form aggregates on our temperature-controlled microscope. We evaluate several potential sources for this failure, including the DNA bridges being not being strong enough to sustain particle-to-particle binding in a shear flow, the DNA bridges not being turned on effectively, and the kinetics of the particle-

to-particle interaction. It was determined that the failure of this system was due to "self-quenching" of the particle once its particle-to-particle interactions were turned on. That is, once the blocker strand was removed, the DNA on the particle formed long lived loops, rather than being available to form bridges with a passing particle. We then propose a new formulation of the particles, considering this self-quenching aspect, which may allow for future experimental success.

In Chapter 3 we present the first DNA mediated rolling system. In this experiment, two DNA systems were designed to promote particle rolling along a surface, with the force exerted on the particle by the surface-to-particle DNA bridges causing the particle to move along the surface at ~1-10% of the free stream velocity. One of these systems was designed such that the overlap between the DNA strands was in line with the overall particle-to-surface bridge, while the other system had the overlap orthogonal to the bridge. In this way, we investigated the effect of the direction of the applied force on the DNA dehybridization reaction. We adhesive dynamics simulations to model the experimental system, and find the model is able to capture the behavior of the system, including at which shear rates the particles adhere firmly, roll, or freely advect along the surface, the particle diffusivity, and the distribution of rolling velocities for a single particle. Additionally, we note a high degree of particle-to-particle variation in the mean rolling velocity. Using the model, we propose potential explanations for this variation.

In Chapter 5 we discuss the adhesive dynamics model used in Chapter 4 in more depth. Here we present the hydrodynamic characteristics of the model, including the effect of the particle to wall separation on the particles free stream velocity and diffusivity. We also discuss the effect of including the DNA steric repulsive force and Van der Waals force on the particle and confirm that the Brownian particle obeys the detailed balance. We also present the method for determining the location of the DNA bridge anchor points, the model used for determining the force-extension curve of the DNA bridges, and the resulting dehybridization kinetics using Bell's model.

In Chapter 6 we discuss some of the side projects I conducted on methods for attaching single stranded DNA to various surfaces. We first discuss the swell-deswell method for grafting DNA onto polymer microspheres. In this method, the DNA is covalently linked to a di-block copolymer which is then adsorbed onto the surface of the particle. We present results on the kinetics and final DNA density using this method and find that the density is dependent on the solution's ionic strength. We then discuss the method for binding disulfide modified DNA to gold nanoparticles. We studied the effect of the solution's ionic strength, pH, and DNA strand length, finding that each of these can be used to control the final DNA density. Finally, we discuss various methods of attaching DNA to glass. However, despite trying many different methods for grafting DNA to glass, we always had difficulty in achieving a high availability of the DNA for binding, that is, only ~10-20% of the DNA that was bound to the glass was available to hybridize with soluble DNA strands, or the DNA on our particles. We discuss Shi et al's

(51) use of molecular dynamics and other experimental studies who found that DNA has an intrinsic propensity to bind to glass nonspecifically, through several different mechanisms. However, we propose a variation of our preferred method, which may in the lead to higher DNA availability in future experiments.

Chapter 7 presents a review of directed self-assembly using directional interactions that John and I wrote. While most of this thesis is regarding the use of experimental systems to study shear flow systems, much of the technology we used for these experiments has been used in colloidal and nanoparticle self-assembly applications. We discuss results from theory and simulation on what types of structures are possible if appropriate building blocks were available. We then discuss some of the experimental efforts to create new libraries of building blocks and their subsequent use in creating super structures.

Finally, in Chapter 8 we conclude with a discussion of the results of this thesis and its meaning in the field. Additionally, we will suggest some future directions that may be of interest for subsequent research efforts.

Chapter 2 Deposition of sticky spheres in channel flow: Modeling of surface coverage evolution requires accurate sphere-sphere collision hydrodynamics

This chapter is adapted from article: Lee YK, Porter C, Diamond SL, Crocker JC, Sinno T. Deposition of sticky spheres in channel flow: Modeling of surface coverage evolution requires accurate sphere-sphere collision hydrodynamics. Journal of Colloid and Interface Science. 2018;530:383-93. https://doi.org/10.1016/j.jcis.2018.06.097

2.1 Abstract

We analyzed the role of hydrodynamic interactions in a microfluidic channel flow containing a dilute suspension of micron-scale colloidal spheres (0.03%, 0.1%, 0.3% volume fraction) engineered to adhere onto a collector patch on the channel wall at wall shear rates of 9.3 to 930 s^{-1}. Particle-wall adhesion was mediated by single-stranded DNA oligomers grafted onto the spheres and the glass channel wall, producing well-defined interactions via DNA strand base pairing. Particle positions in the flow were evolved using Brownian dynamics simulations in which hydrodynamic interactions between moving particles and the channel walls and/or adhered particles were computed off-line using a series of local simulations that explicitly resolve the fluid flow at the particle scale. By systematically varying the nature of hydrodynamic interactions captured in the Brownian dynamics simulations, we find that the interactions between

moving and adhered particles represents the single most important physical element in such models. Once captured sufficiently accurately, the resulting models are able to predict coarse variables such as the overall particle coverage evolution, as well as more subtle characteristics, such as the microstructural distribution of the adhered particles.

2.2 Introduction

Particulate flows are ubiquitous in a large number of natural and technological settings. An important sub-class of particle-containing flows are those in which colloidal particles (i.e., with sizes in the range of tens of nanometers to a few microns) adhere to and become deposited onto surfaces in contact with the flow. Colloidal particle deposition on surfaces is a key aspect of applications and phenomena such as fluid filtration (52, 53), microelectronic device processing (54), biofilm formation and fouling in pipes (55, 56) and medical devices (57, 58), and platelet aggregation/clot formation in blood flow (59, 60). Although the flow conditions, surface chemistry, and particle type, size, and volume fraction, lead to deposition kinetics and deposited layer morphology that differ substantially across specific instances (e.g., (59, 61, 62)), it is generally the case that such systems are essentially defined by particle-wall and particle-particle interactions. Such interactions usually include Van der Waals attraction and repulsive electrostatic repulsion due counter-ion double layer formation. In addition, particles and/or wall surfaces may be intentionally functionalized with oligomeric or polymeric species, e.g., engineered single-stranded DNA, which are designed to induce additional

(usually attractive) interactions. Finally, hydrodynamic correlations between particles and with confining walls mediated by disturbances in the surrounding fluid introduce additional interactions that may strongly modify the deposition process—these interactions may be effectively attractive or repulsive (63-66).

Colloidal particle deposition flows have been studied extensively with experiments and in simulation; a detailed exposition of both aspects is provided in Elimelech et al. (64). Traditionally, these analyses have been performed in a parallel flow channel (61, 66, 67), an impinging jet cell (68), or a rotating disc system (69, 70) because of the well-defined flow geometries and consequent relative ease of analytical treatment. In this paper, we consider a microfluidic parallel channel geometry originally developed for studying thrombosis in blood, where platelets become activated and stick to a well-defined and discrete patch of collagen on one of the channel walls (59, 71, 72). Although this apparatus has successfully provided quantitative measures of thrombosis in a variety of settings, modeling and simulation of the system is challenging because of the highly complex nature of platelet morphology and activity, the coupling to a complex biochemical reaction network, and the complex hydrodynamic forces generated by a high density of deformable red blood cells (59, 73-75). Here, we use the same parallel channel flow geometry to study a system in which the particles are micron-sized, rigid spherical plastic beads that have been functionalized with a polymer brush comprised of single-stranded DNA (ss-DNA) oligomers and dispersed in an aqueous solution (76-78). The ‘collector’ in this experimental model is an area of the

glass channel wall that has been functionalized with single-stranded DNA oligomers that are partially complementary to the strands on the particles—enabling DNA base pairing to create tethers between moving particles and the wall; further details are provided in Section 2.3 . Although we restrict our analysis to a single layer of adhered particles—the ss-DNA oligomers on the particles used in this study are designed to hybridize only with those on the glass wall and not with those on other particles—the system is easily modifiable to accommodate inter-particle adhesion and the formation of multilayered structures.

A large number of modeling and simulation approaches have been developed for simulating particulate flows, each with their own fidelity and computational characteristics. These are far too numerous to summarize comprehensively here but a number of excellent reviews exist on various classes of methods and their applications to specific types of particulate flows; e.g., see Refs. (79-82). In the present study, we focus on so-called Lagrangian simulation approaches, where particle dynamics are described by Langevin equations that can explicitly account for inter-particle and particle-wall forces, the background fluid flow, hydrodynamic interactions, and Brownian fluctuations. Very broadly, these approaches invoke a simplified representation of the hydrodynamic interactions between particles and therefore avoid the need to compute a particle-resolved flow across the entire domain, which becomes prohibitive for large systems and long times. This type of approach has been employed in several previous studies of flows with colloidal particle deposition on surfaces; a

comprehensive discussion of this technique and its application to flows with particle deposition on surfaces is provided in Elimelech et al. (64). Examples of Brownian dynamics simulations of depositing particle flows include the work of Unni and Yang (61), who considered deposition in a parallel-plate channel, and Jung et al. (83), who studied particle deposition on a permeable, corrugated membrane. In both studies, a background, steady flow field was specified externally that provided a convective force on the particles. Unni and Yang, who considered a parabolic flow, introduced analytical hydrodynamic corrections to this flow profile to account for particle-particle and particle-wall interactions; similar corrections were applied to the particle diffusion coefficients. By contrast, the more complex (Stokes) flow considered by Jung et al. was solved numerically, but inter-particle and particle-wall hydrodynamic interactions were neglected. In both cases, non-hydrodynamic inter-particle and particle-wall interactions were modeled according to DLVO (Derjaguin-Landau-Verwey-Overbeek) theory.

In this paper, we employ a similar Lagrangian computational strategy to those in Refs. (61, 83), with some important distinguishing features designed to take advantage of the DNA-functionalized particle system. Most significantly, our DNA-hybridization mediated interactions simplify the description of the non-hydrodynamic particle-particle and particle-wall interactions, enabling us to focus on the hydrodynamic ones. We consider a sequence of models with increasing fidelity in the description of the hydrodynamic interactions between moving particles and the channel wall with and without adhered particles. By systematically 'titrating' model fidelity, we find that an

accurate description of the hydrodynamic interactions between a single moving particle and a single adhered particle is the single strongest factor in obtaining a comprehensive model for particle deposition in channel flow. Significantly, using the Lagrangian approach, a high level of model performance may be obtained without the need to resolve the flow at the particle scale across the entire simulation domain.

The remainder of the paper is organized as follows. The experimental system is described in Section 2.3 , along with the details of the DNA oligomer design strategy and particle/glass functionalization methods. In Section 2.4 , the overall computational strategy is described in detail, along with a discussion of the various levels of model fidelity used to simulate the experiments. Results are presented in Section 2.5 for each of the models and comparisons to the experimental measurements are analyzed. Finally, conclusions are presented in Section 2.6 .

2.3 Experimental Methods

2.3.1 DNA Design for Sticky Sphere Interactions.

For this experiment, we require single-stranded DNA oligonucleotides which are chemically bonded to the microspheres and to the microchannel wall. Minimally, two distinct species of interacting DNA strands would suffice to drive binding between the particles and the wall, provided that the two DNA sequences contained suitably long complementary sequences. In this case, when a particle comes sufficiently close to the

wall, the two strands would spontaneously hybridize together to form a double helix, ultimately forming multiple molecular tethers between the particle and the wall. To permit future experiments with more complex particle-particle and particle-wall interactions, however, we used a slightly more complex scheme of DNA strands, with the sequences and chemical modifications detailed in Table 2.1. Specifically, to enable particle-particle interactions particles were labeled with two complementary DNA sequences, *A Particle* and *B Particle.* The active binding region of the microchannel (the collector) were labeled with *B Glass,* a DNA strand complementary to *A Particle*; non-binding regions of the channel wall were labeled with a non-interacting DNA strands having a *Poly-dT* sequence and a length similar to *B Glass*. To avoid particle-particle interactions mediated by *A Particle* hybridization with *B Particle* in this study, another DNA strand *B Blocker* was added to solution that strongly binds to *B Particle*. In future experiments where particle-particle interactions are desired, these can 'turned on' within the channel by mixing in another strand, *B Stripper,* which is designed to rapidly remove *B Blocker* from the particles via a strand-exchange (or Yurke) process (84).

Table 2.1 DNA Sequence Design

DNA Strand Name	5' Modification	Sequence	3' Modification
A Particle	5'-AmMC6	27T-ATCAAA-CCGCAC	
B Particle	5'-AmMC6	28T-TAGTAT-GTGCGG-TTT	
B Glass	5'-ThioMC6-D	9T-GTGCGG-TTTGAT	3'-Cy5Sp
B Blocker		CCGCAC-ATACTA-ATTCTCCAGCT	
B Stripper		AGCTGGAGAAT-TAGTAT-GTGCGG	

2.3.2 DNA Ligation to Colloidal Microspheres

The method for bonding DNA strands to polystyrene microspheres is adapted from a process we have published previously (76), and relies upon covalently linking amine-modified DNA to a synthetic block polymer, which then is adsorbed onto sterically-stabilized, carboxylate-modified latex (CML) polystyrene microspheres (Seradyn, Ramsey, MN, 13002120100250, diameter 1.02 μm, density 1.05 g/ml, size coefficient of variation 3%). Under the conditions of the experiments reported in this study, the adsorption is effectively irreversible and strong enough to allow particle-particle and particle-wall binding. First, 500 mg of the block polymer, poloxamer F108 (BASF, Ludwigshafen, Germany, 30089186) was dissolved in 2mL dichloromethane (Sigma Aldrich, St. Louis, MO, 270997-100ML) and 30 μL triethylamine (Sigma Aldrich, St. Louis, MO, T0886-100ML). Then, 100mg of fresh 4-Nitrophenyl chloroformate, NPCF (Sigma Aldrich, St. Louis, MO, 160210-56) was added and the mixtures reacted with stirring in an ice bath for 4 hours. The resulting solution was washed once in a 2.6% HCl (Fisher Scientific, Pittsburgh, PA, A144-500), 97.4% 200 proof ethanol solution, allowing the solution to precipitate in a freezer, before centrifuging and removing the supernatant. This process was repeated three more times with a 0.6% HCl, 99.4% 200 proof ethanol solution. The final product was melted with hand heat and then allowed to dry in a vacuum desiccator overnight.

DNA strands with a terminal amino modification were obtained from IDT, Inc. To couple the DNA to the activated F108, 15 μL of 1000 μM amino modified DNA were first added to 1μL carbonate buffer, pH 9.5. Then, 15 μg activated F108 was dissolved in 1 mL 10 mM citric acid buffer (Fisher Scientific, Pittsburgh, PA, A940-500) (Sigma Aldrich, St. Louis, MO, S1804-500g), pH 4. Next, 4 µL F108 solution was added to the DNA solution and allowed to react under aggressive agitation for 4.5 hours. This was done separately for *DNA Particle A* and *DNA Particle B*, and the resulting solutions were combined after reaction. 20 μL of the resulting solution was then added to 40 µL of 10 v% 1.02 μm carboxylate-modified latex beads, along with 340 μL Tris-EDTA buffer solution (Sigma-Aldrich, St. Louis, MO, 93283-500mL) and 4 μL in toluene (Sigma-Aldrich, St. Louis, MO, 244511-100ML) with BODIPY^{TM} 493/503 (ThermoFisher, Waltham, MA, D3922) added. The resulting mixture was gently rotated overnight to periodically invert the sample. The system was then heated at 90 °C for 20 minutes before being washed in Tris-EDTA buffer 3 times. The resulting particles are further sterically stabilized by the DNAylation process, resulting in no noticeable change in hydrodynamic diameter (coalescence) over the course of several months. However, during the toluene driven swelling and subsequent deswelling portions of the particle DNAylation, a small fraction of the particles are observed to aggregate—these aggregates are noted in the subsequent deposition experiments but do not significantly alter the overall particle deposition statistics.

2.3.3 Preparation of microfluidic channels with DNA-ligated walls.

To prepare PDMS microfluidic devices common soft lithography techniques were used. First, 7.5 mL Sylgard® 184 Silicone Elastomer Curing Agent was stirred into 75 g of Sylgard® 184-Silicone Elastomer Base (Dow Corning Corporation, Midland, MI, 3097366-1004). The mixture was placed under vacuum until all air bubbles were removed and then slowly poured onto silicone masters and placed into a 60 °C oven until firm. The devices were cut to their final shape, and a 0.75 mm biopsy punch was used for the inlet and outlet of the device, while a 1.25 mm punch was used for the vacuum seal outlet. Before and after each use they were sonicated for 30 minutes each in acetone and then ethanol, before being allowed to air dry completely. After vacuum bonding with a glass slide, each PDMS channel cross-section was 250 μm wide x 60 μm high, thus creating a uniform wall shear rate in the middle 70% of the channel where all data was collected (the region near each side wall with lower wall shear rates was neglected).

To silanize glass slides, a procedure from Rogers et al. was adapted (85). Briefly, glass slides were gently etched in 28% ammonium hydroxide (Fischer Chemical, Pittsburgh, PA, A669S-212) overnight. Slides were rinsed thoroughly with deionized water (using Barnstead EasyPure Model D7031 water purification system), briefly rinsed in 200 proof ethanol (Decon Labs, King of Prussia, PA, #2716) and then incubated for 30 minutes in a solution of 95% ethanol, 5% deionized water, 16mM acetic acid (Fisher Scientific, Pittsburgh, PA, A38-500), and 1 vol% (3-Mercaptopropyl) trimethoxysilane

(Sigma-Aldrich, St. Louis, MO, 175617-25G). Slides were then rinsed briefly in a 95% ethanol, 5% deionized water, 16mM acetic acid solution and dried at 110 °C for 1 hour.

DNA strands were then ligated onto the silanized glass slides, again following Rogers et al. (85). Briefly, DNA strands with a 5' Thiol Modified C6 S-S modification were used (Integrated DNA Technologies, Coralville, IA). The active strands, *Glass B,* had an additional 3' Cy5™ modification to allow for fluorescence detection. The inactive strands were a length matched Poly-dT sequence with the C6 S-S modification and no fluorophore. First, 2 μL of 1000 μM active strand was added to 8 μL of 500 mM carbonate buffer (Fisher Scientific, Pittsburgh, PA, S263-500). A PDMS device was then positioned on the glass slide with the channel perpendicular to the channel orientation to be used in the final adhesion experiment, loaded with the active DNA strand solution, and allowed to react for two hours leaving a stripe of active strand on the slide. A TNTw solution of 10 mM Tris(hydroxymethyl)-aminomethane (Aldrich, St. Louis, MO, 154563-100G) pH 7.5, 150 mM NaCl, 0.05% Tween 20 (Acros, Pittsburgh, PA, 23336-2500) was used to rinse excess active strand out of the channel, prior to channel removal and air drying of the slide on the benchtop for 30 minutes. This ligation procedure was then repeated for the inactive strand with a second microfluidic channel device using the inactive Poly-dT strand of DNA, oriented perpendicular to the first. The inactive strand significantly reduces the amount of non-specific binding between the DNA colloids and the glass walls.

2.3.4 DNA-Particle Deposition Experimental Procedure and Analysis

The microfluidic device/glass slide was first put on the microscope stage and a vacuum pump was used to ensure the device stayed adherent to the glass. The device was then primed using the TNTw rinse solution and connected to a syringe pump set for withdrawal. Depending on the experimental conditions, between 30 and 300 µL of the DNA functionalized particles were added to 100 µL of 100 µM *B Blocker DNA*, 100 µL of 3M NaCl, 100 µL of 100 mM Phosphate Buffer, pH 7.42 (Fisher Scientific, Pittsburgh, PA, S381-500, S373-500), and Biology Grade Water (GE Healthcare Life Sciences, Logan, Utah, SH30538.03) to a final volume of 1 mL. The particle solution was pipetted on top of the inlet ports into the device and allowed to flow through the device at constant flow rate for the duration of the experiment. Fluorescence microscopy was used to determine the active deposition location containing the *B Glass* strand as well as to image adhered particles. Images were captured every 60s; typical results shown in Figure 2.1. Channel flow rates of 0.1, 1, 3, and 10 μL/min created wall shear rates of 9.3, 93, 280, and 930 s^{-1}, respectively, in the central portion of the channel where data was collected.

Once image sequences were captured, they were rotated such that the device was vertically aligned, and flow pointed upwards. The image prior to the first image with particles was assigned as the initial condition, i.e., $t = 0$. Jitter caused by lack of mechanical repeatability of the scanning stage was removed using an implementation of the Lucas Kanade alignment algorithm obtained from the Image Alignment Toolbox (86).

Once images were properly oriented and dejittered, particle locations were determined using the Kilfoil MATLAB implementation (87) of the Crocker-Grier feature finding algorithm (88) to compute particle counts and locations.

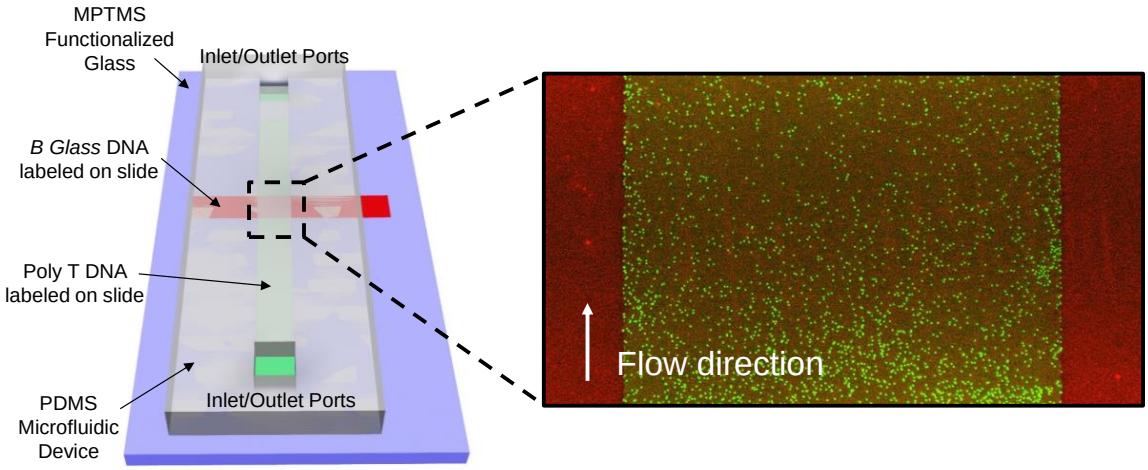

Figure 2.1 Left: Schematic representation of microchannel device. Right: Typical image of 1 μm diameter DNA-grafted particles adhered to active region in a microfluidic channel. The red channel indicates *B Glass* strand functionalization of the glass surface, and the green channel shows DNA-functionalized particles on the surface. Particles were perfused at 10 μL/min at 0.1 v% for 70 minutes. Diffuse green staining is due to out-of-focus particles rapidly flowing in the background.

2.4 Simulation Theory and Methodology

2.4.1 Brownian dynamics simulations

Particle trajectories are described by overdamped Langevin (Brownian) dynamics according to the formalism of Ermack and McCammon (89)

$$\mathbf{r}_i(t+\Delta t) = \mathbf{r}_i(t) + \sum_{j=1}^{N} \mathbf{M}_{ij}(t) \cdot \mathbf{F}_i(t)\Delta t + \mathbf{U}(\mathbf{r}_i)\Delta t\,, \tag{1}$$

where $\mathbf{r}_i(t)$ is the position of particle *i* at time *t*, $\mathbf{M}_{ij}$ is the hydrodynamic mobility tensor that accounts for interparticle hydrodynamic interactions, The force $\mathbf{F}_i(t) = \mathbf{F}_i^I(t) + \mathbf{F}_i^B(t) + \mathbf{F}_G$ is the total non-hydrodynamic force acting on particle *i* that includes contributions from any inter-particle interaction potential (see Section 2.4.2), $\mathbf{F}_i^I(t)$. $\mathbf{F}_i^B(t)$ is a normally distributed stochastic Brownian force with the properties,

$$\left\langle \mathbf{F}_i^B(t) \right\rangle = 0; \qquad \left\langle \mathbf{F}_i^B(t)\mathbf{F}_j^B(t) \right\rangle = \frac{2k_BT\zeta}{\Delta t}\delta_{ij}, \tag{2}$$

where $\zeta = 6\pi\eta R$ is the Stokes drag coefficient on a particle of radius *R* in a fluid with shear viscosity η. In water at room temperature, the isolated particle diffusivity, $D_0 = k_BT/\zeta$, is ~ 4.37 x 10^{-13} m^2/s. Finally, $\mathbf{F}_G$ is the gravitational force acting on each particle—for the experimental system used here, the sedimentation velocity due to gravity is about 25 nm/s. Although sedimentation slightly increases the particle concentration at the wall, we find empirically that it has a quantitatively small impact on our results, and it is not discussed further in the ensuing analysis. Moreover, the low bulk fluid particle volume fractions considered in this study (ϕ < 0.3%) suggest that it is reasonable to neglect inter-particle hydrodynamic interactions between pairs of moving particles and therefore that the hydrodynamic mobility tensor used here is given by $\mathbf{M}_{ij} = (1/\zeta)\mathbf{I}$. By contrast, as we show later in the paper, hydrodynamic interactions between pairs of particles in which one is adhered to the collector are much more important and cannot be neglected. Finally, $\mathbf{U}(\mathbf{r}_i)$ is the velocity of the fluid at the location of particle *i*. The particle velocity due to fluid flow was computed off-line and

fed to the BD simulations as data—different approaches for computing the velocity field are described in Section 2.4.3 .

Equation 1 was integrated numerically using a fixed time step, Δt = 1.14 x 10^{-4} s for particles within the simulation domain shown in Figure 2.2. The total simulation time was 40 minutes for each run with fluid flow rates ranging from Q = 0.1 - 10 μL/min, similar to the experimental conditions described in Section 2.3 . The corresponding particle Reynolds numbers, $\mathrm{Re}_P = 4\dot{\gamma}R^2\rho/\eta$, based on the average fluid velocity and a particle radius of 0.5 μm are approximately 2.4 × 10^{-6} – 2.4 × 10^{-4}, which are safely in the Stokes regime, justifying the use of overdamped Langevin dynamics.

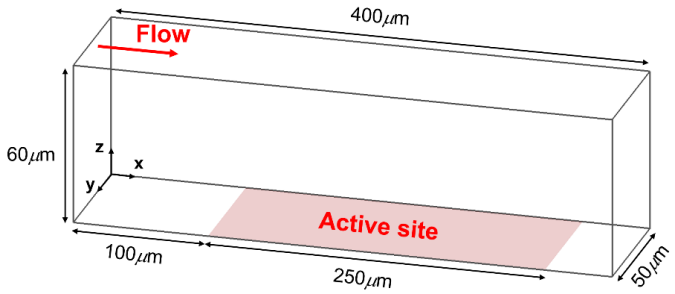

Figure 2.2 Simulation domain for Brownian dynamics with dimensions 400μm × 50μm × 60μm (*x*, *y*, *z*) containing a 250 μm-long adhesive patch (collector). Periodic boundary conditions are applied in the y-direction, impermeable walls are applied in the *z*-direction.

Particles were introduced into the simulation domain at x = 0 μm and removed once they reached a lateral position x = 400 μm. Individual particles were introduced at random channel heights biased by the local fluid velocity in order to create a spatially uniform concentration profile across the channel height—the bias was enforced using the rejection method (90). The overall particle introduction rate was varied to produce

mean volume fractions in the range ϕ = 0.03 – 0.3%. Note that the actual experimental channel length is much longer (~30 mm) than the simulation domain shown in Figure 2.2—this channel length is computationally intractable for BD simulations. We investigated the impact of the additional particle dispersion introduced by the longer channel by solving numerically a convection-diffusion continuum model of the particle distribution across the entire channel length and then using the exit profiles to specify the particle inlet distribution for the BD simulation domain. The primary impact of the additional 30 mm of channel was found to be a flow-rate dependent delay in the onset of particle capture at the collector patch. For example, at Q = 0.1 μL/min, the particle concentration near the channel walls begins to rise only after about 150 s following particle injection and does not reach the bulk value until about 500 s. However, the impact of this particle dispersion was found to be small because the transient timescale is short relative to the overall deposition process (40 mins), particularly at the higher flow rates. Moreover, particles more than a few μm away from the wall are generally too far to contribute to the deposition process, further limiting the impact of any non-uniformity in particle density due to dispersion.

2.4.2 Non-hydrodynamic particle-particle and particle-wall interactions

Interactions between pairs of micron-sized DNA-functionalized particles or between a particle and a DNA-functionalized wall have been studied experimentally in detail and are well described by simple coarse-grained models (35, 85, 91-95). Briefly, these

models account for entropic repulsion between two oligomer brushes brought into close proximity and an effective energetic attraction that arises from hybridization of single-stranded DNA chains. The extent of hybridization, and therefore the strength of the attraction, depends on the specifics of the DNA oligomer sequence, the grafting density of DNA oligomers on each body, the temperature, and the separation distance between the two functionalized entities.

Several features of the experimental system considered here greatly simplify the description of the inter-particle and particle-wall interactions. First, as noted in Section 2.3 , only a short-range repulsive interaction between particles is operational because we do not consider particle-particle adhesion in this study. Second, particle capture by the collector is assumed to take place upon the formation of a single DNA-DNA tether between a moving particle and the collector surface. In other words, we assume that a single tether is sufficiently strong to hold the particle in place long enough to allow the formation of additional tethers, leading to irreversible binding (14, 15). Consequently, the probability of particle capture over a single BD simulation timestep, P_{stick}, is directly related to the kinetics of a single DNA hybridization event according to the relationship $r_{hyb} \times \Delta t = P_{stick}$. The hybridization rate (or equivalently P_{stick}) represents the single regression parameter in our model. The probability of forming a tether between a particle and the wall increases exponentially with decreasing separation with particle binding typically occurring at 10-15 nm of separation (35). Here, we assume that

particle-wall binding may be attempted at separation distances equal to or less than 10 nm.

Other potential sources of inter-particle and particle-wall interactions may exist in general, namely Van der Waals (VdW) and electric double-layer interactions. The Debye screening length for the salt concentration used in our experiments is on the order of 0.5 nm, effectively rendering all electrostatic interactions negligible within about 3-4 nm. The VdW interactions may be estimated with Lifchitz theory to be ~k_BT at 10 nm from the surface and effectively zero above 20 nm (96, 97)—this interaction was also neglected. The implications of the choice of capture distance and surface interaction assumptions are discussed later in Section 2.6 .

2.4.3 Fluid flow fields for particle advection in BD simulations

We consider three models for describing the fluid flow in the channel in order to systematically assess the level of hydrodynamic detail required to capture quantitatively the experimental data. In the first flow model (referred to as the Base Case, or BC), we consider a simple, parallel-plate parabolic flow that assumes all particles are point tracers that do not perturb the flow field and do not interact hydrodynamically with particles adhered to the wall or with the wall itself. This reference flow field is given analytically by

$$\mathbf{U}(z) = \mathbf{e}_x \frac{12Q}{H^3 W} z(H - z), \tag{3}$$

where Q is the flow rate, and H and W are the channel height and width, respectively. Also note that this is a two-dimensional flow that neglects edge effects in the channel width dimension, consistent with the periodic boundary conditions applied in the BD simulations.

The other two models include local corrections of the reference flow in eq. (3) to account for hydrodynamic interactions between moving particles and the channel wall and/or adhered particles. As noted in the Introduction, the salient feature of this approach is to pre-compute estimates for hydrodynamic interactions using a series of one-time, 'off-line' simulations, thereby avoiding the prohibitive computational expense of resolving all hydrodynamic interactions everywhere in the domain at all times. In the second model, we account for particle-wall hydrodynamic interactions by modifying the flow field in eq. (3) to reflect the fact that finite-sized particles close to the wall are subject to hydrodynamic drag and therefore are advected more slowly than predicted by eq. (3); we refer to this model as the Wall Hydrodynamic (WH) model. Finally, in the third model we consider the impact of both particle-particle and particle-wall hydrodynamic interactions on moving particle velocities; this model is referred to as the Wall-and-Particle Hydrodynamic, or WPH, model.

2.4.3.1 Local velocity corrections for particulate flows

For both the WH and WPH models, local hydrodynamic interactions between moving particles and adhered particles or the channel wall were computed numerically

based on the lattice Boltzmann method (LBM) coupled with the smoothed profile method (SPM) (98-100) (see Supporting Material for methodological details). For the WH model, particle trajectories were collected as a function of a single height parameter, $s = (h - R)/R$, where h is the vertical distance between a single particle center-of-mass and the wall. In the case of the WPH model, two independent parameters are required to fully characterize the trajectory database—these are the scaled particle height above the wall, s, and the lateral particle center-of-mass offset relative to the adhered sphere, w.

All LBM-SPM calculations of single-particle trajectories were computed in a domain measuring 20μm (length) by 5μm (width) by 60μm (height) with a grid spacing of 0.1μm in all three dimensions. The smaller domain (relative to the full domain shown in Figure 2.4) was used for computational efficiency and the domain size was investigated to ensure that any finite-size effects were negligible. For the WPH trajectories, the single adhered particle was placed in the middle of the domain on the bottom channel wall, i.e., its center-of-mass coordinates were $x = 10\mu$m, $y = 2.5\mu$m, $z = 0.5\mu$m. For each LBM-SPM run, the moving particle center-of-mass was initially placed at $x = 6\mu$m, while the height (both WH and WPH) and lateral offset (WPH only) positions were varied. For both the WH and WPH trajectories, initial center-of-mass heights in the range 0.6 – 1.6μm ($0.2 \leq s \leq 2.2$) were considered at intervals of 0.2μm, while for the WPH database we also considered initial lateral offsets in the range $-2.8 \leq w \leq 2.8$ at 0.2μm intervals for a total of 90 trajectories; see Figure 2.3. In all cases, LBM-SPM

calculations were executed until the moving particle reached the end of the simulation domain in the flow direction (x = 20μm). Finally, we note that all flow conditions considered in this study correspond to Re_P <<1 and therefore are governed by Stokes flow (see Section 2.4.1). Consequently, particle trajectories computed at a single flow rate may be rescaled and used to represent trajectories at other flow rates. We employed this property to greatly reduce the number of LBM-SPM calculations required to fully span the parametric space in both the WH and WPH models.

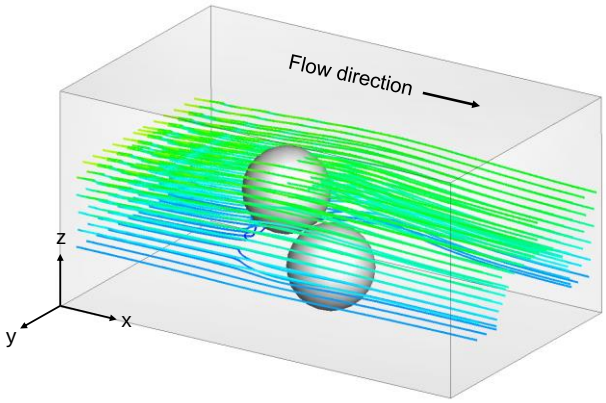

Figure 2.3 Local velocity database for the WPH model showing trajectories of a particle moving around an adhered particle for various entrance heights and lateral offsets (see text). Color represents the *x*-component of the velocity.

The particle-wall hydrodynamic interaction computed for the WH model were summarized in terms of a scalar 'velocity correction factor' that represents the multiplicative deviation from the base case parabolic flow as a function of height from the bottom channel wall; see Supporting Material. For the WH simulations, the velocity correction factor was used to modify the parabolic flow profile, but in all other aspects WH simulations are functionally equivalent to the BC ones.

The WPH simulations require a more complex approach for blending together the background parabolic flow and the local particle trajectories; see Figure 2.4. Within a WPH simulation, each adhered particle is assigned a hemispherical interaction zone with a 4 μm radius—any moving particles that enter an interaction zone are evolved along the trajectories computed using the LBM-SPM. In the event that a moving particle exists in multiple interaction zones (i.e., the interaction zones of two adhered particles overlap), the particle is evolved along trajectories corresponding to the nearest adhered particle. The Eulerian-to-Lagrangian mapping required to transfer the velocities along the LBM-SPM trajectories onto BD particles that are within interaction range of adhered particles is described in the Supporting Material.

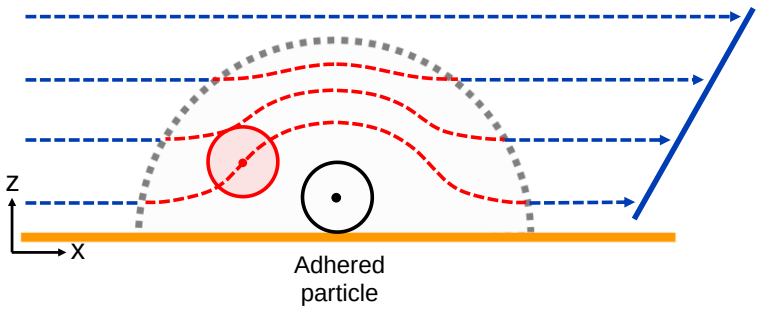

Figure 2.4 Schematic diagram for local velocity coupling in the WPH model. Blue dashed lines represent outer velocity field (eq. (3)), red dashed lines denote LBM-SPM trajectories for a particle (red circle) moving around an adhered particle (black circle) within the interaction shell (denoted by the dotted grey line).

2.5 Results and Discussion

Brownian dynamics simulations were performed using each of the three velocity models (BC, WH, and WPH) described in Section 2.4.3 at 4 flow rates (Q = 0.1, 1.0, 3.0, and 10 μL/min) and 3 particle volume fractions (0.03%, 0.1%, and 0.3%). For each run,

the evolution of the particle coverage as function of time and the final adhered particle positions were recorded. At each parameter combination, runs were repeated with adjustment of the particle adhesion rate until the best possible fit of the experimental particle coverage evolution was achieved. The one-dimensional optimization was performed manually using a simple bisection strategy in which the minimum was first bracketed by trial-and-error. The particle positions on the collector patch also were used to compute a two-dimensional autocorrelation function that was also compared to the experimental result at various time points.

2.5.1 Deposition Rate Analysis

The coverage evolution at each of the 4 flow rates and 3 particle volume fractions are shown in Figs. 5-7 for each of the three velocity models, BC, WP, and WPH. For all cases, coverages were computed over the entire collector domain in both the flow and transverse directions. As seen in Figure 2.1, enhanced deposition is visible near the collector entrance, a feature that is also noted in simulation. Given that this heterogeneity was only significantly apparent at the highest flow rate (10 μm/min), and that additional statistics (larger domains) would be required to quantify it, we did not attempt to isolate it from the computed coverage average. In addition, any edge effects in the transverse direction were not considered in the simulations (see Section 2.4.1). Errors arising from the exclusion of edge effects were assessed by comparing average coverages over the entire width of the collector with those computed when excluding

5%, 10%, and 20% of the domain near the channel edges. We find that the coverages vary by no more than 5-10% across this range—given the added complexity of resolving the edges in simulation, we chose to neglect this error in the subsequent analysis.

For each flow rate/particle fraction combination, the best fit of the coverage evolution (using the particle adhesion rate as a single adjustable parameter) to the experimental data is shown for the 3 particle densities at a given flow rate, while each of the 4 panels represents a different flow rate. The BC model (Figure 2.5) is able to capture the overall trends—coverage increases with increasing particle density and decreases as the flow rate is increased. However, the agreement is not quantitative, and the shapes of the coverage evolution curves are rather poorly captured in some of the cases. Including the particle-wall hydrodynamic interactions in the WH model (Figure 2.6) does not lead to significant improvement—in fact, the results are largely the same as the BC case, signifying that particle-wall hydrodynamic interactions are not critical in describing how the deposition process evolves. By contrast, the situation is dramatically altered when particle-particle hydrodynamic interactions also are included in the WPH model (Figure 2.7). Here, the single regression parameters are sufficient to capture the coverage evolution across all the flow and particle density conditions and across all times considered in the experiments. It is apparent from this improvement that the details of the hydrodynamic interactions between moving and adhered particles is critically important.

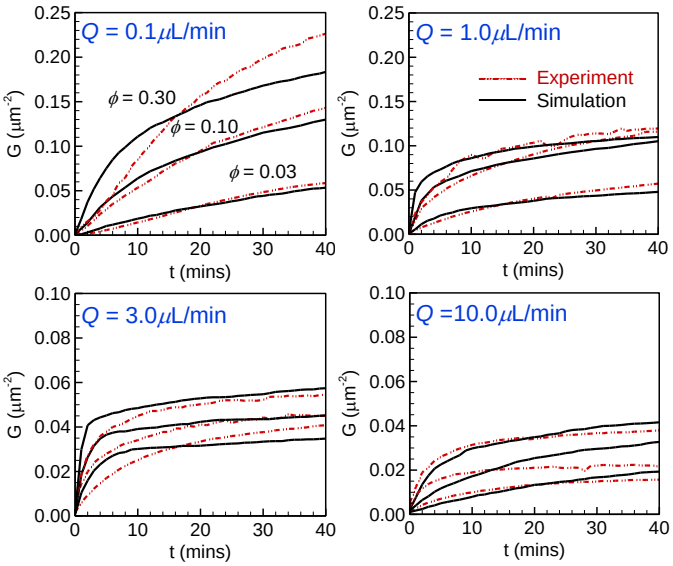

Figure 2.5 Evolution in time of sub-monolayer particle coverage (particles/μm^2) on the collector patch. Each panel shows the experimental and best-fit simulation results (BC model) at a given channel flow rate, *Q*, and at 3 different overall particle volume fractions (in %).

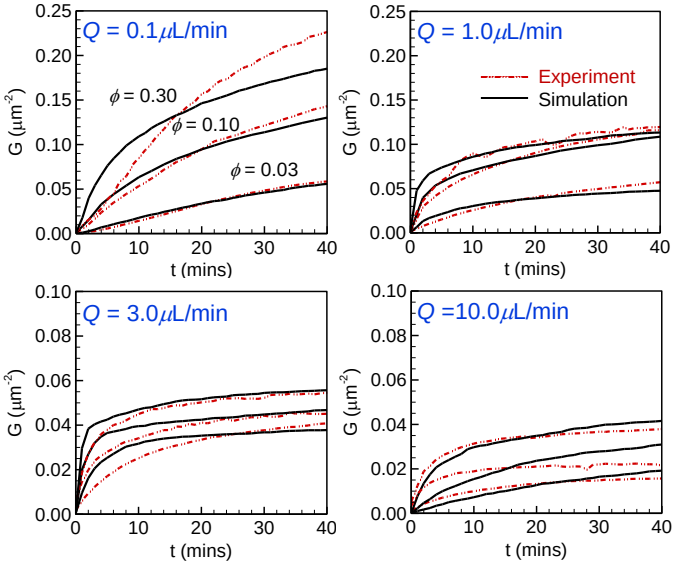

Figure 2.6 Evolution in time of sub-monolayer particle coverage (particles/μm^2) on the collector patch. Each panel shows the experimental and best-fit simulation results (WP model) at a given channel flow rate, *Q*, and at 3 different overall particle volume fractions (in %).

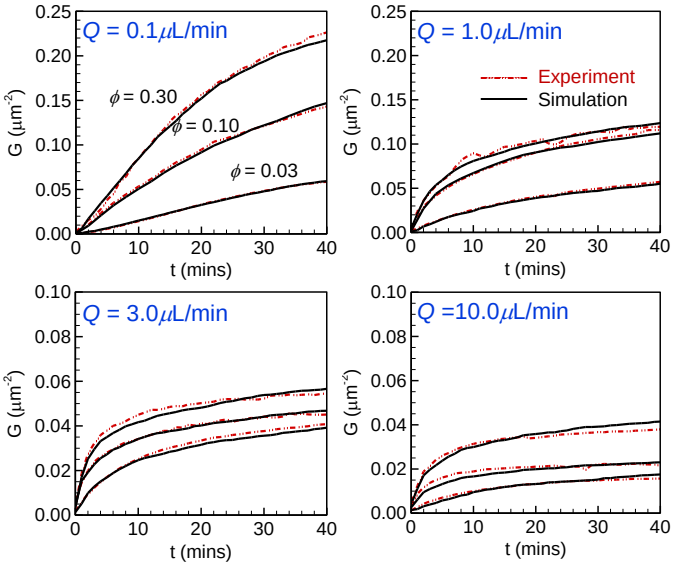

Figure 2.7 Evolution in time of sub-monolayer particle coverage (particles/μm^2) on the collector patch. Each panel shows the experimental and best-fit simulation results (WPH model) at a given channel flow rate, *Q*, and at 3 different overall particle volume fractions (in %).

We studied further the role of the particle-wall hydrodynamic interaction in model fidelity by considering a simplified version of the WPH model. In this model, denoted as WPH/-, a single, steady-state LBM calculation of the flow field around a single adhered particle was used to define the local velocity in the same 4 μm-diameter hemisphere interaction region used in the WPH model. In effect, the WPH/- model assumes (in the off-line calculation of the velocity field) that the nearby moving particle is a tracer (i.e., does not perturb the flow) that is advected in a flow field around the adhered particle. Therefore, although the flow distortion due to the adhered particle is explicitly captured (unlike in the BC and WH cases), the hydrodynamic interaction between the two spheres is not. The WPH/- model is computationally attractive relative to WPH because only a single, steady-state LBM flow field calculation is required, rather

than the ensemble of individual two-particle trajectories needed for the WPH model. As shown in Figure 2.14 (Supporting Materials), the WPH/- model is able to capture the deposition process at the two lower flow rates but, interestingly, fails strongly at the higher flow rates.

One way to explain the failure of the WPH/- model to capture the physics of deposition under flow is to consider example trajectories of particles moving around an adhered particle within the different models. Shown in Figure 2.8 are the (noiseless) trajectories of a particle moving directly over an adhered one as predicted by the BC, WPH/-, and WPH models. As expected, the BC model shows that the moving particle rises over the adhered one due to repulsive interactions (collision) and then maintains a horizontal trajectory after reaching the maximum height. This is not the case in both the WPH/- and WPH models, which show that a moving particle will be advected back towards the wall after passing the top of the adhered particle. What is different between the two cases, however, is the extent of the return—while the WPH/- trajectories are always symmetric and result in no net lift, the WPH ones may be asymmetric, depending on the initial height of the moving particle. The dramatic contrast in the ability of the two models to capture the experimental data highlights the importance of the lift extent—although the differences are on the sub-micron scale, they lead to large impacts on the diffusion time required for a particle to reach the surface and potentially become adhered.

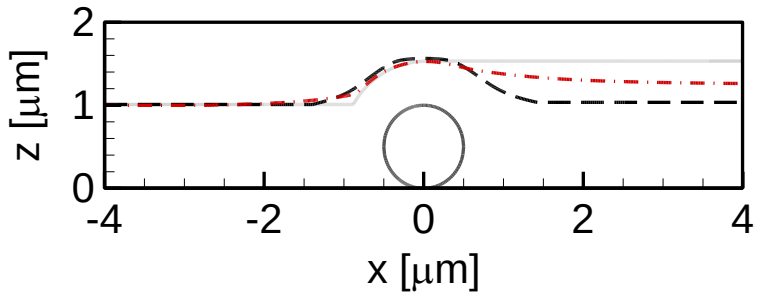

Figure 2.8 Two-dimensional projection of particle trajectories around a single adhered particle (with zero lateral offset) in different velocity models. Grey line—BC/WH, black dashed line—WPH/-, red dash-dot line—WPH.

To provide a quantitative comparison between the various model results, the model error relative to the experimental data for each optimized velocity model was computed using the L2 norm evaluated at 80 points (0 to 40 mins) along the coverage evolution curves, i.e.,

$$L2\ error = \sqrt{\frac{1}{80}\sum_{i=1}^{80}\left(\frac{G_i^{sim} - G_i^{\exp}}{G_i^{\exp}}\right)^2} \tag{4}$$

where G_i^{sim} and $G_i^{\exp}$ are the simulated and experimental particle coverages, respectively, at time *i*. The average, maximum and minimum errors for each velocity model are shown in Figure 2.9. As expected, the BC, WP, and WPH/- models exhibit, on average, higher errors than the WPH model (~25% versus 8%). Even more significant is that the maximum error in first three models can be as high as 60%, suggesting a highly non-uniform model accuracy. By contrast, the WPH model exhibits relatively small differences (~8%) between the maximum, minimum, and average errors. This

consistency is yet another indication of the ability of the WPH model to capture coverage evolution over a wide range of conditions.

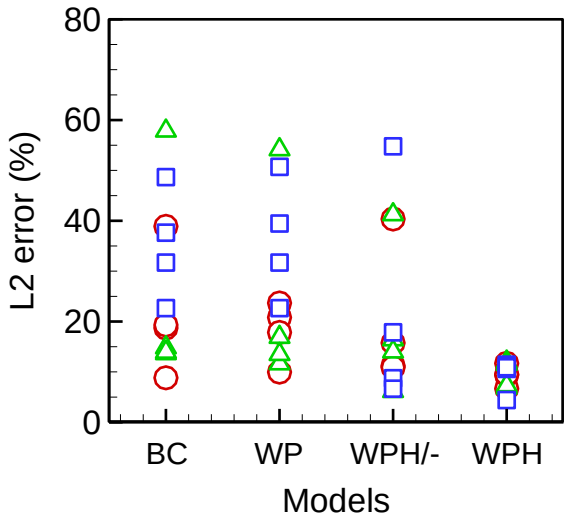

Figure 2.9 . L2-norm of model deviation relative to corresponding experimental data for BC, WP, WPH/-, and WPH models. Each symbol corresponds to a flow rate/particle volume fraction combination: blue squares—ϕ = 0.03%, green deltas—ϕ = 0.1%, and red circles—ϕ = 0.3%.

The corresponding best-fit values of the adhesion rate are shown in Figure 2.10 for all velocity models. Once again, the BC, WH, and WPH/- models show a large dispersion (several orders-of-magnitude!) in the optimal adhesion rates fitted for each combination of flow rate and particle density. This is an additional indication of poor model performance because the adhesion rate, which is determined by DNA hybridization kinetics, is expected to be independent of both the particle volume fraction and the fluid flow rate. By contrast, the WPH model exhibits a much smaller variation in the fitted adhesion rates, as well as a somewhat lower value for the average (~10^2 s^{-1} for WPH versus 10^3 s^{-1} for BC and WP). It is notable that the lowest values of the regressed adhesion rates for all cases correspond to the highest flow rate

experiment (Q = 10 μL/min)—this is likely due to some (observed) particle detachment that is taking place in the experiments at the relatively high shear rates, which slightly lowers the coverage. Nonetheless, this effect is clearly exaggerated in the first 3 models and only leads to a modest effect in the WPH model. It is also worth noting that the regressed WPH adhesion rates correspond to particle sticking probabilities of ~0.01. These small values are consistent with the fact that the experimental coverages evolve significantly more slowly than expected from analytical models (64).

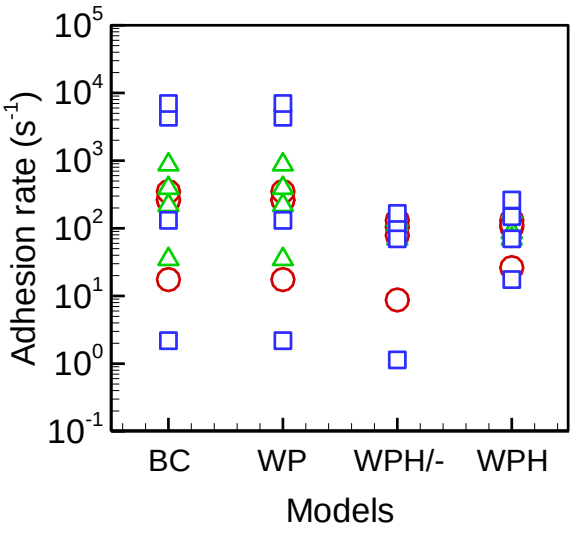

Figure 2.10 . Best-fit adhesion rate for BC, WP, WPH/-, and WPH models. Each symbol corresponds to a flow rate/particle volume fraction combination: blue squares—ϕ = 0.03%, green deltas—ϕ = 0.1%, and red circles—ϕ = 0.3%.

The single regression parameter used in our study—the DNA hybridization rate—may be independently estimated based on knowledge of the DNA areal density on both the particles and the collector surface (35). For the experimental conditions considered in this study, corresponding to particle and wall areal DNA densities of ~1000 and ~11,000 DNA/μm^2, respectively, the average adhesion rate is expected to be ~10^3 s^{-1},

which is roughly a factor of 5-10 higher than the ~10^2 s^{-1} value obtained with the WPH model. This discrepancy may be explained by considering the various assumptions made in the particle-wall interaction model. First, we note that all models neglect the effect of hydrodynamic interactions on particle diffusion. It is well established that particle-wall and bulk particle-particle hydrodynamic interactions reduce particle diffusivities as well as velocities at small separations. Consequently, diffusion near adhered particles is over-estimated in our analysis, leading to an overestimate of particles reaching the binding threshold distance and resulting in a reduction of the regressed adhesion rate. While analytical and computationally-derived corrections to particle diffusion have been developed for particle-wall and bulk particle-particle interactions (21, 64, 101), these are not generally applicable to the more complex case where a particle moves around another that is adhered to a wall. One possible approach to address this limitation in the future is to use a method such as Multi-Particle Collision Dynamics (MPCD) (102, 103) or fluctuating lattice Boltzmann (FLB) (104), which naturally includes Brownian motion, to compute the trajectories in a WPH simulation.

The lack of diffusion correction near the wall must be considered in the context of the other assumptions, namely that VdW attractions are neglected, particle adhesion is limited to a 10 nm capture distance, and that the particle adhesion rate is independent of the particle-wall separation distance (in reality, the capture rate depends on the degree of overlap of the DNA brushes). Each of these assumptions is likely to have some effect on the regressed value of the effective adhesion rate. In

effect, our approach combines these approximations into a single regression parameter. Nonetheless, the fact that the other models cannot adequately capture the data for any value of this parameter, while the WPH model can, suggests that the key requirement is capturing convective flows in the immediate vicinity of adhered particles, rather than the precise details of the inter-particle interactions at nanometer-scale separations.

2.5.2 Film Microstructure Analysis

Next, we consider the microstructure of the sub-monolayer adhered particle film for each of the models relative to the experimental data using a two-dimensional structural auto-correlation function (105). The autocorrelation function measures the particle density as a function of position around each particle and therefore describes the structure of the adhered particle film. The autocorrelation function was computed by discretizing the observed collector domain into $L \times W$ binarized pixels each of dimension 0.3225×0.3225 μm^2 that were assigned a value of 1 if a particle center-of-mass was present and 0 otherwise. For both the experimental data and simulation predictions, the full collector domains (250×300 μm^2 and 250×50 μm^2, respectively) were used to compute the autocorrelation function.

Autocorrelation functions at several time points are shown in Figure 2.11 at a flow rate of 1.0 μL/min and a particle fraction of 0.1%. The experiments show an essentially uniform distribution of particles except for one striking feature—a vertical line, corresponding to lower particle density, aligned with the flow direction (bottom to

top). This feature, which is apparent both upstream and downstream of the reference particles, represents the lifting of moving particles by adhered particles due to both volume exclusion and hydrodynamic effects. To leading order, all 3 models capture the particle depletion effect. However, closer inspection shows that the width of the depletion zone (approximately a full particle diameter) is overestimated in both the WH and WPH/- models, indicating that these models fail to capture correctly the lateral hydrodynamic interactions between moving and adhered particles. By contrast, the thin depletion zone predicted by the WPH model demonstrates the ability of the model to correctly predict particle trajectories in the vicinity of adhered particles. Moreover, some additional discrepancies are noted in the WH and WPH/- autocorrelation functions, most notably a small ring of enhanced particle density immediately adjacent to the reference particle. Finally, no significant time evolution of the microstructure is observed at this flow rate.

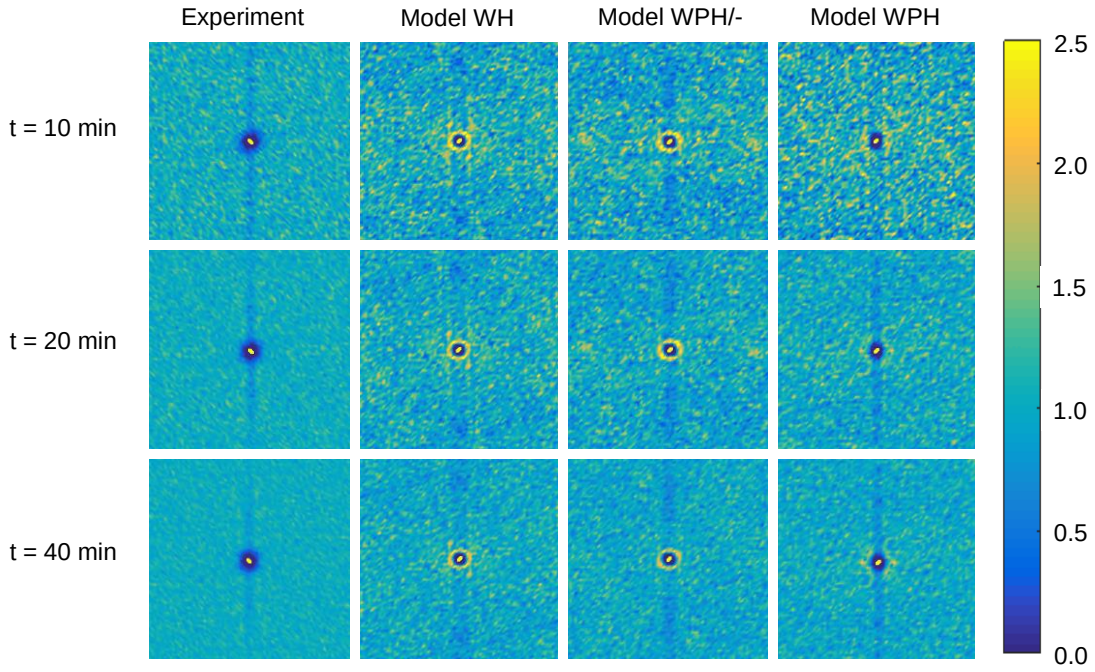

Figure 2.11 . Two-dimensional autocorrelation function as a function of time (rows) for the experimental data and three velocity models (columns) at Q = 1.0 μL/min. Color scale shows normalized density—a value of unity corresponds to the domain-averaged particle density.

Lowering the flow rate to 0.3 μL/min increases the time scale of the overall deposition process as shown in Figure 2.15 (see Supporting Materials). Specifically, the experimental data shows that the depletion line becomes less prominent and shorter as the deposition process continues between 10 and 40 mins. Generally, lower flow rates reduce the particle exclusion zone because more time is available for diffusion to bring particles to the surface, i.e., diffusion acts to 'erase' the advectively-generated depletion zone. This picture is captured remarkably well by the WPH model but quite poorly by the WH and WPH/- models—the latter show an excessively prominent depletion zone at all times and fail to capture the temporal evolution of the microstructure.

2.6 Conclusions

We have studied the deposition of micron-scale spherical particles on an adhesive collector patch in a microfluidic channel flow using a synergistic combination of experiments and computations. By modifying a microfluidic device used previously to study thrombosis in blood flow (59, 71, 72) to accommodate DNA-functionalized polystyrene microspheres, we have developed a versatile microfluidic flow assay for particle deposition studies that exhibits a high degree of controllability and well-defined interactions (76, 85). Specifically, our system was engineered to reduce the complexity associated with non-hydrodynamic interactions between particles and between particles and the channel walls—electrostatic interactions were salted-out and particle stickiness, mediated entirely by DNA hybridization, was short-ranged. Moreover, the particle DNA-functionalization technology used here may be readily modified to accommodate particle-particle adhesion and the formation of more complex, multilayered structures, such as those found in biofilms [4] or blood clots [20].

The microfluidic system was used to generate quantitative measurements of sub-monolayer particle deposition rates and microstructure under conditions of varying flow rates and particle volume fractions. The experimental data was analyzed with a computationally efficient Lagrangian simulation framework that includes hydrodynamic interactions computed numerically in an off-line fashion, in contrast to previous approaches that rely on analytical solutions (61, 64, 83). One of our primary goals was to

systematically identify what types of hydrodynamic interactions are crucial for accurate modeling of the deposition process. We find that even apparently 'simple' metrics, such as the overall particle coverage as a function of time, cannot be captured well by simulations that do not accurately represent the trajectories of moving particles in the vicinity of already adhered particles at the wall. Unfortunately, these types of hydrodynamic interactions are difficult to accurately describe with analytical calculations and generally require explicit fluid-structure simulations (81) to resolve. Our results further suggest that other types of hydrodynamic interactions, such as those among pairs of moving particles and those between moving particles and the bare channel walls, are significantly less critical for an accurate description of the deposition process, at least under the conditions studied here. Finally, the microstructural distribution of deposited particles also was studied quantitatively. Interestingly, we find that once the overall coverage evolution was captured correctly, more subtle microstructural details, such as a time-varying zone of reduced particle density in the flow direction around adhered particles, also were described well.

Taken together, our findings provide guidance for construction of models for particle flow and deposition that are both accurate and computationally efficient. Nonetheless, additional methodological developments will be required to extend the approach presented here to denser and/or multi-layer deposited films (64). In particular, it is not immediately obvious how to superpose the disturbances created by the individual adhered particles to allow for a comprehensive, yet still tractable,

trajectory database. These modifications and extensions will be the subject of future investigations.

2.7 Supporting Materials

2.7.1 Preparation of microfluidic channels with DNA-ligated walls

The areal density of the *B Glass* strand onto the glass slides was determined by quantitative fluorescence, compared to a fluorescence standard consisting of a microchannel filled with soluble *Glass B* DNA at a known concentration. Experiments varying the concentration of *Glass B* strand during incubation show that the 200 µM concentration used saturated the surface, and yields about 11,000 DNA/µm^2, data in Figure 2.12.

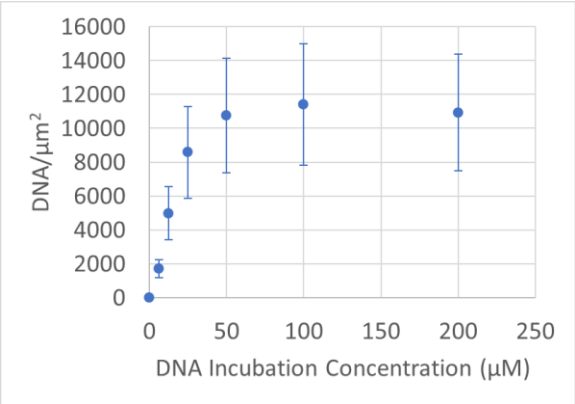

Figure 2.12 The results of quantitative fluorescence experiments show that the DNA ligation on silanized glass saturates at ~11,000 DNA/µm^2 under the reaction conditions used here.

2.7.2 The lattice Boltzmann-smoothed profile method (LBM-SPM) for WH and WPH Databases

The smoothed profile method was introduced in ref. (98, 99) as an alternative to immersed boundary approaches (106, 107). In this approach, the momentum conservation equations for the fluid are augmented to include a force arising from the presence of immersed particles. For the incompressible Navier-Stokes case, the modified momentum balance and continuity equations take the form

$$\frac{\partial \mathbf{u}}{\partial t} + \mathbf{u} \cdot \nabla \mathbf{u} = -\frac{1}{\rho} \nabla P + \nu \nabla^2 \mathbf{u} + \psi \mathbf{f}^P, \tag{5}$$

$$\nabla \cdot \mathbf{u} = 0, \tag{6}$$

where **u** is the fluid velocity, ρ is the fluid density, *P* is the pressure, and ν is the fluid kinematic viscosity. The last term in eq. (1) represents the force exerted by a particle on the fluid as a function of position, where ψ is a phase-field function defined such that ψ = 1 at locations inside particles, ψ = 0 in the fluid, and 0< ψ <1 across an interfacial region between the two. The phase-field function is given by

$$\psi(\mathbf{x}) = \frac{1}{2}\left[1 + \tanh \frac{R - |\mathbf{x} - \mathbf{X}|}{\xi}\right], \tag{7}$$

where *R* denotes the radius of a particle, **X** is the position of the particle center-of-mass, and **x** is the position of the computational nodes (in the present case corresponding to the lattice Boltzmann grid). The parameter ξ represents the particle-

fluid interface thickness and sets the accuracy of the method; here, as is commonly applied, $\xi = 1$ (99, 100).

The solid-on-fluid force at a node located at position **x** is given by

$$\mathbf{f}^P(\mathbf{x},t) = \psi(\mathbf{x},t)\frac{\left[\mathbf{u}^P(\mathbf{x},t) - \mathbf{u}(\mathbf{x},t)\right]}{\Delta t}, \tag{8}$$

where **u** is the fluid velocity and $\mathbf{u}^p$ is the velocity of the particle, both computed at the node. The solid velocity at node position **x** is given by the sum of particle translational ($\mathbf{V}_i$) and angular components ($\mathbf{\Omega}_i$),

$$\mathbf{u}^P(\mathbf{x},t) = \mathbf{V}_i(t) + \mathbf{\Omega}_i(t)\times(\mathbf{x}-\mathbf{X}). \tag{9}$$

Consequently, the total hydrodynamic force and torque exerted by the fluid on particle *i* are given by

$$\mathbf{F}_i^H = -\sum_{\mathbf{x}\in V_i} \rho(\mathbf{x})\mathbf{f}^P(\mathbf{x},t), \tag{10}$$

$$\mathbf{T}_i^H = -\sum_{\mathbf{x}\in V_i} (\mathbf{x}-\mathbf{X})\times\rho(\mathbf{x})\mathbf{f}^P(\mathbf{x},t), \tag{11}$$

where the summations run over all nodes located in the domain of particle *i*. The linear and angular velocities, and the center-of-mass position of each particle are integrated in time using Euler integration,

$$\mathbf{V}_i(t+\Delta t) = \mathbf{V}_i(t) + \frac{\mathbf{F}_i^H + \mathbf{F}_i^I + \mathbf{F}_i^{LUB}}{M_i}\Delta t, \tag{12}$$

$$\mathbf{\Omega}_i(t+\Delta t) = \mathbf{\Omega}_i(t) + \frac{\mathbf{T}_i^H}{I_i}\Delta t\,, \tag{13}$$

$$\mathbf{X}(t+\Delta t) = \mathbf{X}(t) + \mathbf{V}(t+\Delta t)\Delta t\,, \tag{14}$$

where M_i and I_i are the mass and moment of inertia of particle i. Finally, the term $\mathbf{F}_i^{LUB}$ is introduced to account for lubrication forces between pairs of particles that are very close to each other (108). The lubrication force is given by

$$\mathbf{F}^{LUB} = \begin{cases} -6\pi\eta \dfrac{R_1^2 R_2^2}{(R_1+R_2)^2}\left(\dfrac{1}{h}-\dfrac{1}{h_c}\right)\mathbf{V}_{12}\cdot\hat{\mathbf{X}}_{12}, & h < h_c \\ 0, & h > h_c \end{cases} \tag{15}$$

where R_1 and R_2 are the particle radii, h is the minimum surface-to-surface separation between the particles, h_c is a cut-off distance (here set to 0.1μm, or 1 grid spacing), $\mathbf{V}_{12}$ is the relative particle velocity, and $\hat{\mathbf{X}}_{12} = (\mathbf{X}_1 - \mathbf{X}_2)/|\mathbf{X}_1 - \mathbf{X}_2|$ is the unit vector connecting the particle centers-of-mass.

The momentum and continuity equations, eqs. (1) and (2), were solved using LBM in three dimensions and the particle trajectories updated using the SPM; the combination is referred to as LBM-SPM. For the LBM, the Bhatnagar–Gross–Krook (BGK) collision model (109) was used with the D3Q19 velocity set. In this framework, each LBM lattice node streams the distribution function to its 18 nearest-neighbors as well as itself. After the streaming step, the distribution function at each lattice site is relaxed to an equilibrium configuration. The macroscopic density and velocity of the fluid are obtained respectively from the zeroth and first velocity moments of the distribution

function at each node. No-slip boundary conditions were applied on the top and bottom channel walls and on the adhered particle (for the WPH model), while periodic boundary conditions were applied in the width dimension. A fully developed, two-dimensional parabolic flow profile with the desired flow rate was applied at the domain inlet, while constant pressure was applied at the outlet using the Zou-He boundary condition (110). Additional standard methodological details related to LBM may be found in refs. (111, 112).

2.7.3 Particle-Wall Hydrodynamic Interactions for the WH Model

The particle-wall hydrodynamic interaction computed for the WH model is shown in Figure 2.13 in terms of a scalar 'velocity correction factor' that represents the multiplicative deviation from the base case parabolic flow as a function of height from the bottom channel wall. As shown in the Figure, the numerical results are in close agreement with analytical predictions (21, 64, 113).

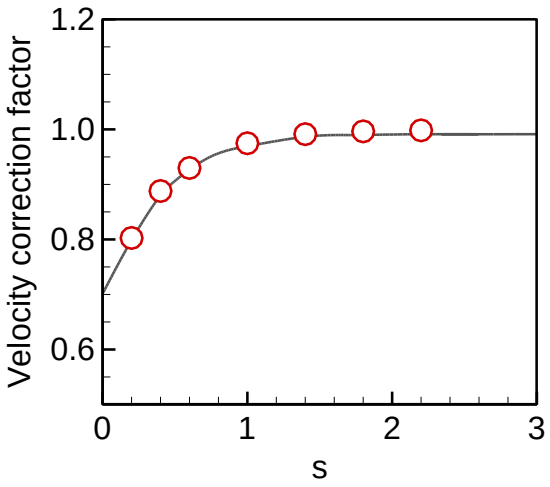

Figure 2.13 A universal correction factor for a single particle motion near a planar solid wall. It describes corrected translational velocity of a particle due to particle-wall hydrodynamic interactions in channel flow. Red circle and black solid line denote a numerical result obtained by LBM-SPM calculation and analytical prediction, respectively.

2.7.4 Mapping Off-Line Trajectories onto BD Particles in WPH Model

The Eulerian-to-Lagrangian mapping required to transfer the velocities along the LBM-SPM trajectories onto moving BD particles that are within interaction range of adhered particles was accomplished by first mapping the velocity data from the collection of trajectories onto a fixed grid, i.e., the one used in the LBM-SPM calculations. Then, the velocities were mapped from LBM nodes to the center-of-mass of moving BD particles using the interpolation scheme

$$\mathbf{u}_{BD}(\mathbf{r}) = \sum \mathbf{u}_{LBM-SPM}(\mathbf{x})\delta\left(\mathbf{e}_x \cdot (\mathbf{x}-\mathbf{r})\right)\delta\left(\mathbf{e}_y \cdot (\mathbf{x}-\mathbf{r})\right)\delta\left(\mathbf{e}_z \cdot (\mathbf{x}-\mathbf{r})\right), \qquad (16)$$

where $\mathbf{u}_{BD}(\mathbf{r})$ is the velocity of the BD particle, and $\mathbf{u}_{LBM-SPM}(\mathbf{x})$ is the velocity vector at the LBM node; the sum runs over all eight nodes that surround the particle position at a given time. The 3-point Peskin interpolation function is used here (106):

$$\delta(r)=\begin{cases}\frac{1}{3}\left(1+\sqrt{1-3r^2}\right) & 0\le|r|\le\frac{1}{2}\\ \frac{1}{6}\left(5-3|r|-\sqrt{-2+6|r|-3r^2}\right) & \frac{1}{2}\le|r|\le\frac{3}{2}\\ 0 & \frac{3}{2}\le|r|\end{cases}. \tag{17}$$

2.7.5 Coverage Evolution Prediction with the WPH/- Model

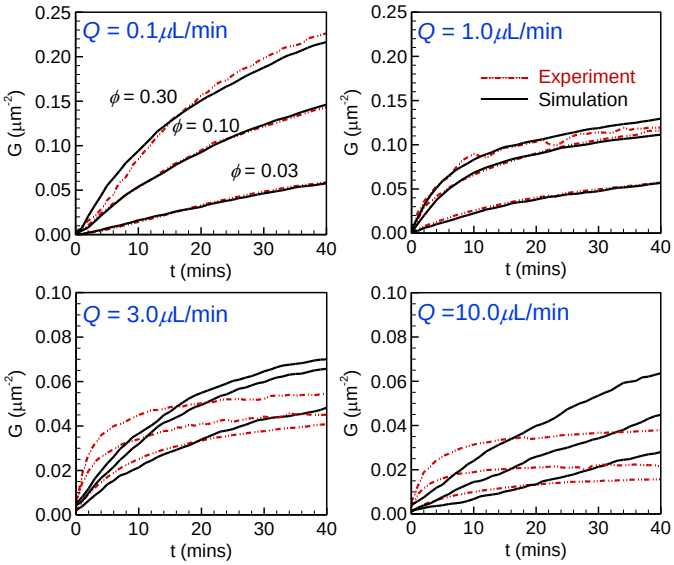

Figure 2.14 Evolution in time of sub-monolayer particle coverage (particles/μm^2) on the collector patch. Each panel shows the experimental and best-fit simulation results (WPH/- model) at a given channel flow rate, *Q*, and at 3 different overall particle volume fractions (in %).

2.7.6 Autocorrelation Data for Q = 0.3 μL/min

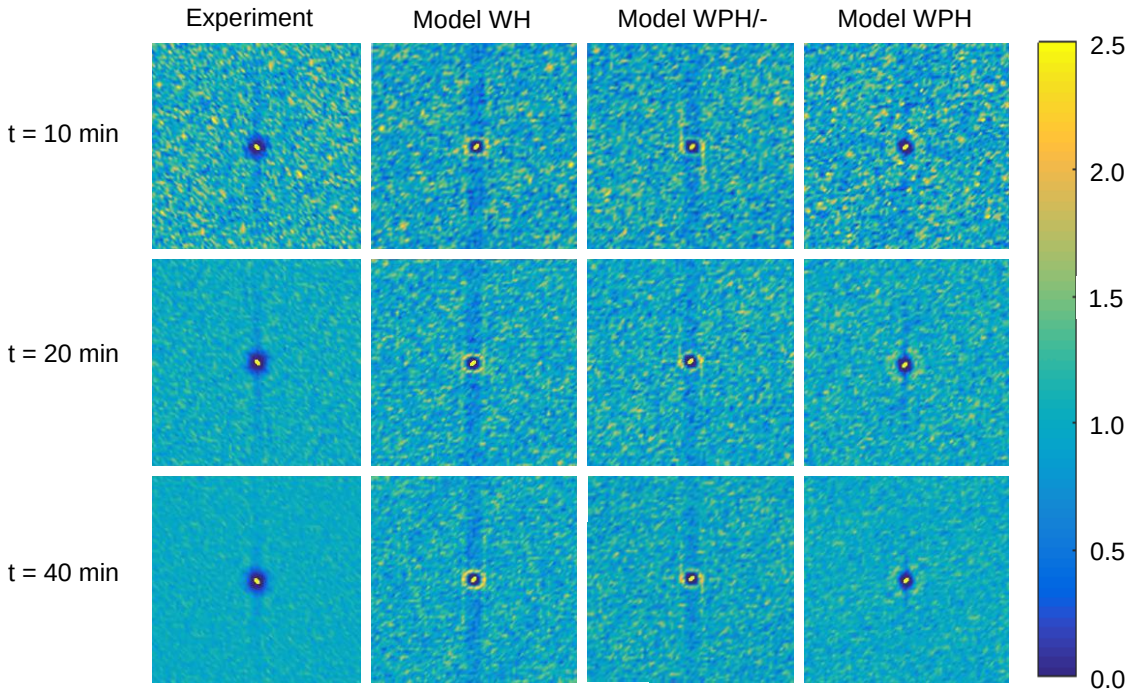

Figure 2.15 Two-dimensional autocorrelation function as a function of time (rows) for the experimental data and three velocity models (columns) at Q = 0.3 μL/min. Color scale shows normalized density—a value of unity corresponds to the domain-averaged particle density.

Chapter 3 Multilayer Particle Deposition

3.1 Introduction

The DNA system used in Chapter 2 was designed to allow for particle-to-particle interactions. The overall experimental design is shown in Figure 3.1 and a summary of the DNA design's thermodynamics and degree of overlap are shown in Table 3.1 and

Table 3.2, respectively. Particles were labeled with complementary *A* and *B* DNA strands. A blocker strand was added which bound strongly to the B DNA on the particle to prevent premature aggregation and self-passivation. These particles were then perfused through the channel where they adhered to the region of the glass labeled with *B Glass,* a DNA strand complementary to *A*. Additionally, during the experiment, *B Stripper* was perfused through the outer edges of the channel, where it could diffuse throughout the width of the channel and remove the blocker strand from adhered particles. This removal of the blocker strand would activate particle-to-particle interactions and allow for the particles in stream to bind to the newly unblocked B strands on the adhered particles.

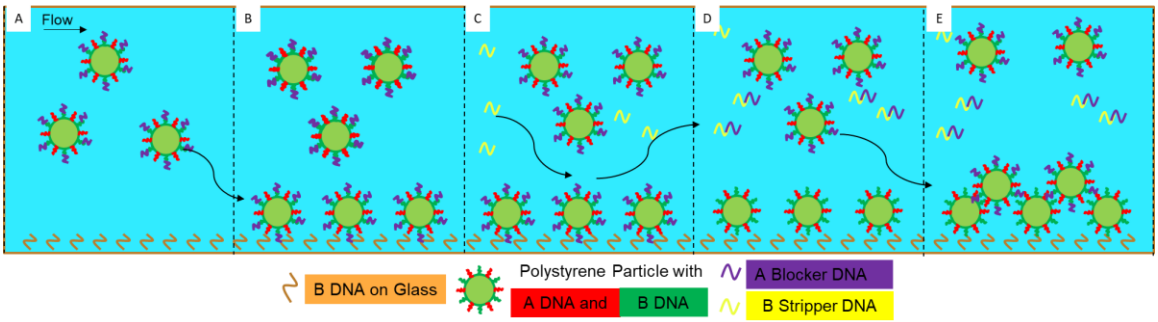

Figure 3.1 Schematic of particle clotting DNA design. Particles coated with A and B DNA are perfused over a channel containing B DNA glass. To prevent particle aggregation in solution, a blocker strand would be added, preventing the A-B DNA complex. Particles could then bind to the surface through the A-B Glass DNA complex. Then, B Stripper DNA would remove the blocker strand from the surface bound particles, thus "activating" the particle-to-particle interaction, allowing for subsequent layers of particles to deposit.

Table 3.1 DNA Thermodynamic Analysis for Clotting Particle System, Values from Nupack (114)

ΔG (25°C,200mM NaCl) [kCal/mole]	*B Glass*	*B Particle*	*Stripper*
A Particle	-15.1	-10.7	-7.9
B Blocker	-8.3	-14.2	-28.5

Table 3.2 Summary of Clotting Particle System DNA Overlap

Overlap	*B Glass*	*B Particle*	*Stripper*
A Particle	12	9	6
B Blocker	6	12	23

However, in the clotting experiments, it was observed that while the first layer of particles deposited on the surface as in Chapter 2 , subsequent layers did not form. Additionally, when flow was stopped, it did appear that aggregates would form, however, restarting the flow sheared the particle aggregates from the surface. In this chapter, we analyze this clotting system further and propose a remediation for future experiments. We analyze the diffusion of the stripper DNA into the width of the channel to confirm that the adhered particles can be "activated" for particle-to-particle

interactions. Then, we perform a back-of-the-envelope calculation to determine the number of DNA bridges between particles necessary to prevent a particle from being sheared off of the particle "clot", finding that for bio-relevant shear rates the particle-to-particle DNA bridges are strong enough to allow for aggregation in a shear flow. We then consider the kinetics of the particle-to-particle interaction, finding that for the implemented system, self-passivation significantly impedes "clot" build up. To overcome this self-passivation, we present a simple change of the particle preparation which may allow for future DNA particle "clotting" experiments.

3.2 Diffusion of Stripper DNA into Full Channel

One of the key questions of the system is whether the stripper DNA strand, which is perfused through the outer edges of the channel of the device, can diffuse far enough to strip the blocker strand from the particles towards the center of the channel. Of course, the characteristic time for this process is L^2/D, where L is the distance needed to diffuse, and D is the DNA diffusivity. Assuming a plug flow in the x -direction and that the mass transfer of DNA is diffusion limited, the concentration of DNA stripper, C, is a function of the contact time of the three streams or analogously the distance in the x-direction traveled and is described by the differential equation

$$\frac{dC}{dt} = v_x \frac{dC}{dx} = D \frac{d^2C}{dy^2}$$

, with initial conditions

$$C(y,0) = C_0(y) = \begin{cases} C_0 \; for \; y < \dfrac{W}{4} \\ 0 \; for \; \dfrac{W}{4} < y < \dfrac{3W}{4} \\ C_0 \; for \; y > \dfrac{W}{4} \end{cases}$$

, and boundary conditions

$$\frac{dC}{dy}(y = 0, t) = \frac{dC}{dy}(y = W, t) = 0$$

$$\frac{dC}{dx}\left(y = \frac{1}{2}W, t\right) = 0$$

, where *W* is the width of the channel in the *Y*-direction. This differential equation can be solved analytically and has the solution,

$$C(y,t)/C_0 = \frac{1}{2} + \sum_{n=1}^{\infty} \left\{ \frac{2}{n * \pi} \left[sin\left(\frac{n\pi}{4}\right) - sin\left(\frac{3n\pi}{4}\right) \right] e^{-\frac{n^2\pi^2\mathcal{D}}{W^2}t} \, cos\left(\frac{n\pi}{W}y\right) \right\}$$

The solution of this problem is shown in Figure 3.2 assuming a radius of gyration of 10 nanometers of the DNA to compute it's Einstein-Stokes diffusivity.

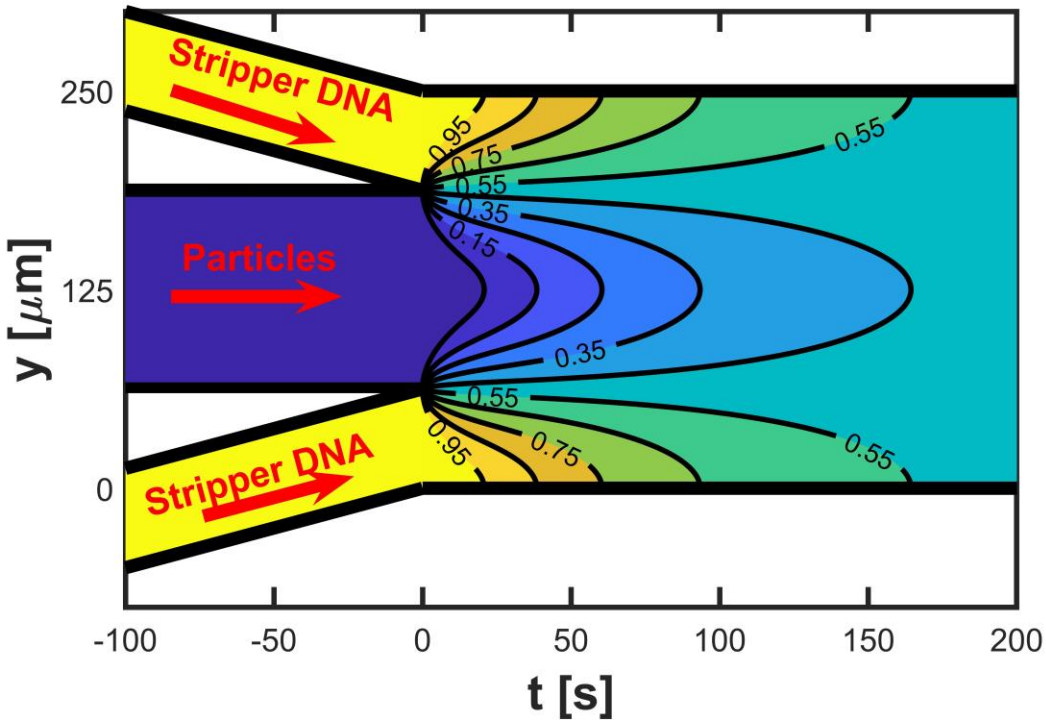

Figure 3.2 Solution to diffusion limited mixing of Stripper DNA throughout the microfluidic channel width. The contour levels indicate the normalized Stripper DNA concentration, $C(y, t)/C_o$. A radius of gyration of 10 nanometers was assumed to determine the Einstein-Stokes diffusivity.

For the microfluidic channel channels used in this dissertation, typical dimensions are 250 μm wide by 60 μm high by 4 cm long, and typical flow rates through the device ranged from 0.1 μL to 10 μL, which corresponds to a mean residence time in the channel ranging from ~0.06 to 6 seconds. This means that the particles which stick in the "clotting" region on the glass, will see a spatial variation in stripper DNA concentration along the width of the clot. However, this is not fatal to the multilayer particle deposition experiment, as the stripper DNA only needs to dehybridize the blocker DNA on the particles. With an appropriate DNA design, this could be done at low concentrations. Additionally, the stripper concentration could be increased arbitrarily,

and the chip could be elongated or incorporate in chip mixing to ensure adhered particles become “activated”.

3.3 Particle-to-Particle DNA Tether Strength

An important feature in any potential multilayer particle deposition in a shear flow is, of course, the buildup of subsequent particle layers after the initial monolayer deposition. For this to be possible, the particle-to-particle interaction must be strong enough to hold up against the shear forces exerted on the particle. Here we present a back-of-the-envelope calculation for the critical wall shear rate to tear the *i*th particle layer from the “clot”.

For a particle in a viscous shear flow, the drag force, F_{drag}, scales with $6\pi\eta a\gamma h$, where a is the particle radius, η is the fluid’s dynamic viscosity, γ is the wall shear rate, and h is the wall to particle center distance. The force to instantaneously rupture a DNA bridge, F_{DNA}, can be approximated as $F_{DNA}=\Delta G^{Hyb}/RC$, where ΔG^{Hyb} is the Gibb’s free energy of hybridization and RC is the reactive compliance of the DNA overlap given by Strunz (44), $RC=0.7+n_{BP}0.07$ nm, where n_{BP} is the number of base pairs in the overlap . Then, the number of bridges needed to hold a particle in place is $N\sim F_{drag}/F_{DNA}\sim \gamma h$.

Next, we can estimate the number of bridges between the *i*th and *i-1*th particle. Assume that the two particles are in contact and bridges can form out to the point where they are fully extended between the two particles. For the case where the particle is on the wall, the radius of the base circle of the spherical cap on the particle

where DNA is in range of the DNA on the wall is $r_{W2P}=\sqrt{(2al_{DNA}-l_{DNA}^2)}$, and the area of the spherical cap is $A_{W2P}=\pi(r_{W2P}^2+l_{DNA}^2)$, where l_{DNA} is the fully-extended length of the DNA bridge. Similarly, for the particle-to-particle case, $r_{P2P}=0.25a^{-1}\sqrt{(l_{DNA}(4a+l_{DNA})(2a-l_{DNA})(2a+l_{DNA}))}$, and $A_{P2P}=2\pi(a^2-a\sqrt{(a^2-r_{P2P}^2)})$. Then to determine the number of DNA strands available, we can simply multiply the DNA areal density on the relevant surfaces by the area of this spherical cap. This geometric analysis is shown schematically in Figure 3.3, for a particle of radius 550 nanometers, and a DNA bridge with fully extended length of 50 nanometers. This analysis will overestimate the number of DNA strands available to bind, as full extension of the DNA strands is entropically unfavorable and there is a steric repulsion preventing surface-to-surface contact.

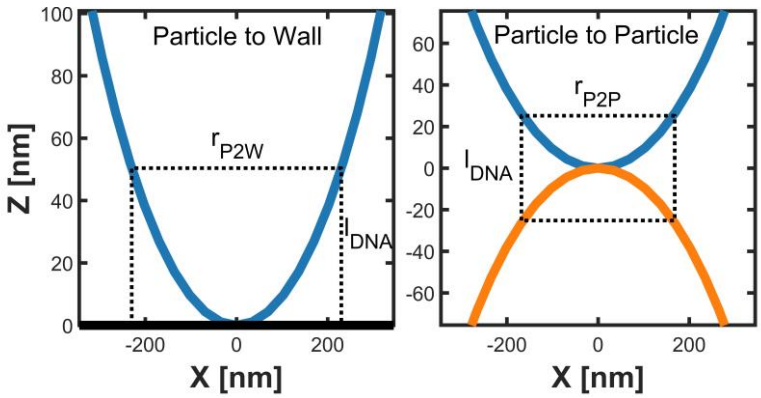

Figure 3.3 Geometric consideration for the size of the spherical cap of DNA available for binding between a particle and a planar wall and a particle to another particle for a 550 nm radius particle. Here the contour length of the DNA bridge, l_{DNA}, is ~50 nanometers. The dashed line indicates the region where the two surfaces are within l_{DNA} of each other.

Now we can estimate the number of DNA bridges necessary to hold a particle against the shear forces, *N*. Consider that as the particle is being sheared off the below surface, it is also being torqued, so that the DNA strands in the leading edge of the contact region are compressed, the DNA strands in the center of the contact patch are neutral, and the strands towards the trailing edge are stretched. Therefore, we will

assume ~1/3 of the DNA strands in the contact region are holding the particle in place. Additionally, we must consider the mechanical advantage in the problem, the particle acting as a lever for the shear flow to act, while the DNA only acts on the radius of the contact patch. With this, we estimate $N \approx 3F_{drag}a/F_{DNA}r_{P2P}$. N is plotted in Figure 3.4 for a particle of radius 550 nm, a DNA bridge contour length of 50 nm with a 9 base pair overlap and a hybridization energy of -10.7 kCal/mole, similar to the Clot AB system discussed in Chapter 2 , as shown in Table 3.1 and

Table 3.2.

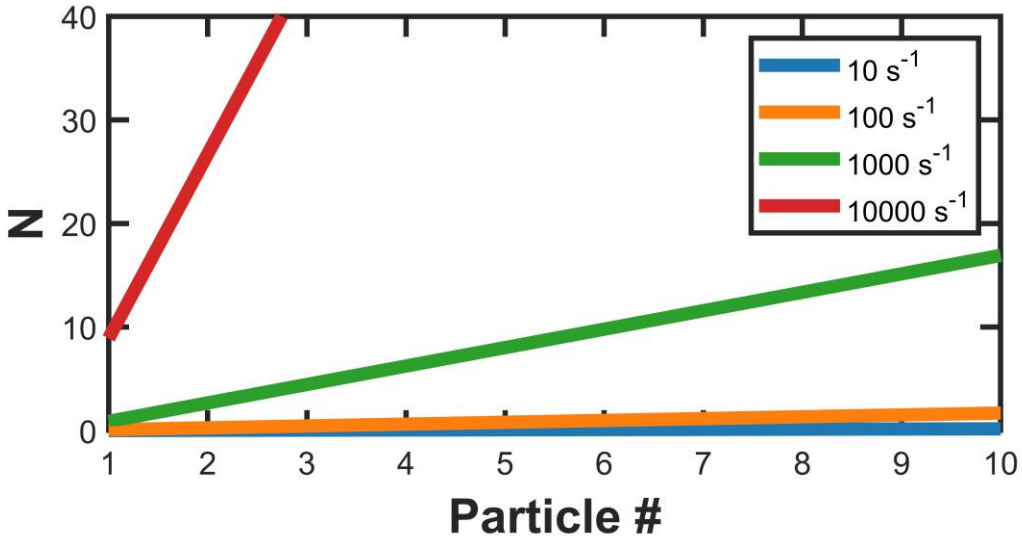

Figure 3.4 Plot of critical number of DNA bridges (N) to hold a particle in place, depending on which layer of particles it is in for a range of bio relevant shear rates. Here, it was assumed that the particle is 550 nm in radius, the DNA bridge contour length was 50 nm, and the DNA bridge had an overlap of 9 base pairs and an energy of hybridization of -10.7 kCal/mole.

With our current method for grafting DNA onto particles, areal densities of ~2000 DNA strands per square micron are typical. This corresponds to ~180 DNA strands in the contact patch between two particles. Considering that with the DNA design used in Chapter 2 , in equilibrium, about half of the DNA strands in the patch will form loops on the particle and the other half will form bridges between particle, meaning we can expect ~90 DNA bridges in equilibrium between particles. Even if we consider that we

overestimated the contact patch size, this suggests that in equilibrium, the DNA ligands can be designed to be sturdy enough to hold the particle in place under bio relevant shear rates.

3.4 Analysis of DNA Kinetics in Particle Clotting System

While the analysis in Sections 3.2 and 3.3 suggest that the Stripper DNA is able to diffuse enough in the channel to remove the Blocker DNA from stuck particles to turn on their particle-to-particle interactions, and that in equilibrium, this interaction should be strong enough to allow for the buildup of the microparticle "clot", experiments did not show any evidence of this build up.

To analyze this further, we considered the kinetics of the particle-to-particle interaction. Consider the case where the stuck particle, particle 1, has been stripped completely of its blocker DNA and the free stream particle, particle 2, has not been stripped of any of the blocker strand. Additionally, let us assume the two particles are in contact with each other. Then we have the following DNA hybridization reactions which define this system.

$$A_i + B_i \rightleftharpoons A_i B_i$$

$$B_2 Block + Stripper \longrightarrow B_2$$

, *i=1,2* indicates which particle that strand is anchored to. We can assume the forward rate of hybridization, k_f, is 6e5 /mole-second (35) , the backward rate of dehybridization, k_b, is determined by the energy of hybridization (Table 3.1), and the

toehold mediated strand exchange reactions rate constant, k_f^{TMSE}, is *~1/(3*9)*k_f* (115). Combining this with the initial conditions that *A_1, B_1, and A_1B_1* are in chemical equilibrium, all the B_2 strands are in the *B_2Block* complex, we can numerically integrate the relevant rate equations.

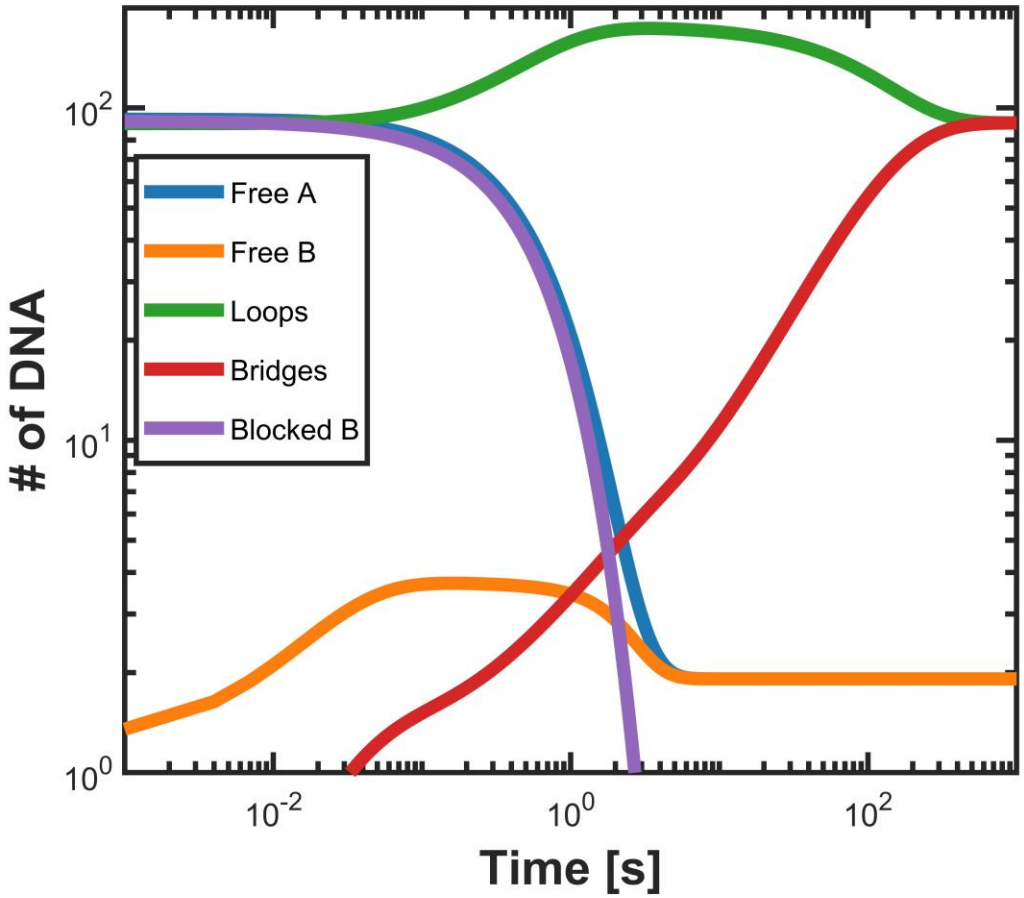

Figure 3.5 Kinetic analysis of DNA Clotting system. The # of DNA refers to the total number of DNA in each state in the contact patch between two 550 nm radius particles with total DNA densities of 2000 per μm^2. Initially, one particle is assumed to have its *A* and *B* DNA strands in equilibrium while the other particle has all its *B* strands blocked. The stripper DNA concentration is assumed to be 100 μM. Loops refer to *AB* complexes on a single particle, while bridges span the two particles.

As shown in the graphed solution to this problem, Figure 3.5, the formation of DNA loops on a single particle significantly impedes the formation of bridges. Initially, the particle that is already stuck to the surface is has almost all of its DNA strands in a loop state, while the seconds particles *B* DNA is almost entirely blocked. As the stripper DNA works to unblock the second particle, these now free *B* DNA strands tend to form loops with the available *A* strands on the same particle. In fact, in this system, it takes ~30 milliseconds for the first bridge to form, ~1 second for the first three bridges to form, and several minutes for the system to fully equilibrate. By comparison, at a wall shear rate of 100 s^{-1}, a particle at a height of 3/2 of its radius travels its full diameter in ~ 6 milliseconds, and travels the full contact patch length from Section 3.3 in ~4 milliseconds. This calculation points to the kinetics of the particle-to-particle interaction being what prevents "clot" formation for this system as currently conceived.

3.5 DNA-Particle Clotting System

As shown in the previous sections, the DNA clotting system as designed, is severely limited by the self-passivation of particles preventing particle-to-particle binding. One simple way to overcome this may be by using particles with a stoichiometry of *A* to *B* DNA not equal to 1:1, but rather equal to 1:2. In this way, as particles are introduced to the channel, they would still have their *B* DNA blocked allowing for the *A*-*B Glass* DNA complex to form and thus the first layer of particles to deposit. However, as the *B* DNA became unblocked, it would still form loops with the *A*

DNA on the same particle, but would be in excess on the surface, so after this self-passivation, there would still be *B* strands available for "unactivated" particles to bind to. Figure 3.6 shows the results of redoing the analysis from Section 3.4 for a particle DNA stoichiometry of 1 *A*:2 *B* DNA.

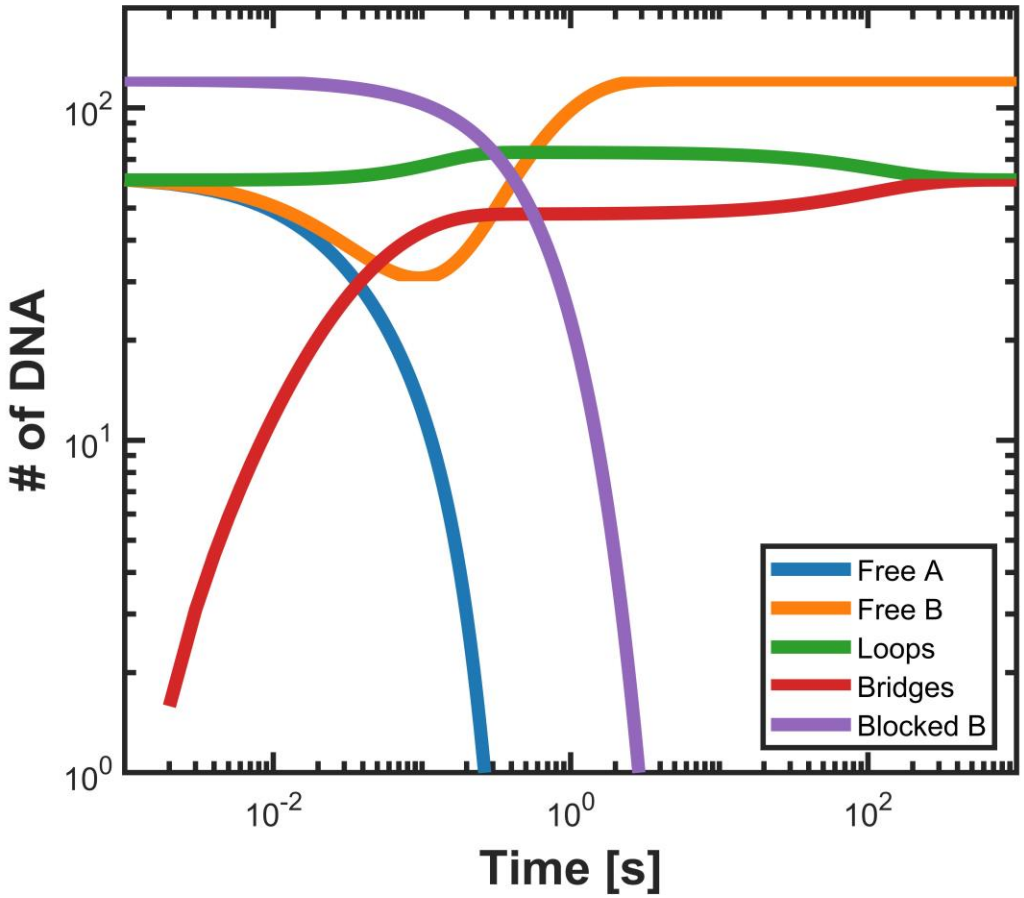

Figure 3.6 Kinetic analysis of DNA Clotting system with particles having 1:2 *A:B* DNA stoichiometry. The # of DNA refers to the total number of DNA in each state in the contact patch between two 550 nm radius particles with total DNA densities of 2000 per μm^2. Initially, one particle is assumed to have its *A* and *B* DNA strands in equilibrium while the other particle has all its *B* strands blocked. The stripper DNA concentration is assumed to be 100 μM. Loops refer to *AB* complexes on a single particle, while bridges span the two particles.

This change in DNA stoichiometry on the particle allows for an order of magnitude faster bridge formation compared to when the A and B DNA are in equal concentrations on the particle. In fact, in the ~4 milliseconds that a particle takes to pass a particle stuck to the glass, ~4 DNA bridges can form slowing the particle down and allowing for subsequent bridges to form. This indicates that reformulating the particles to have this imbalance in DNA may allow for future DNA particle clotting experiments.

3.6 Conclusion

In this chapter, we discussed the challenges associated with DNA mediated particle-clotting in a shear flow. The necessary criterion for this system to work are: 1. a strong particle-glass interaction which was verified and used in Chapter 2 ; 2. Particles that do not aggregate prior to the experiment or in solution, but can be "activated" to induce particle-to-particle interactions once adhered to the "clot", which can be achieved by perfusing a stripper strand through the outer channels of the device, as discussed in Section 3.2 ; 3. Fast particle-to-particle binding kinetics to allow for particles in the shear flow to form enough bridges with adhered particles to adhere to the clot. Our analysis suggests this last requirement can be achieved by adjusting the stoichiometry of the two strands of DNA on the particle. Additionally, while our current chemistry for grafting DNA on to particles yields ~2000 strands per μm^2, the Pine group has reported significantly higher DNA densities for similar particles (116), which could be used to both increase the kinetics and the strength of particle-to-particle binding.

Chapter 4 Shear-driven Rolling of DNA-adhesive Microspheres

Christopher L Porter,[1] Scott Diamond[1], Talid Sinno[1] and John C. Crocker[1*]
[1]Department of Chemical and Biomolecular Engineering, University of Pennsylvania, Philadelphia, PA 19104
*Correspondence: jcrocker@seas.upenn.edu

4.1 Abstract

Many biologically important cell binding processes are multivalent, such as the rolling of leukocytes in the vasculature, and have been challenging to capture with a physical simulation. Here we present a cell-free model for such rolling, consisting of polymer microspheres whose adhesion to a glass surface is mediated by complementary synthetic DNA strands. For certain values of the DNA constructs' binding free energy, force sensitivity and shear rate, we observe robust rolling behavior. A simulation framework developed to model leukocyte rolling, adhesive dynamics, accurately captures the mean rolling velocity and lateral diffusivity of the experimental particles, using known values of the relevant experimental parameters. Moreover, the model captures the velocity variations seen within the trajectories of single particles. Particle-to-particle variation are attributable to plausible but minute differences in particle characteristics. Overall, our findings confirm that state of the art adhesive dynamics simulations are able to complex physics of particle rolling, boding well for their application to understanding rolling leukocytes.

4.2 Introduction

Blood is a dauntingly complex system for modelling, involving many-body hydrodynamics, cellular viscoelasticity, intracellular signaling, extracellular expression of reactive soluble species, as well as cell-cell binding and adhesion. Understanding of the binding processes is further complicated by cell-cell interactions typically being multivalent, whether in the context of the deposition/clotting of platelets (117) or the rolling adhesion of leukocytes (16, 118-120). These cellular adhesion processes have been studied in vitro for decades (17-19), and recapitulated using cell-free models consisting of synthetic microspheres grafted with the relevant adhesion ligands and receptors, with respectable agreement with computational models that include both explicitly represented ligands and the hydrodynamic and surface forces on the particles, termed adhesive dynamics (118, 121). In adhesive dynamics, the ligand bonds form and rupture stochastically according to their force and biomechanics, and while formed exert forces and torques on the particle. Many early studies have had difficulty comparing experimental and simulation results because of a lack of independently measured ligand properties, the inherent complexities of cell signaling pathways, significant cell-to-cell heterogeneities, and a lack of computational power.

Cell-free model systems of cell deposition and rolling remain limited by the lack of knowledge regarding many ligand properties, suggesting the use of a model ligand with well-known mechanochemistry. The deep understanding of DNA thermodynamics

and stereochemistry has led to an ever-increasing number of nanoscale engineering applications, including colloidal self-assembly (32, 122-125), DNA microarray technology (126, 127), aptamers (128), and targeted drug delivery (129). Specifically, the force-extension behavior and force-sensitivity of the DNA duplex have been extensively studied at the single molecule level using atomic force microscopy (4, 44, 46, 47), optical tweezers (43) and molecular simulation (45), and can be well modeled by the Bell model (4). The multivalent interactions and binding kinetics of particles bearing complementary DNA strands have been studied via shear force induced unbinding (14, 15), and equilibrium binding and unbinding (NYU) (35, 130).

Here we report a cell-free model for intravascular rolling using synthetic microspheres and complementary DNA strands as a model adhesion ligand. In a microfluidic chamber, progressively higher shear rates reveal a firm binding regime, a robust rolling adhesion regime, followed by unbinding from the surface. Two DNA model ligands are investigated, one where the DNA overlap is parallel to the molecular tension, and one with the DNA overlap orthogonal to the tension; resulting in a three-fold difference in force-sensitivity for duplex rupture. As expected, we find a strong dependence of rolling velocity on shear rate, and moreover, find a significant degree of particle-to-particle variation in both the rolling velocity and lateral diffusivity. A state-of-the-art adhesive dynamics model, coupled to parameter values consistent with independent measurements, captures the experimentally observed rolling regime, mean rolling velocity and lateral diffusivity, for both model ligands. It also reproduces

the shear rate-dependent dispersion in single-particle rolling velocities. Using the model, we then investigate potential origins for the particle-to-particle variation.

4.3 Materials and Methods

4.3.1 Experimental Materials and Methods

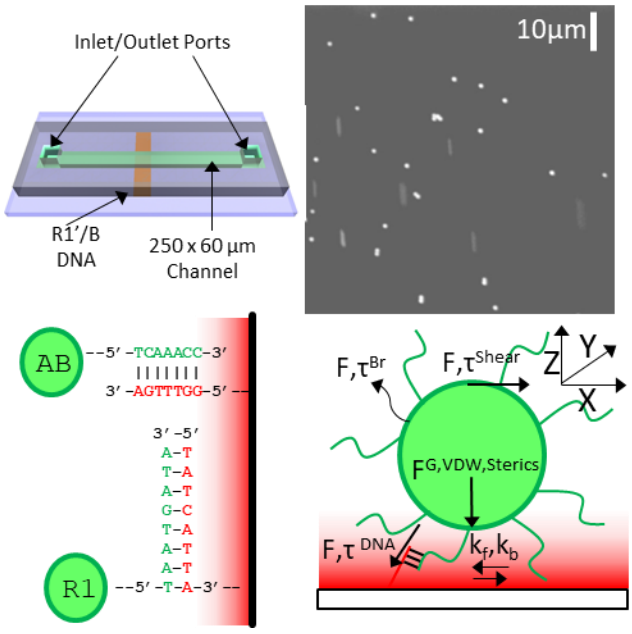

Figure 4.1(Top Left) Schematic of PDMS microchip used for particle rolling experiments. (Top Right) Example of typical images captured during experiment. (Bottom Left) Schematic of the two DNA systems used in the experiment. (Bottom Right) Schematic of the overall adhesive dynamics simulation.

4.3.2 DNA Architecture

For the particle rolling experiments, four DNA systems were studied, R1, AB, A11B, and A3B shown in Figure 4.1. The R1 system consisted of an 8 base pair overlap, with $\Delta G^{27^{\circ}C}_{200mM\ NaCl}$=-6.0 ± 0.3 kCal/mole as calculated using NUPACK (114). Additionally,

the hybridized region was designed to be perpendicular to molecular tension applied between anchor points on the glass and the particle, Figure 4.1. The AB systems, in contrast, had a hybridized region in line with the molecular tension. The AB system consisted of a 7 base pair overlap, with $\Delta G^{27^\circ C}_{200mM\ NaCl}$=-7.2 ± 0.3 kCal/mole, while the A11B system had an 11 base pair overlap with $\Delta G^{27^\circ C}_{200mM\ NaCl}$=-15.1 ± 0.3 kCal/mole, and the A3B system had a 3 base pair overlap with $\Delta G^{27^\circ C}_{200mM\ NaCl}$=-1.5 ± 0.3 kCal/mole. All DNA strands were obtained from Integrated DNA Technologies, Inc.

Table 4.1 DNA Sequence Design

DNA Strand Name	5' Modification	5'-to-3' Sequence	3' Modification
R1	5'-DBCON	32 T-TAATGATA	
R1'	5'-Cy5	TATCATTA-32 T	3'-ThioMC3
R3 Pull down		TATCATTA-16 A	3-Cy5Sp
A	5'-DBCON	27 T-A-TCAAACC	
A11	5'-DBCON	27 T-A-TCAAACCGCAC	
A3	5'-DBCON	27 T-A-TCA	
B	5'-ThioMC6-D	9 T-GTGC-GGTTTGA	3'-Cy5Sp
B Pull Down		GTGCGGTTTGATAAA	3'-Cy5Sp

4.3.3 Attachment of DNA to Particles

The method for bonding DNA strands to 1.1 µm diameter poly(methyl methacrylate) (PMMA) particles (Bangs Laboratories, Inc, Fishers, IN, PP04N) is adapted from a process reported by the Pine lab (116), and relies on using a strain-promoted

azide-alkyne cycloaddition (SPAAC) reaction to covalently link dibenzylcyclooctyne (DBCO) modified DNA to a di-block polymer which is adsorbed onto a particle.

First, 0.1 g (14.5 µmol) poly (styrene-b-ethylene oxide) (Polymer Source, Dorval, Quebec, Canada, P11110-SEO) was dissolved in 2 mL dichloromethane (Sigma Aldrich, St. Louis, MO, 270997-100ML). Then, 30 µL (215 µmol) of triethylamine (Sigma Aldrich, St. Louis, MO, T0886-100ML) and 42 µL (543 µmol) of methane sulfonyl chloride (Sigma Aldrich, St. Louis, MO, 471259-100ML) was added. This mixture was allowed to react for 24 hours at room temperature with constant mixing. Next, 2 mL of a 3% hydrochloric acid (Fisher Scientific, Pittsburgh, PA, A144-500), 97% methanol (Sigma Aldrich, St. Louis, MO, A452-1) was added. 45 mL of cold diethyl ether (Fisher Scientific, Pittsburgh, PA, E138-1) was added and the polymer was precipitated in the freezer. The resulting pellet was then centrifuged, the supernatant removed, and pellet resuspended with the HCl-MeOH mixture and washed again in diethyl ether. This process was then repeated twice more using only methanol for the resuspension. The washed polymer was then dried under vacuum.

Next, the dried polymer was dissolved in 2 mL dimethylformamide (Sigma Aldrich, St. Louis, MO, 227056-100ML) along with 0.01 g (150 µmol) sodium azide (Sigma Aldrich, St. Louis, MO, S2002-5G). This mixture was then allowed to react for 20 hours at 65 °C with constant mixing, before being washed 3 times using methanol and ether as before. The product was then dried under vacuum for at least 24 hours. The

azidylated polymer was then stored dried in a freezer for up to 6 months, or in de-ionized water at 10 mM for up to 1 month.

To adsorb the azidylated polymer to the PMMA particles, 50 µL of 10% v/v particles was gently mixed with 24 µL of 2 mM azidylated polymer. This mixture was diluted to 500 µL using Tris-EDTA buffer solution (1xTE) (Sigma Aldrich, St. Louis, MO, 93283-500ML). Then, 4 µL of toluene (Sigma-Aldrich, St. Louis, MO, 244511-100ML) along with BODIPYTM 493/503 (Thermo-Fisher, Waltham, MA, D3922) was added. The mixture was gently inverted for 1 hour. After the adsorption was complete, the particles were put in a 90 °C oven for 20 minutes to remove the toluene, and then were washed in 1xTE three times.

Finally, 2 µL of 1000 µM DBCO modified DNA was added to the particles along with 1xTE and NaCl, so that the final solution was 100 mM NaCl and 500 µL total. This solution was allowed to react for four days at room temperature, and then the particles were washed 4 times in 1xTE.

To quantify the DNA yield on the particles, the DNA functionalized particles where incubated with a known quantity of a fluorescently modified soluble DNA strand in a 300 mM NaCl solution. The particles where then centrifuged, and the supernatant analyzed using UV/Vis spectroscopy. Upon comparing the supernatant to known standard concentrations of the probe DNA, it was determined that the particles had ~9,000 DNA/particle.

4.3.4 Preparation of PDMS devices and DNA attachment to glass

PDMS microfluidic channels were manufactured using standard soft lithography techniques as previously reported (131). Specifically, 7.5 mL of Sylgard® 184 Silicone Elastomer Curing Agent was stirred into 75 g of Sylgard® 184 Silicone Elastomer Base (Dow Corning Corporation, Midland, MI, 3097366-1004). A vacuum was applied for 1 hour to remove all air bubbles, and then the mixture was gently poured onto a silicone master and baked at 60 °C until firm, ~1 hour. The device was then cooled, cut to size, and a 0.75 mm biopsy punch was used to create inlet and outlet ports. The devices were cleaned, before and after each use, via sonication for 30 minutes each in acetone, then 90% ethanol and 10 % deionized water, and finally deionized water, and then allowed to dry completely. The resulting channels were 60 µm high by 250 µm wide.

To silanize the glass slides, the procedure from Rogers et al. (132) was adapted, as previously reported (131). Glass slides (Fisher Scientific, Pittsburgh, PA, 12-550B) were soaked in 28% ammonium hydroxide (Fisher Chemical, Pittsburgh, PA, A669S-212) overnight, then rinsed thoroughly in deionized water (from Barnstead EasyPure Model D7031 water purification system). They were then rinsed briefly in 200 proof ethanol (Decon Labs, King of Prussia, PA, #2716), before being incubated for 30-60 minutes in a solution of 95% ethanol, 5% de-ionized water, 16 mM acetic acid (Fisher Scientific, Pittsburgh, PA, A38-500), and 1 vol% (3-mercaptopropyl) trimethoxy silane (Sigma-Aldrich, St. Louis, MO, 175617-25G). Slides were then rinsed in the 95% ethanol, 5% de-

ionized water, 16 mM acetic acid solution and cured in a 110° oven for 1 hour. Slides were then stored in a desiccator for up to 48 hours.

Disulfide functionalized DNA strands were ligated to the silanized glass slides following the method adapted from Rogers et al. (132) and reported previously (131). Briefly, the 1 µL of 1000 µM disulfide DNA was added to 10 µL of 500 mM carbonate buffer pH = 9.95 (Fisher Scientific, Pittsburgh, PA, S263-500). A PDMS device was then positioned on the activated glass slide, and the DNA solution was loaded into the channel and allowed to react in a humidified chamber for 2 hours. The channel was then flushed with a solution of 10 mM tris(hydroxymethyl)-aminomethane (Aldrich, St. Louis, MO, 154563-100G) pH 7.5, 150 mM NaCl, 0.05% Tween 20 (Acros, Pittsburgh, PA, 23336-2500). The PDMS device was then removed, and the glass slide was thoroughly desalted in methanol before being allowed to dry. The DNA density on the glass was measured via fluorescent microscopy compared to known standard concentrations and showed ~7200 DNA/ μm^2.

4.3.5 Quantification of DNA Availability on the Glass

To quantify what fraction of the DNA on the glass was available for binding, devices were prepared as described. Then, the channel was filled with a complementary, fluorescently tagged DNA strand in 300 mM NaCl, pH 7.5 PBS. The solution was allowed to hybridize for ~5 minutes, before being flushed with phosphate buffered saline to remove any non-hybridized DNA. The fluorescent intensity was then

measured, followed by a flushing of the channel using DI water, in order to dehybridize the DNA strands. Again, the fluorescent intensity was measured, and compared to the original to determine the areal density of DNA strands available for binding on the glass. We found ~10% of the DNA was available for binding, consistent with value reported by Rogers et al. (132).

4.3.6 Particle rolling experimental procedure and analysis

For the rolling experiments, first a microfluidic device was placed on the glass slide, such that its channel intersected the stripe of DNA ligated to the glass, Figure 4.1, and then primed with 1xTE. The DNA stripe was then located using fluorescent microscopy, and a 0.01 particle v/v%, 200 mM NaCl, 10 mM phosphate buffer pH 7.4 solution was pumped through using a syringe pump at wall shear rates ranging from 10-1000s^1. Particles were imaged at between 30 and 60 frames per second. At shear rates of 10 s^{-1} and below, both DNA systems showed only firm particle adhesion, while at shear rates of 1000 s^{-1}, and above, particles did not significantly interact with the surface.

A feature finding algorithm (88) was then used to track the particle trajectories. A hidden Markov model based on the velocity distributions was used to categorize particles as either firmly adhered, rolling, or free stream, and the firmly adhered particles were used as fiduciaries to dejitter the particle trajectories. Finally, the

trajectories were rotated so that the net motion of the ensemble of particles was purely in the X-direction.

4.3.7 Simulation theory and methodology

To simulate a particle rolling on a sphere, we implemented an event-tracking Brownian adhesive dynamics simulation. Overall, the model consists of a spherical particle covered in explicitly represented DNA strands under a shear flow over an infinite planar wall, Figure 4.1. The solutions derived by Goldman, Cox and Brenner (21-23), as described by Hammer (133), for the viscous motion of a sphere near a wall were used to compute the hydrodynamic forces and mobility matrix of the particle. The solution to the Langevin equation for a particle near a wall, as derived by Maffettone (24), was used to compute the Brownian translational and rotational displacements of the particle. The DNA strands on the particle were modeled as random gaussian coils, while the DNA on the wall was modeled as a continuous concentration field corresponding to tethered Gaussian coils. When a particle-wall bridge is formed, this bridge exerts forces and torques on the particle, according to the force-extension curve of a worm-like chain. The force accelerated unbinding of the bridges was modeled using the Bell model (4). Electrostatic forces are assumed to be negligible at the high ionic strengths used in the experiment. The Van der Waals forces were considered, however our analysis showed that its effect, modulated by the value of the Hamaker constant, was minimal for low Hamaker constant values, and unphysical results emerged for

higher Hamaker constant values, with no intermediate regime. Thus, the Van der Waals forces were not included in the final simulation. The details of each portion of the model are described in more detail in the Supplementary Material.

4.4 Results and Discussion

In this section we present experimental results of our in vitro particle rolling experiments. Particles coated in DNA were perfused through a microfluidic channel with a complementary DNA functionalized surface. We report the behavior of the four DNA systems investigated, and for the two systems which exhibited rolling, we report the log-mean rolling velocity and lateral diffusivity. In analyzing the experimental results, we note a significant degree of particle-to-particle variation in both the rolling velocity and lateral diffusivity. To compare the experimental data to our model, we use statistical methods to remove the effect of this variation from the experimental data. We then implement a quantitative fitting methodology to fit adhesive dynamic simulations to the experiment and find good agreement in the particle rolling velocity, diffusivity and individual particle velocity dispersion using parameter values within the bounds of independently reported literature values. For the parameters which are experimentally controllable through DNA architecture design and experimental preparation, we discuss the model's sensitivity. Finally, using the results from the adhesive dynamics simulations, we discuss potential sources of the observed experimental particle-to-particle variation.

4.4.1 *In Vitro* Particle Rolling Experiments

Microfluidic experiments were performed using DNA coated microbeads perfused through a channel over a complementary DNA functionalized glass slide at shear rates ranging from 10 to 1000 s^{-1}. In total, four DNA systems were investigated, the R1 system with an 8 base pair overlap perpendicular to the bead-to-glass bridge, the AB system with a 7 base pair overlap in line with the bridge, its derivatives, the A11B system with an 11 base pair overlap and the A3B system with a 3 base pair overlap. The R1 and AB systems both exhibited dynamic particle rolling regimes at the studied shear rates. Neither of the A3B or A11B systems showed any particle rolling behavior and will not be discussed further in this article.

Figure 4.2 shows sample trajectories of particles that exhibit some rolling behavior at various shear rates for the R1 (Top) and AB (Bottom) DNA systems. At lower wall shear rates, both systems show intermittent rolling behavior, or rolling before arresting. At intermediate shear rates, particles arrested much less frequently, and displayed prolonged rolling behavior. As the shear rate increased further, particle rolling became increasingly rare, until eventually no particles interacted with the surface.

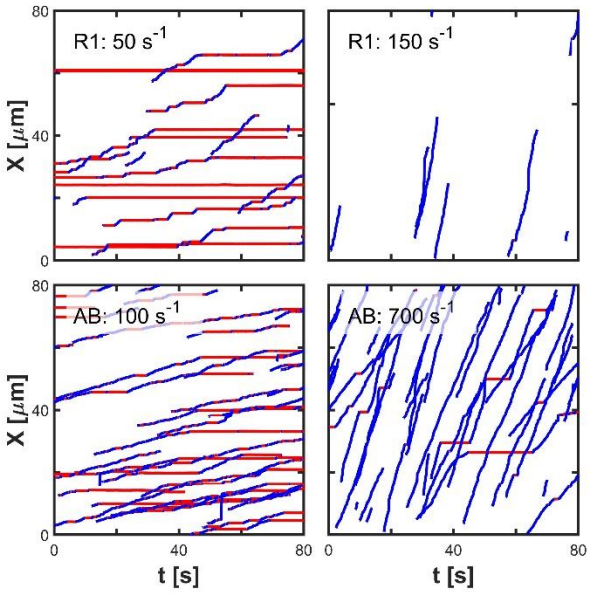

Figure 4.2. Experimental trajectories of particles for both the R1 and AB DNA system. Particles that did not roll at least 5 μm are excluded. Red portions of trajectories indicate "stuck" particles, while blue portions indicate "rolling" particles, as determined from a Hidden Markov Model based on the particle velocity. At relatively low shear rates (Left Panels), the particles tended to exhibit short rolling excursions before either firmly adhering to the surface or detaching from the surface entirely. At higher shear rates (Right Panels), particles tend to roll farther, faster, and less intermittently.

While both systems showed this same behavior, the shear rate at which the two systems transitioned between this intermittent rolling and firm arrest to rolling to pure advection differed, with the R1 system arresting below 25 s^{-1} and freely advected above 200 s^{-1}, whereas the AB system firmly arrested below 100 s^{-1} and freely advected above 900 s^{-1}. As shown in Figure 4.3, the velocity of rolling particles depends on the shear rate, with higher shear rates leading to faster rolling behavior and a broader distribution of velocities.

Next, we looked at the mean squared displacements in the downstream (X) and transverse (Y) direction (Figure 4.3) and observed that the particles diffuse laterally as they roll along the surface. By fitting the ensemble lateral mean squared displacement to $\Delta Y^2 = 2D_Y \Delta t + Constant$, we extracted a lateral diffusivity of the particles at each shear rate. For each system, we see a trend that as shear rate increases, and thus the rolling velocity, the particle's lateral diffusivity also increases.

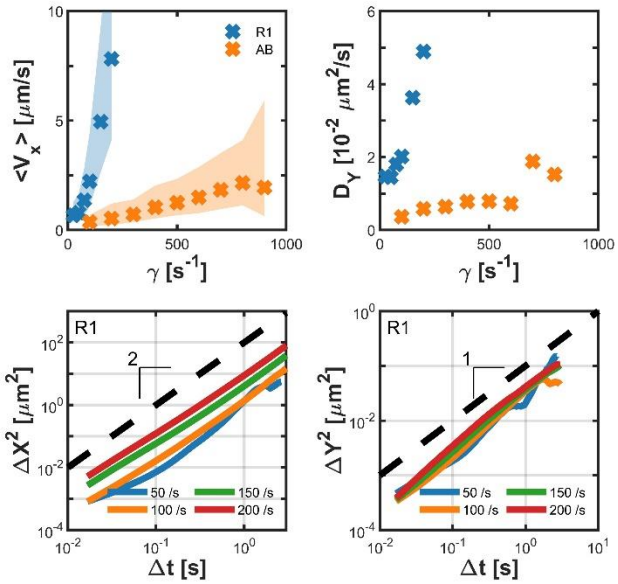

Figure 4.3. (Top Left) Log-mean downstream rolling velocity of particles over range of shear rates, γ. The bands represent one log standard deviation of the ensemble's velocity distribution. (Top Right) Lateral particle diffusivities over range of shear rates. The diffusivities where computed by fitting the mean squared displacement to $\Delta Y^2 = 2D_Y \Delta t + Constant$. (Bottom Left) Ensemble mean squared displacement in the downstream direction for selected shear rates. The dashed line is an eye-guide representing ballistic motion. (Bottom Right) Ensemble mean squared displacement in the lateral direction for selected shear rates. The dashed line is an eye-guide representing purely diffusive behavior. In each case, there is no detectable noise-floor resulting from the particle tracking.

4.4.2 Effect of Particle-to-Particle Velocity and Diffusivity Variations

Analyzing the velocity distributions of individual particles, Figure 4.4, we observe that while the shapes of the distributions of individual particles at a given shear rate are consistent, they appear to be shifted, indicating that there is a distribution of mean rolling velocities for individual particles. In order to compare the experimental results to the adhesive dynamics model, it is important to account for and remove this effect. The individual distributions can be shifted to the global log-mean value, resulting in a collapse of the curves. The distribution of this shifting parameter for individual particles was fit to a log-normal distribution. While the mean of this distribution varied with shear rate, owing to under sampling of “fast” particles and data-attrition on stuck particles, the log standard deviation of the distribution is independent of shear rate and the DNA system used at ~0.5.

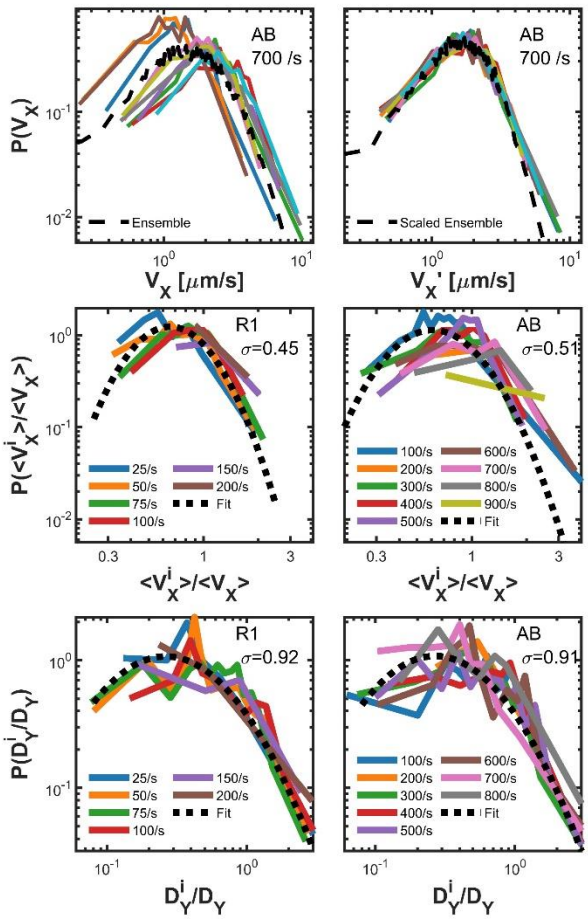

Figure 4.4 (Top Left) Rolling velocity distributions of individual particles for the AB DNA system at a shear rate of 700 s^{-1}. The dashed line represents the ensemble distribution. (Top Right) Individual particle rolling velocity distributions after rescaling to the ensemble log-mean velocity. The dashed line shows the ensemble distribution after this rescaling. (Middle) Probability distribution function of the ratio of an individual particles log-mean rolling velocity compared to the ensemble for the two DNA systems at each examined shear rate. The dashed line shows the log-normal fit over all shear rates. The displayed σ values represent the standard deviation of the natural log of the fit. (Bottom) Probability distribution function of the ratio of an individual particle's lateral diffusivity to the lateral diffusivity derived from the ensemble mean square displacement for the two DNA systems at each shear rate. The dashed line is a log-normal fit over the data for all shear rates, with a log standard deviation displayed by σ.

Similarly, for a given shear rate, measuring an individual particles lateral diffusivity reveals a log-normal distribution of diffusivities, with a log-standard deviation

of ~0.9 which again is independent of shear rate and DNA architecture, Figure 4.4. Additionally, for a given particle, the velocity scale factor and the diffusivity scale factor scale together with an exponent of ~0.5, Figure 4.5, indicating that the particles that roll faster also tend to diffuse more rapidly. When comparing the particle diffusivity between experiments and simulation, we will use the log-mean of the individual particle diffusivities.

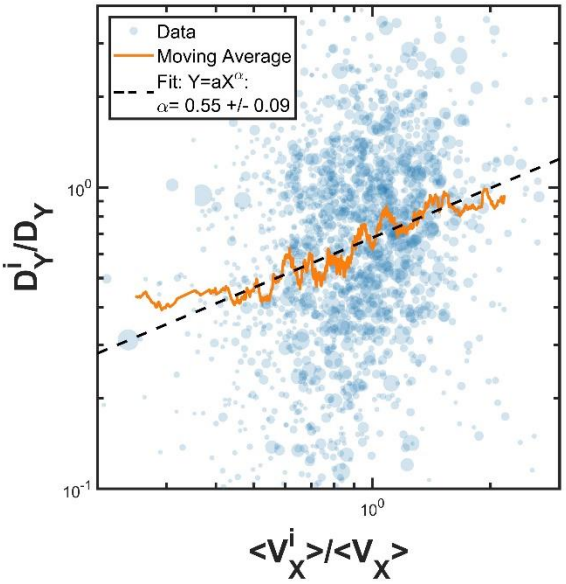

Figure 4.5 The scatter represents show the individual particles ratio of log-mean rolling velocity and lateral diffusivity compared to the ensemble at that shear rate and DNA system, for every shear rate and both the R1 and AB system. The size of each point corresponds to the duration in time of that particle's trajectory. The solid orange line shows the moving log-mean of the data, while the dashed line is a fit of a power law to the scattered points.

Looking at the mean rolling velocity of particles as a function of their X and Y position on the cover slip, Figure 4.6, we can rule out long range DNA gradients on the glass as the cause of the distribution of particle velocities. Similarly, by looking at the

autocorrelation function of the rolling velocity of particles versus distance traveled, we note that the rolling velocity immediately decorrelates, ruling out short range DNA gradients on either the particle or the glass as effecting our system.

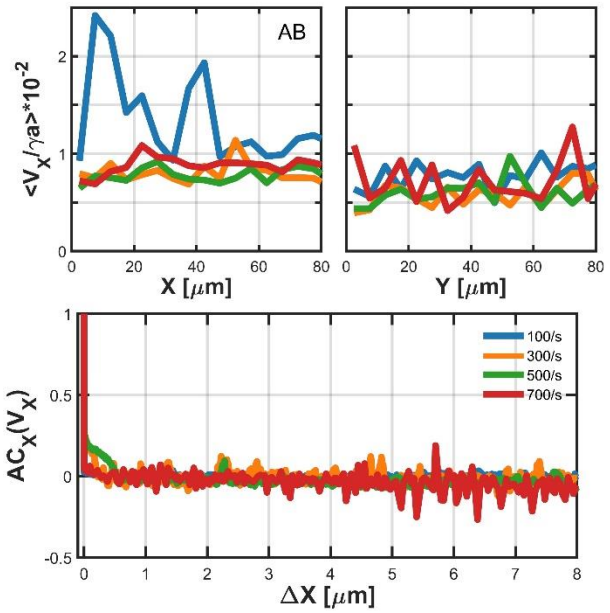

Figure 4.6 Dimensionless log-mean rolling velocity of particles as a function of downstream (Top Left) and lateral (Top Right) position in the observed region for selected shear rates of the AB system. (Bottom) Autocorrelation function of the ensemble of particle's rolling velocity as a funciton of distance traveled downstream for selected shear rates.

4.4.3 Quantitative Fitting of Adhesive Dynamics Simulations to Rolling Experiments

To fit the simulation model to the experimental data, first model parameters were chosen from literature values or measured as shown in Table 4.2. Then, a fitting operation was done on the log-mean particle velocities as a function of shear rate while varying the DNA's Gibb's free energy of hybridization (ΔG), reactive compliance (RC),

and the areal density of DNA available for hybridization on the glass (ρ_G^{DNA}). This was done for both the R1 and AB experimental system, with areal density of DNA on the particle, ρ_P^{DNA}, being a constant across the two systems. It should be noted that this fitting was extremely computationally intensive with over 70,000 separate simulations being done corresponding to over 340 hours of simulated particle trajectories.

Table 4.2. Model Parameters

Model Parameter, Symbol	Value	Reference
Radius, a	550 ± 50 nm	Bangs Laboratories
AB DNA Hybridization Energy, ΔG^{AB}	7.2 ± 0.3 kCal/mole	(114)
R1 DNA Hybridization Energy, ΔG^{R1}	6.0 ± 0.3 kCal/mole	(114)
Hybridization Rate, $\mathrm{k_f}$	6e5 ± 2e5 $M^{-1}s^{-1}$	(35)
Particle DNA Density, ρ_P^{DNA}	2350 ± 200 μm^{-2}	Measured
Glass DNA Density, ρ_G^{DNA}	7200 ± 1000 μm^{-2}	Measured
Glass DNA Availability, α_G^{DNA}	10% ± 5%	Measured
AB DNA Reactive Compliance, RC^{AB}	2.5 ± 1.1 nm	(44)
R1 DNA Reactive Compliance, RC^{R1}	1.2 ± 0.5 nm	(44)
ssDNA Kuhn Length, l_K	5 nm	(134)
ssDNA Contour Length, l_{BP}	0.63 nm/Base Pair	(134)
Temperature, T	300 K	Measured
Viscosity, μ	8.9e-4 Pa-s	(135)
Particle Density, ρ^{PMMA}	1.2 g/mL	(135)
Fluid Density, ρ^{H_2O}	1.0 g/mL	(135)
Maximum Time Step, Δt_{Max}	1e-4 s	
Maximum Displacement, $\Delta \mathrm{x_{Max}}$	1 nm	

Figure 4.7 shows the heat map of the quality of fit between the experimental data and the simulation for a range of simulation parameters. As the figure shows, the simulation fits the experimental data over a range of ΔG, RC, and ρ_G^{DNA} values. Including the known variation in the experimental rolling velocities for an individual particle in the fit does not significantly change the shape of the heat maps. However, by constraining these values to within the known uncertainties from measurements and literature values and considering the experimental particles behavior at low and high shear rates, either all stuck or all unbound, respectively, we can select a best fit. Additionally, it is not possible to fit the model to the experimental data with no force-accelerated unbinding of DNA ($\mathrm{RC} = 0$ case) with plausible values for the other parameters.

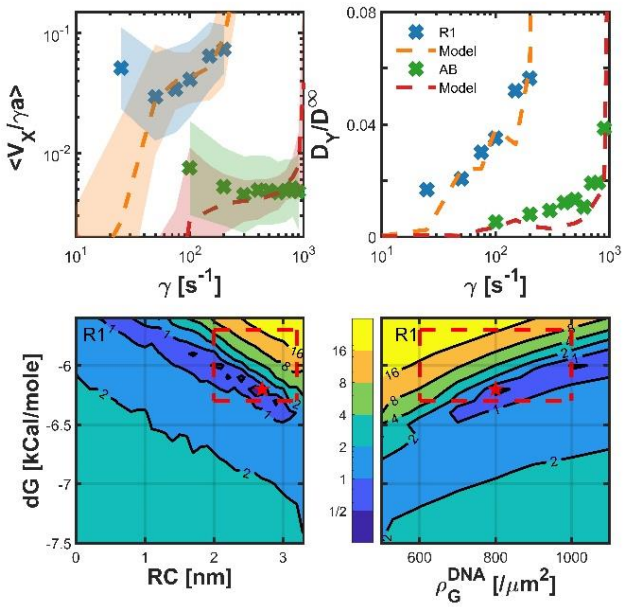

Figure 4.7 (Top Left) The dimensionless log-mean rolling velocity of the experimental systems (AB system in blue x's, AB system in green x's), compared to the best-fit of the simulation data (orange and red dashed lines, respectively), over the range of shear rates. The bands represent one log standard deviation of the velocity distribution. (Top Right) The dimensionless lateral diffusivity of the experimental systems and the

respective best-fit simulation data. D^{∞} is the Stokes-Einstein diffusivity. The experimental diffusivities shown are after rescaling. (Bottom) Heat map of the goodness of fit of the simulation to the R1 system experimental log-mean rolling velocities for the range of studied parameter values. The red star indicates the best simulation values, while the red dashed box indicates the region of plausible parameter values.

Figure 4.7, Top Left and Top Right, show the comparison of the experimental and model log-mean rolling velocities and diffusivities for both DNA systems. Despite not being included in the fitting operation, the model captures the trends of the particle diffusivities well.

Next, we compare the velocity distributions of the experimental system to the model, Figure 4.8. Despite the mean experimental rolling velocity being captured well by the model, the distribution of velocities in the model tends to be narrower than in the experiment. The instantaneous rolling velocity within the model is a strong function of the particles distance from the wall, with a change in distance of ~0.5 nm resulting in ~60% change in velocity. This suggests that the model does not capture the full distribution of velocities because it does not completely accurately capture the distribution of particle-wall distances. This idea will be discussed further later.

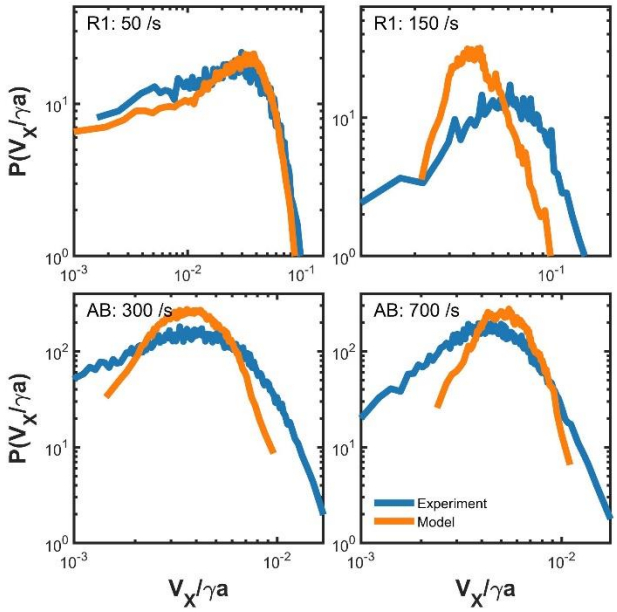

Figure 4.8 Rolling velocity distribution of experimental and simulation particles. For the experimental data, the distributions are from the rescaled data.

4.5 Sensitivity Analysis of Model Parameters

Experimentally, we can control four parameters, the DNA hybridization energy (ΔG) and reactive compliance (RC), through the choice of DNA design, experimental temperature and salt concentration, and the areal density of DNA on the particle (ρ_P^{DNA}), and glass (ρ_G^{DNA}). Therefore, we will discuss the model sensitivity to these parameters, in particular how they pertain to the R1 DNA system.

Figure 4.9 and Figure 4.10 show the dimensionless mean rolling velocity and dimensionless particle diffusivity, respectively, over the range of studied shear rates while varying these parameters individually. The trends in the diffusivity follow the trends in the velocity, and in fact they are linearly correlated. As the force sensitivity of the DNA bridges (RC) increases, the particles begin rolling at lower shear rates, roll at

higher velocities, and are more easily torn off the surface. Similarly, as the energy of hybridization for the DNA decreases (ΔG), decreasing the unforced bridge lifetime, and thus the equilibrium number of bridges formed between the particle and the surface, the particle rolls faster. If the bridge lifetimes are too short, we effectively see no interaction between surface and particle, as expected.

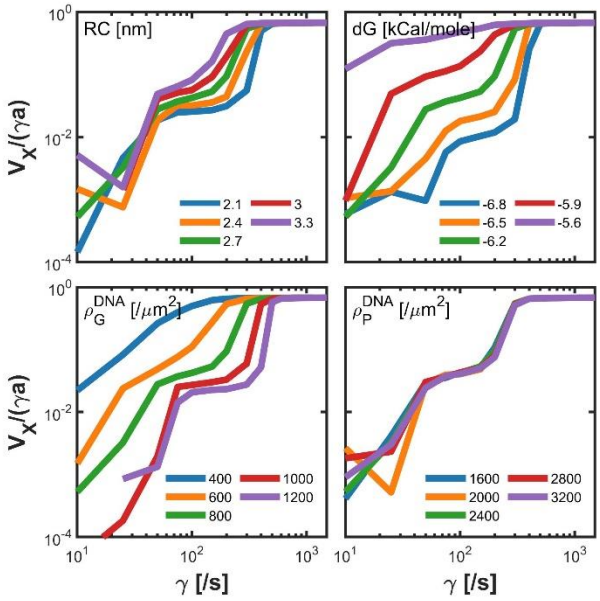

Figure 4.9 Dimensionless velocity of simulated particles for a variety of parameter values. In each plot the indicated parameter was changed while leaving all over parameters constant at the nominal R1 model values.

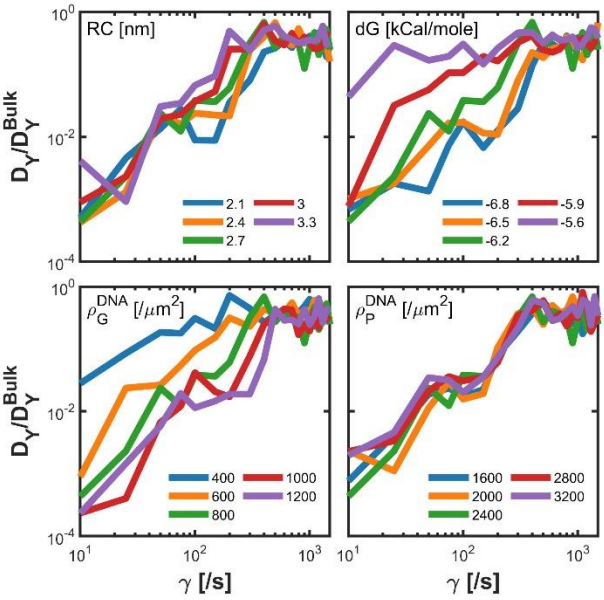

Figure 4.10 Dimensionless Diffusivity of simulated particles for a variety of parameter values. In each plot the indicated parameter was changed while leaving all over parameters constant at the nominal R1 model values.

Since the DNA on the glass (ρ_P^{DNA}) is the limiting reactant, we see a high sensitivity to this parameter. Again intuitively, as there is less DNA on the glass, there are fewer bridges to hold the particle back, and the particle rolls at lower shear rates. Somewhat unintuitively, the model is insensitive to the DNA density on the particle (ρ_P^{DNA}). Since the DNA on the particle is in excess, increasing its value has two competing effects in the model, increasing the effective forward rate of bridge formation (but not the total possible number of bridges), and increasing the steric repulsive force on the particle. These effects balance tend to balance each other out in the model and result in no sensitivity for this parameter, in the case that the DNA on the particle is in excess.

4.5.1 Potential Sources of Particle-to-Particle Variation

As previously discussed, the experimental system shows a significant amount of particle-to-particle variation in the mean rolling velocity and diffusivity, and the model tends to underrepresent an individual particles distribution in velocities. Here we propose two potential causes for this phenomenon. The first is the known particle size distribution. Figure 4.11 shows the effect of varying the particle size by up to twice the coefficient of variation. We see that the model is sensitive to the particle radius, with larger particles rolling faster. As the particle increases in size, the patch on the particle where DNA are close enough to bind to the strands on the glass grows, but the shear force and torque on the particle also increase faster, resulting in a net increase in the particle velocity. However, this bead-to-bead variation can only account for about half of the variation in log-mean rolling velocities we see in the experiment.

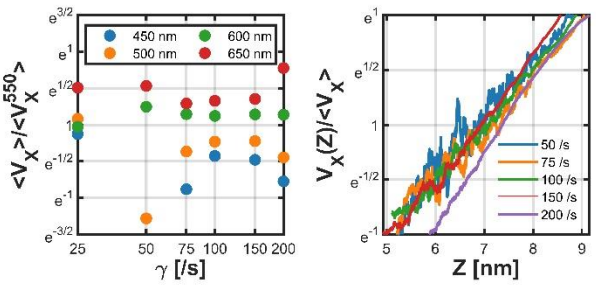

Figure 4.11 (Left) The log-mean rolling velocity of the simulated system for a range of particle radius sizes divided by the log-mean rolling velocity of a 550 nm radius particle. (Right) The simulated log-mean rolling velocity as a function of particle distance from the wall divided by the particle's overall log-mean rolling velocity.

At a given shear rate, the particles rolling velocity is strongly dependent on the particle to wall separation distance, Figure 4.11. This suggests that if there is bead-to-

bead variation in the mean particle-wall separation distance of ~1-2 nm, this could fully account for the variation in particle mean rolling velocities. Such a variation could arise from particle-to-particle surface charge heterogeneities, gel-layer thicknesses, et cetera. Additionally, this result suggests that the model could be tweaked such that the energy potential holding the particle near the wall was shallower, allowing for a wider range of heights to be explored by the particle, and thus a wider velocity distribution, to more closely match the experimental results.

4.6 Conclusion

We have presented an experimental DNA-mediated particle rolling system using two different DNA architectures. This experiment allowed for the comparison of the two systems and the effect of the DNA hybridization energy, ΔG, and the orientation of the DNA overlap to the particle-to-wall bridge. Additionally, in both systems we found that there is a significant bead-to-bead variation in both the log-mean rolling velocity and lateral diffusivity, which cannot be accounted for by DNA heterogeneities on either surface. We then employed an adhesive dynamics simulation to model the experimental rolling data. This model was fit to the log-mean rolling velocities of the particles by varying the DNA hybridization energy, ΔG, force sensitivity,RC, and areal density on the glass and particle, ρ_G^{DNA} and ρ_P^{DNA}. The resulting best-fit parameters were within the uncertainty of independent measurements and literature values. The model showed good agreement with the lateral diffusivities of the experimental systems but does not

quite capture the full individual particle rolling velocity distribution. We then proposed two potential causes for the bead-to-bead variation and the discrepancy in velocity distribution, one being the known bead-to-bead size variation, and the other being the particle-to-wall height distribution during rolling.

4.7 Supplemental Information

Supplemental Information (movies, database files, etc. may be uploaded as separate files). Instructions for Supplemental Information are available at the following link: Supporting Material

4.7.1 Simulation methodology

4.7.1.1 Brownian Particle Hydrodynamics

For our simulations, to solve for the hydrodynamic interactions between the particle, fluid, and wall, we follow the method outlined by Hammer (133) using the solutions from Goldman, Cox, and Brenner (21-23). Specifically, we begin by calculating the mobility matrix, M, of the particle, which expresses how a particles motion responds to applied forces and torques. Since we are considering a spherical particle, M is only a function of the particle distance to the wall, Z.

$$\begin{bmatrix} V_X \\ V_Y \\ V_Z \end{bmatrix} = M \begin{bmatrix} F_X \\ F_Y \\ F_Z \\ \tau_X \\ \tau_Y \\ \tau_Z \end{bmatrix} = \begin{bmatrix} \frac{T_r}{6\pi\mu a D} & 0 & 0 & -\frac{T_t}{6\pi\mu a^2 D} & 0 & 0 \\ 0 & \frac{T_r}{6\pi\mu a D} & 0 & 0 & \frac{T_t}{6\pi\mu a^2 D} & 0 \\ 0 & 0 & \frac{1}{6\pi\mu a\lambda} & 0 & 0 & 0 \\ 0 & \frac{T_t}{6\pi\mu a^2 D} & 0 & -\frac{F_t}{8\pi\mu a^3 D} & 0 & 0 \\ -\frac{T_t}{6\pi\mu a^2 D} & 0 & 0 & 0 & \frac{F_t}{8\pi\mu a^3 D} & 0 \\ 0 & 0 & 0 & 0 & 0 & \frac{1}{8\pi\mu a^2 \chi} \end{bmatrix} \begin{bmatrix} F_X \\ F_Y \\ F_Z \\ \tau_X \\ \tau_Y \\ \tau_Z \end{bmatrix}$$

where T_r, T_t, F_r, F_t, functions of the particle radius and distance from the wall, are interpolated from Goldman, Cox and Brenner (21-23), and D, χ, and λ are calculated as,

$$D = T_t\, F_r - F_t T_r$$

$$\alpha = \ln\left[\frac{(a+h)}{a} + \left(\left(\frac{a+h}{h}\right)^2 - 1\right)^{\frac{1}{2}}\right]$$

$$\chi = \sinh^3\alpha \sum_{n=1}^{\infty} \sinh^{-3}(n\alpha)$$

$$\lambda = \frac{4}{3}\sinh(\alpha) \sum_{n=1}^{\infty} \left[\frac{n(n+1)}{(2n-1)(2n+3)}\right]\left[\frac{2\sinh\big(\alpha(2n+1)\big) + (2n+1)\sinh(2\alpha)}{4\sinh^2\big(\alpha(n+0.5)\big) - (2n+1)^2\sinh^2(\alpha} - 1\right]$$

Once M is calculated, the Brownian displacement of the particle can be determined following the procedure from Maffettone (24) for a spherical particle. Namely, first the square root of M, m, is determined such that

$$M = m * m^T$$

Then, the Brownian translational, Δr_B, and rotational, $\Delta\Theta_B$, forcings are calculated as,

$$\begin{bmatrix}\Delta r_B \\ \Delta\Theta_B\end{bmatrix} = (2k_BT\Delta t)^{0.5} m \begin{bmatrix}\Delta N_1 \\ \Delta N_2\end{bmatrix}$$

where ΔN_1, ΔN_2, are 3x1 Gaussian random vectors. Then, we can calculate the Brownian translational displacement as

$$\begin{bmatrix}\Delta X_B \\ \Delta Y_B \\ \Delta Z_B\end{bmatrix} = \Delta r_B + k_BT \begin{bmatrix} 0 \\ 0 \\ \frac{\delta}{\delta z} M_{3,3}\end{bmatrix} \Delta t$$

Similarly, if we have a vector $p(t)$, we can calculate its new orientation after a Brownian rotational diffusion step as,

$$p(t+\Delta t) = p(t) + \Delta\Theta_B \times p(t) + 0.5\Delta\Theta_B \cdot [p(t)\Delta\Theta_B - \Delta\Theta_B p(t)]$$

Then, by calculating the new orientation of three orthogonal unit vectors, we can compute an overall rotation matrix which can be used to update any point on the particle to its new location.

4.7.1.2 Deterministic Body Forces

The force and torque on the particle resulting from the shear flow are calculated following the methods of Goldman, Cox and Brenner (22, 23). Specifically,

$$F_{Shear} = 6\pi\mu a(a+h)\,\gamma F_s$$
$$\tau_{Shear} = 4\pi\mu a^3 \gamma T_s$$

where F_s and T_s are functions of the particle radius and distance from the wall, interpolated from Goldman, Cox and Brenner (22, 23).

To determine the steric repulsion force resulting from the DNA present in the system, a method from (130) was adopted. First, the DNA on the glass surface was modeled as gaussian random walks, consisting of 5 steps of 5 nm each. From these

walks, the height probability distribution function, $p(h)$, of the DNA strands was inferred. Then, the loss of entropic energy between these two planar surfaces per DNA is

$$dU_{Planar}(h) = k_b T * p(h) \int_0^h p(h)dh$$

Then, by using the Derjaguin approximation for a sphere and a plate we get the steric repulsive force:

$$F_Z^{Steric}(h) = 2\pi a\ (\rho_G^{DNA} + \rho_P^{DNA}) \int_h^\infty dU_{Planar}(h)dh$$

To estimate the Van der Waals attraction between our particle and the glass surface, we used the method described by Johnson (97) and Prieve (96). Specifically,

$$F_Z^{VDW} = k_b T A \left(\frac{a}{6h(1 + 14h/\lambda)}\right)\left(\frac{1}{h} + \frac{14/\lambda}{1 + 14h/\lambda}\right)$$

where, A is the Hamaker constant between a particle and glass surface separated by an aqueous fluid, and λ is the characteristic wavelength of retardation. However, in our analysis, we found that the for low values of A, Van der Waals did not appreciably affect the simulation, however, once A was increased to high, unphysical results were obtained. Therefore, in the final simulation, Van der Waals forces were not included.

The buoyant force on the particle is given by

$$F_g = 4/3\pi a^3(\rho_P - \rho_f)$$

4.7.1.3 DNA Modeling

To initialize the DNA strands in the model, first the number of DNA strands was determined, $N_{DNA} = 4\pi a^2 \rho_P^{DNA}$. Then, N_{DNA} 3 x 1 Gaussian random vectors were drawn and normalized to the particle radius; this determined the anchor point on the particle. Then to determine the "sticky-end" location, a Gaussian random walk was performed for each DNA strand starting at the anchor point on the particle, and consisting of 5 steps of 5 nm each, corresponding to single stranded DNA having a Kuhn length of 5 nm (134), a contour length of 0.63 nm/base pair (134), and our DNA having 40 base pairs. If the random walk intersected either the particle or the wall at any step, the walk was restarted. If, because the particle was too close to the wall, the walk failed more than 100 times, the sticky end was placed at a uniform random distance between the anchor site on the particle and the wall, and a predetermined Gaussian random radius away from the anchor site. This walk was then repeated every 100 time steps in the simulation, when the DNA strand de-hybridized, or when the particle motion would put the DNA sticky-end through the wall.

For the DNA binding kinetics, we use the DNA height distribution from the steric repulsion calculation, $p(h)$, to determine the concentration profile of DNA on the wall, $C(h)$. Then for each unhybridized DNA strand that is on the particle, based on where its "sticky-end" is we can calculate its rate of hybridization.

$$k_f^i = k_f C(h)$$

For the DNA dehybridization, we first calculate the unforced dehybridization rate as,

$$k_b = k_f \; exp(\Delta G/(RT))$$

We then model the force-induced unbinding of the hybridized DNA using Bell's model (4),

$$k_b^i = k_b exp(|F_{DNA}^i|RC/(k_B T))$$

where $|F_{DNA}^i|$ is the force from the DNA extension calculated using the worm-like chain model (136, 137),

$$|F_{DNA}^i| = 2k_B T/l_k \left[\frac{0.25}{\left(1 - \frac{l_{E2E}}{l_{con}}\right)^2} - 0.25 + \frac{l_{E2E}}{l_{con}} - 0.8\left(\frac{l_{E2E}}{l_{con}}\right)^{2.15} \right]$$

where l_K, l_{E2E}, and l_{con} are the Kuhn, end-to-end, and contour length of the DNA strand, respectively.

With each strand's respective rate of binding or unbinding, we can then determine the probability that a DNA event occurs in a time step. Specifically,

$$k_{total} = \sum_{Bound} k_b^i + \sum_{Unbound} k_f^i$$

$$p_{yes}(\Delta t) = 1 - \exp(-\Delta t k_{total})$$

We can then draw a random uniform number, between 0 and 1, to determine if an event happens, and if one does, we can determine at what time point by drawing a new random uniform number p, between 0 and 1, and then calculating

$$\Delta t = -ln(1 - p)/k_{Total}$$

Finally, we can determine which DNA event occurred in the time step by taking the sequence of the cumulative sum of the k^i's, i.e. $\{0, k_{f,b}^1, k_{f,b}^1 + k_{f,b}^2, \ldots, k_{total}\}$, drawing a random number between 0 and k_{total}, and then finding where in the sequence that random number falls.

If a DNA hybridization event is chosen, a random anchor point on the wall is selected based on an a priori determined radial distribution.

4.7.1.4 Overall Model Procedure

Initialize particle and DNA parameters

Compute mobility matrix M, based on particle distance from the wall

Compute the total force and torque on exerted on the particle,

$$F = F_{Shear} + F_{VDW} + F_g + F_{Steric} + \sum_{Bound\ DNA} F_{DNA}^i$$

$$\tau = \tau_{Shear} + \sum_{Bound\ DNA} \tau_{DNA}^i$$

Determine the velocity of the particle, using equation [**], and determine Δt based on maximum allowable displacement.

Determine DNA binding and Unbinding rates and do lottery to determine if any DNA events occur. If a DNA event occurs, update DNA list and Δt.

Calculate the deterministic and Brownian displacements using the new Δt.

Update particle and DNA locations. If any DNA strands are longer than their contour length, automatically break these bonds. If the particle travels either through the wall or further than 50 nm above the wall, reflect the particle back into the simulation domain.

Repeat steps 2-7 until the final time is reached.

Chapter 5 Adhesive Dynamics Validation

5.1 Introduction

In Chapter 4 an adhesive dynamics simulation was used to model DNA functionalized particles rolling along a wall in a shear flow. The model consisted of a particle coated in explicitly represented DNA strands near a wall with DNA strands represented by a concentration field. The hydrodynamic forces and mobility matrix of the particle were calculated using the solutions for the viscous flow of a particle near an infinite wall (21-23, 133) . Using this mobility matrix, the Brownian motion of the particle was determined following the solution to the Langevin equation (24). The model included gravity, Van der Waals forces, and steric forces originating from the DNA on the particle and the wall. Additionally, the forming and breaking of DNA bridges was modeled using Bells model (4, 7). Once formed, these bridges exerted forces and torques on the particle following the worm-like-chain model, and this force accelerated the breaking of DNA bridges.

This chapter presents some of the features of the model and the methods used to validate it. We present the hydrodynamic solutions for our particle. We then discuss the effects of gravity, Van der Waals, and the steric repulsion, and find that the diffusing particle follows the Boltzmann distribution in this energy potential. Then, we discuss the handling of DNA bridges.

5.2 Hydrodynamics of a Particle in a Shear Flow

The hydrodynamic forces and mobility matrix of the particle were calculated using the solutions for the viscous flow of a particle near an infinite wall (21-23, 133) . Since we neglect inertia in this system (Re<<1), these solutions result in a 6x6 mobility matrix relating the force and torques on the particle to the translational and rotational velocities. This mobility matrix accounts for the friction between the wall and the particle, i.e. when the particle is closer to the wall it takes more force to move it at the same velocity. Additionally, it couples the forces and torques on the particle, meaning that when a force is applied in the X-direction, it causes the particle to translate in that direction AND rotate about the Y-axis of the particle. For this model we use the coordinate system where X is the direction parallel to the wall, and the shear flow is in this direction. Y is the direction parallel to the wall and orthogonal to the shear flow and Z is the direction orthogonal to the wall.

Figure 5.1 and Figure 5.2 show the dimensionless shear force and torque on the particle and the resulting dimensionless rotational and translational velocity. In both cases, at large gap distances between the particle and the wall, the effect of the wall friction has a vanishing effect and the particle behaves as if there was no wall. As the particle approaches the wall, friction becomes a bigger factor, and the particle's velocity becomes significantly reduced. Within the simulation, we predominantly explored the regime where the gap height was between 1 and 50 nanometers and $10^{-3}<(Z-a)/a<10^{-2}$.

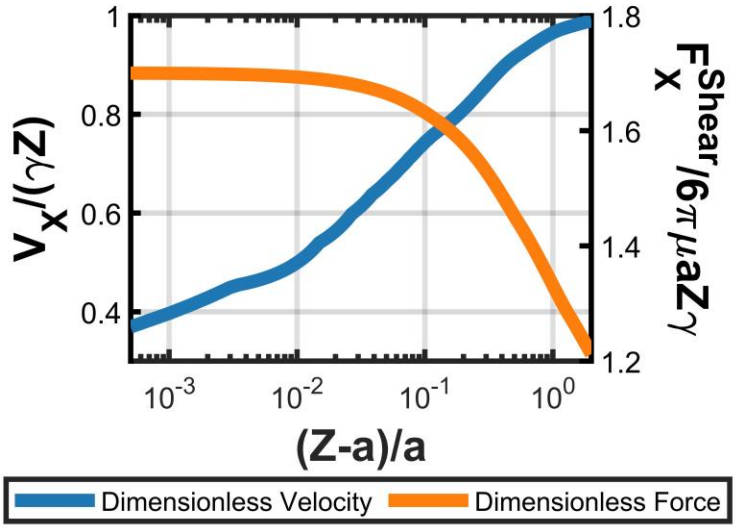

Figure 5.1 Solution for the velocity and shear force of a spherical particle of radius *a* in a shear flow near a wall. Z is the height of the center of the particle. The blue curve shows the velocity of the particle divided by its velocity if there was no friction from the wall. The orange curve shows the shear force on the particle divided by the force if there was no friction.

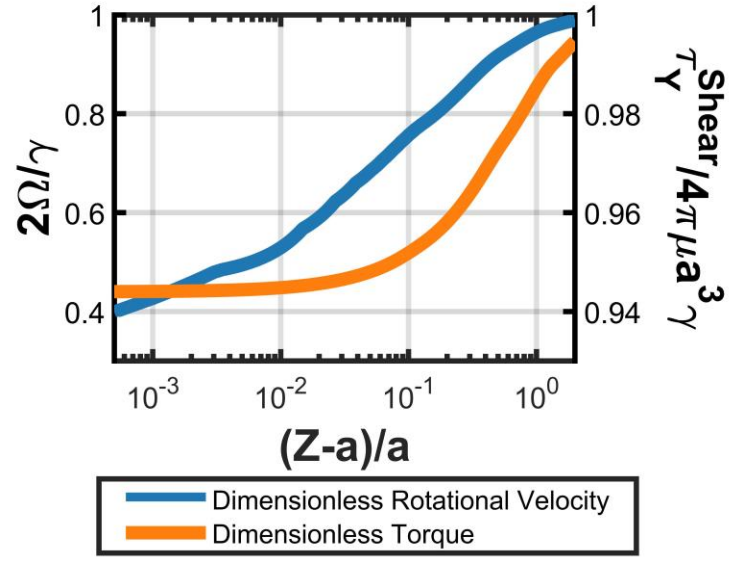

Figure 5.2 Solution for the rotational velocity and shear torque of a spherical particle of radius *a* in a shear flow near a wall. Z is the height of the center of the particle. The blue curve shows the rotational velocity of the particle divided by its rotational velocity if there was no friction from the wall. The orange curve shows the shear torque on the particle divided by the torque if there was no friction.

Using the mobility matrix and the solution to the Langevin equation (24), the translational and rotational diffusivity of the particle can be calculated. Figure 5.3 and Figure 5.4 show the dimensionless translational and rotational diffusivity of the particle as a function of the gap height. It should be noted that these solutions agree with the solutions for the translational diffusivity of a particle near a wall (21, 138) , specifically for the diffusivity of a particle near the wall parallel to the wall,

$$\frac{D_{\parallel}}{D^{\infty}} = 1 - \frac{9}{16}\left(\frac{a}{Z}\right) + \frac{1}{8}\left(\frac{a}{Z}\right)^3 - \frac{45}{256}\left(\frac{a}{Z}\right)^4 - \frac{1}{16}\left(\frac{a}{Z}\right)^5$$

and diffusion normal to the wall,

$$\frac{D_{\perp}}{D^{\infty}} = \frac{6(Z-a)^2 + 2a(Z-a)}{6(Z-a)^2 + 9a(Z-a) + 2a^2}$$

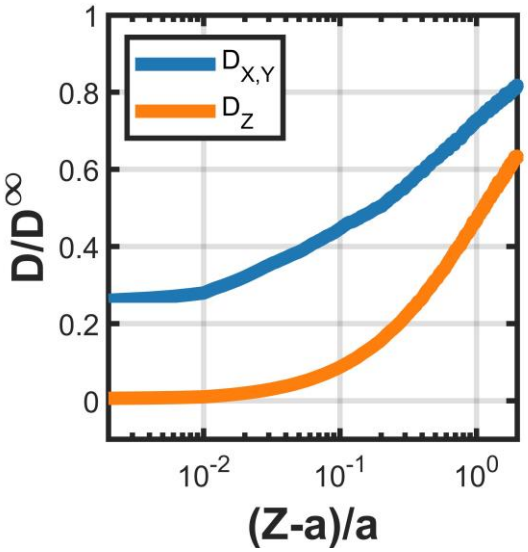

Figure 5.3 Dimensionless translational diffusivity in the X,Y, and Z direction of a particle near a wall of radius *a* and center height *Z*. Here, D^{ω} is the Einstein-Stokes diffusivity of the particle.

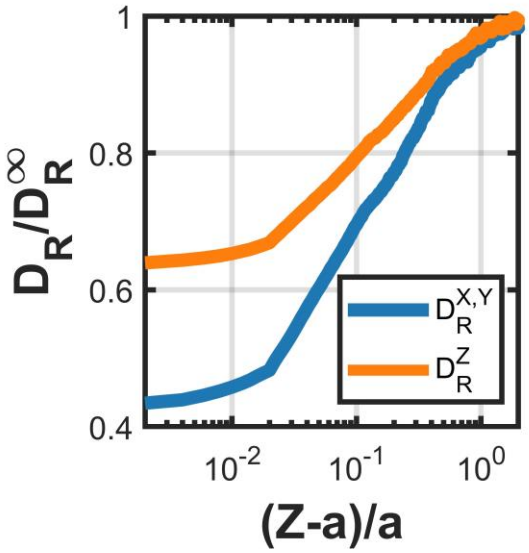

Figure 5.4 Dimensionless rotational diffusivity about the X,Y, and Z axis of a particle near a wall of radius *a* and center height *Z*. Here, D^{ω}_{R} is the Einstein-Stokes rotational diffusivity of the particle.

5.3 Effect of Van der Waals and DNA Repulsion on a particle

To determine the DNA concentration field of the DNA on the wall, the DNA strands were modeled as 3 dimensional gaussian random walks, where each step was a Kuhn length. For this process to be valid, it is important that if at any point during the walk the DNA intersects the surface, we restart the walk. If we ignored this consideration, the height distribution of the DNA would be a half gaussian originating at the origin. Figure 5.5 shows the resulting height distribution of the DNA strands for a strand with a contour length of 19 nanometers and a Kuhn length of 5 nanometers. The concentration field is proportional to this distribution, and the steric force resulting from the DNA can be computed using the method outlined by Ben Rogers (130).

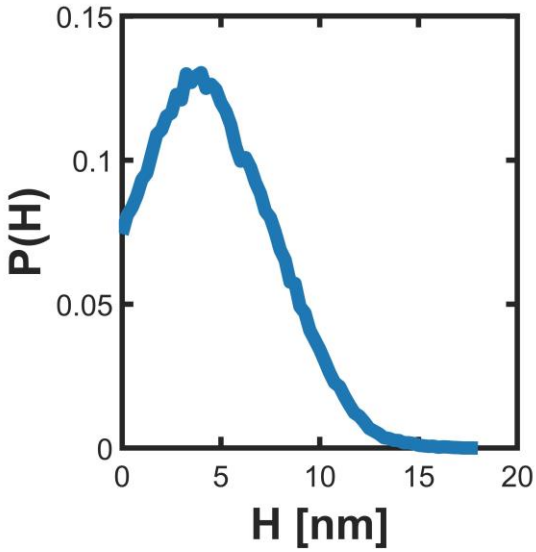

Figure 5.5 Height Distribution of DNA on the glass, assuming contour length of 19 nanometers, corresponding to 30 base pairs and a Kuhn length of 5 nanometers.

The retarded Van der Waals forces can be calculated using the equations of Bevan and Assemi (96, 139). The gravitational force is simply the buoyant force felt by the particle in the fluid. These forces are shown in Figure 5.6. By integrating this force, the potential can be found as shown in Figure 5.7.

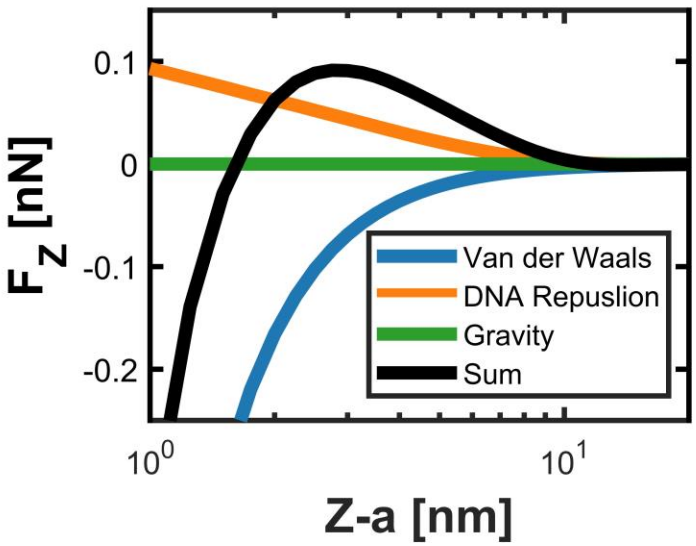

Figure 5.6 Force in the Z direction exerted on a particle with radius of 500 nanometers from the Van der Waals, DNA steric repulsion, and gravitational forces, where *Z-a* is the gap distance between the wall and the particle surface. The DNA density was assumed to be 3000 strands per μm^2, and the DNA contour length was 19 nanometers.

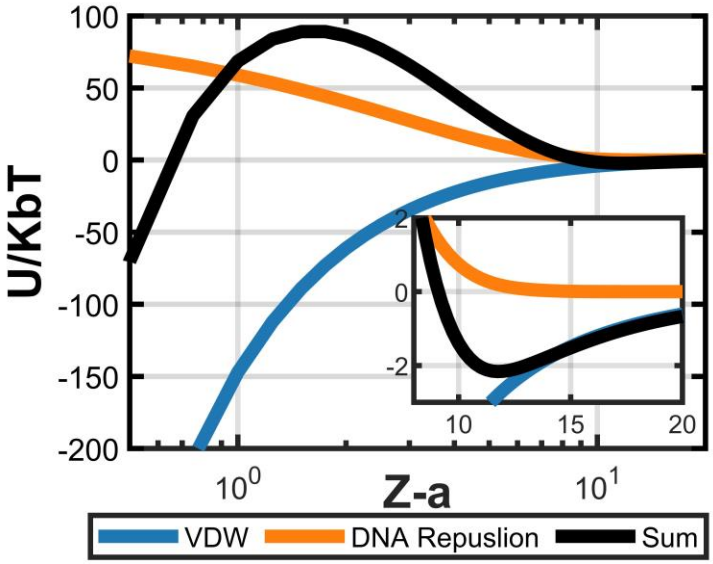

Figure 5.7 Energy potential in the Z direction felt by a particle with radius of 500 nanometers from Van der Waals and DNA steric repulsion, where *Z-a* is the gap distance between the wall and the particle surface. The DNA density was assumed to be 3000 strands per μm^2, and the DNA contour length was 19 nanometers.

To ensure that the model was functioning properly, a simulation was run where DNA bridges were turned off, but the particle could still diffuse, and the deterministic

forces were still exerted on the particle. Then, the height distribution of the particle was analyzed, as shown in Figure 5.8. When no external forces were exerted on the particle, the particle was equally likely to be at any height, satisfying the fluctuation-dissipation theorem. Additionally, when forces were exerted on the particle, effectively making the particle diffuse within an energy potential, the particle's height distribution satisfied the Boltzmann distribution, $P(h_1)/P(h_2)=exp(-(U_1-U_2))$.

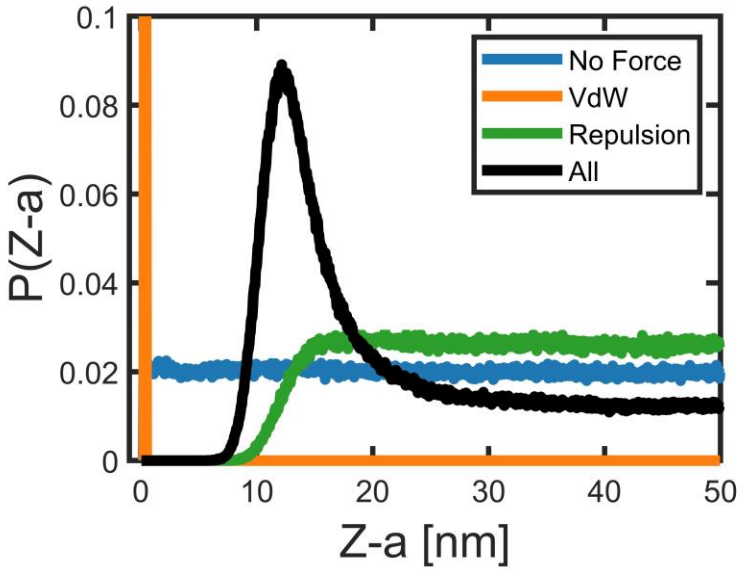

Figure 5.8 Height distribution of a diffusing particle with radius of 500 nanometers near a wall with the Van der Waals forces and DNA steric repulsive forces exerted on the particle. Here the DNA density was assumed to be 11000 strands per μm^2. It was confirmed that these distributions follow the Boltzmann distribution from the energy potential.

5.4 DNA Anchor Point Determination

In the model, prior to bridge formation, the DNA on the wall is represented as a concentration field. However, when a bridge is formed, an explicit DNA strand is necessary to determine the total end-to-end distance and thus the force on the particle

exerted by this bridge. The anchor point of this DNA is determined using a gaussian distribution for the radial distance between the DNA on the particle's sticky end and the DNA strand on the wall's anchor point, and a uniform distribution for the direction. To determine the parameters of the gaussian distribution, random gaussian walks were computed starting at the wall. These walks were then binned by the final height of the walk, and the mean and standard deviation of the radial displacements were computed, as shown in Figure 5.9. Unsurprisingly, it was found that the mean and standard deviation of the radial displacement of the walk was correlated to the final height (if a walk reached a height comparable to its contour length, it must have gone straight up), and these were each empirically fit to $\langle R \rangle = a + b * \ln(L_C - H)$ and $\text{std}(R) = a + b * \ln(L_C - H)$.

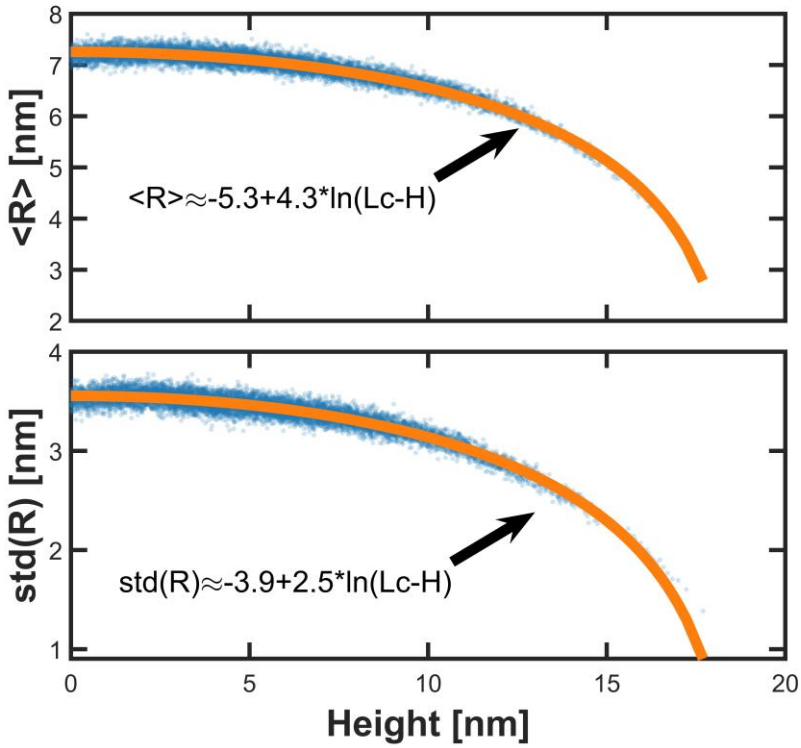

Figure 5.9 Empirical model for determining the distribution of anchor point locations on the glass surface once a DNA bond is formed. In the program, once a DNA strand on the particle is determined to bind to the surface, the location of its sticky end is taken. Then, based on the height of the sticky end, the radial off set of the anchor point from the sticky end, R, is taken from a Gaussian distribution with a mean and standard deviation dependent on the height. The mean and standard deviation of this distribution was determined by doing 1e7 random gaussian walks for DNA with a contour length (Lc) of 19 nm (30 base pairs) anchored at a wall. Then, binning this data based on the height from the surface we determine the mean and standard deviation of the radial offset. Empirically, the data fits the form std(R), <R>=a+b*ln(Lc-H).

5.5 Force Response of DNA tethers

Once a DNA bridge is formed, we use the worm-like chain model to determine the force and torque exerted by this bridge. Figure 5.10 shows the force extension curve of the worm-like chain model assuming a Kuhn length of 5 nanometers. At small extensions, the model behaves like a spring, with the force being proportional to the

length of the extension. However, when the chain is extended to ~70% of the contour length, the force deviates from the spring model and asymptotes towards infinity.

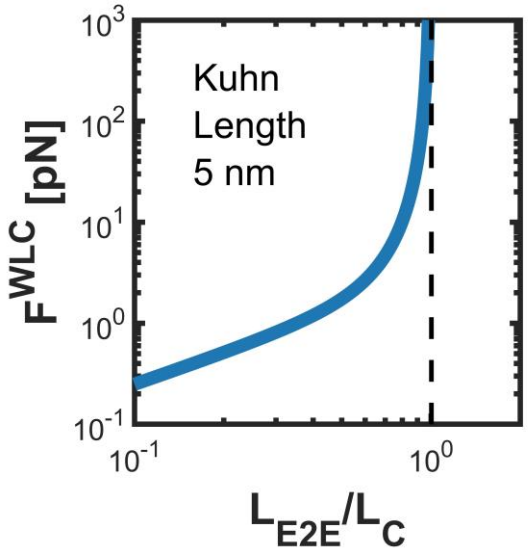

Figure 5.10 Force extension curve for a DNA strand modeled by the Worm-Like Chain model.

We model the force accelerated unbind rate of the DNA strands using Bells model (4) where $k_d = k_d^O \exp\left(\frac{F*RC}{k_bT}\right)$, where k_d^O is the unforced unbinding rate determined by the forward binding rate of reaction and the Gibb's free energy of hybridization, F is the force exerted by the DNA strand, *RC* is the reactive compliance of the DNA, effectively the distance between the bound state and the transition state, and k_bT is the Boltzmann constant times the temperature. The resulting unbinding rate as a function of the end-to-end distance of the DNA strand is shown Figure 5.11 and Figure 5.12 for different values of the Gibb's free energy of hybridization and reactive compliance, respectively.

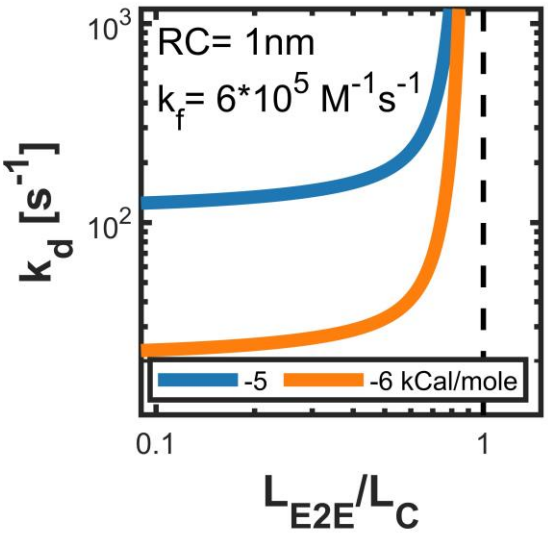

Figure 5.11 Dehybridization rate of DNA strand modeled as a Worm-Like Chain using the Bell Model. The legend shows the Gibb's Free energy of hybridization, and the annotation shows the reactive compliance and forward rate constant of hybridization.

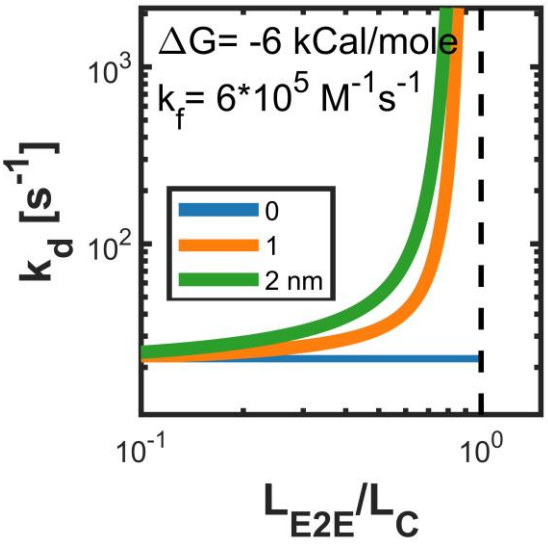

Figure 5.12 Dehybridization rate of DNA strand modeled as a Worm-Like Chain using the Bell Model. The legend shows the reactive compliance, and the annotation shows the Gibb's free energy of hybridization and forward rate constant of hybridization.

5.6 Conclusions

In this section we presented some of the basic features of the adhesive dynamics model for a DNA functionalized particle in a shear flow near a wall. Specifically, we showed the dependence of the hydrodynamic forces and torques, translational and rotational velocities and diffusivities on the distance between the particle and the wall. We then showed the forces and energy potential resulting from gravity, Van der Waals forces, and the steric repulsive forces. Using these potentials, we verified that the Brownian particle satisfies detailed balance. We then showed how the anchor point of the DNA bridge on the wall was determined, and the resulting force exerted on the particle and unbinding rates of the DNA bridges.

Chapter 6 DNA Functionalized Surfaces

6.1 Adsorption of Polystyrene-Poly (Ethylene Oxide)-DNA onto Polystyrene Colloids

6.1.1 Introduction

DNA coated colloids have been used in a variety of applications ranging from self-assembly (140-142), to the study of DNA kinetics and colloidal interactions (35, 130) and much of the work in this dissertation. A main approach of functionalizing colloidal particles with DNA is to use the swell-deswell method (116, 143). In this method, the DNA is first covalently linked to a di-block or tri-block copolymer, where one block is miscible with the polymer particle and the other block is miscible in aqueous solutions. Then, the particles and DNA-polymer are mixed, and a solvent is added that swells the particles allowing the polymer to adsorb onto and anchor itself to the particle. Then the solvent is removed and the particles deswell, trapping the polymer in the particle. This then creates a brush of DNA on the surface of the particle and, with the typical polymers used, has the added benefit of creating a high-density poly (ethylene oxide) brush layer on the particle further stabilizing the particles from aggregation. While these processes have been used successfully to create DNA functionalized particles for a wide array of applications, this process has not been investigated thoroughly to understand the process parameters that control the resulting DNA density on the particle.

In this section, we perform the swell-deswell procedure using polystyrene-poly (ethylene oxide)-DNA to graft DNA onto the surface of polystyrene particles. We investigate the effect of the DNA concentration, salt concentration, and incubation time on the final DNA density on the particles. Additionally, we propose a potential mechanism derived from a two-stage random sequential adsorption process to model the kinetics of this process.

6.1.2 Method for Adsorbing PS-PEO-DNA onto Particles and Measuring DNA Yield

The click chemistry protocol previously described was used with a final DNA concentration of 125 µM and 375 µM PS-PEO, and 150 mM NaCl. A solution of 1 mM PS-PEO solution in bio water was made. Then, 50 µL of 1.02 µm at 10% volume/volume carboxylate particles were washed in 1x Tris EDTA 3 times. The particles where mixed with the "Clicked" DNA, PS-PEO solution, 200 mM NaCl 1xTE, and 1xTE so that the resulting solution had 600,000 PS-PEO polymer strands per particle, and the desired amount of DNA and NaCl concentration. Then, 5 µL of toluene was added to the solution, and the solution was gently inverted for the duration of the incubation time. After incubation, the solution was put into a 90 °C oven to remove the toluene, and then again washed in 1xTE 3 times.

Then, the particles were mixed with a complementary fluorescently tagged DNA strand, in 300 mM NaCl and allowed to hybridize for ~10 minutes. The particles were

pelleted, and the supernatant removed. The supernatant was then centrifuged to pellet any residual particles and then measured using UV/Vis to measure the adsorption of the fluorophore's excitation peak. This was compared to standards of known DNA concentrations to determine the amount of still soluble DNA, and subtracting this number from what was originally added, the amount of DNA labeled to each particle was calculated.

6.1.3 Results and Discussion

Overall, three operating parameters of the procedure were investigated at a range of values: the DNA concentration (20,000, 100,000 and 200,000 DNA/Particle added), NaCl concentration (10, 30, 100, and 300 mM) and incubation time (3 and 40 hours). The results of these experiments are shown in Table 2.1 and Figure 6.1.

Increasing the amount of DNA added per particle increases the total amount of DNA labeled to the particles, however, at the shorter incubation times, this relationship is sublinear, i.e. doubling the amount of DNA added results in less than a doubling of the DNA on the particle. This makes sense intuitively, as at some point we would expect to saturate the particle surface to a point where no more DNA strands can be squeezed in. However, at the longer incubation time of 40 hours, there does appear to be a linear relationship between the amount of DNA added and the DNA yield on the particle.

Increasing the NaCl concentration during the incubation results in an increase in the DNA density on the particles. We suspect this is because the DNA molecules have a

negative charge, so as we add more DNA strands to the particle, there is an increasing electric potential hindering further adsorption. However, by increasing the salt concentration, and thus decreasing the Debye length, more DNA strands can be added before this electric force hinders further adsorption.

Table 6.1 Results of Adsorbing DNA onto 1.02 micron particles for a range of swelling conditions

[NaCl] (mM)	Incubation Time (hours)	DNA/Particle Added	DNA/Particle Final	Efficiency
10	3	20000	1157	6%
10	3	20000	1590	8%
10	3	100000	3156	3%
10	3	100000	3979	4%
10	3	200000	5330	3%
10	40	20000	990	5%
10	40	100000	5720	6%
10	40	200000	13170	7%
30	3	20000	2115	11%
30	3	100000	3971	4%
30	40	20000	2039	10%
30	40	100000	6139	6%
30	40	200000	14554	7%
100	3	20000	2071	10%
100	3	100000	5698	6%
100	40	20000	2138	11%
100	40	100000	8339	8%
100	40	200000	17939	9%

300	3	20000	2650	13%
300	3	100000	5942	6%
300	40	20000	2914	15%
300	40	100000	10420	10%
300	40	200000	20702	10%

With these results, we attempted to model the kinetics of the system. Initially, we tried to model the system using a standard random sequential adsorption process, however this was not successful. We then developed a new model which we will call a two-stage random sequential adsorption process. In this process, there is an initial fast adsorption process, and then a longer and slower “ripening” process. This initial fast adsorption process occurs at the beginning when the DNA on the particle is sparse, so that an incoming DNA strand is unlikely to encounter an already bound strand. We can calculate the radius of gyration of the PEO-DNA component of the strand. Using this radius of gyration, we can estimate the diffusivity and expected areal density on the particle. Using these values along with the solution concentration, we can calculate the characteristic time to saturate the particle in this fast process, finding that it is about ~0.1 seconds. So, this initial process sets the y-intercept in the graphs below. This first stage packs the particle to the density allowed by the size of the radius of gyration of the DNA strand. The second stage accounts for the fact that there are fluctuations in the DNA strands configuration (such as pointing outward instead of laying on the surface of the particle) that may allow for a new DNA strand to insert onto the particle. This process is much slower as there is an electrostatic force the new DNA must overcome to

insert, but in theory we might expect this process to occur until the steric limit is reached. Overall this model is described by the differential equation

$$\frac{d\Theta}{dt} = (C_O * Yield - \Theta) * [k_1 * (M_1 - \Theta) + k_2 * (M_2 - \Theta)]$$

, where Θ is the number of DNA on the particle, C_O is the amount of DNA per particle added initially, *Yield*, is fraction of DNA strands that are labeled to a PS-PEO strand, $M_{I,}$ is the maximum amount of DNA allowed per particle for the first and second stage of RSA, respectively, and k_i, is the rate constant of the respective stages. Additionally, since the screening length scales with the inverse of the square root of the ionic strength, the initial stage of RSA should have a maximum coverage proportional to the ionic strength, i.e. M_i=a*[NaCl]+b. Additionally, since the second stage considers when the DNA strands are overcoming this electrostatic potential to insert onto the particle, we expect k_2 to be a function of ionic strength. With this we fit the data to the model using a least-squares fitting approach. The results are shown in Figure 6.1 and Table 6.2.

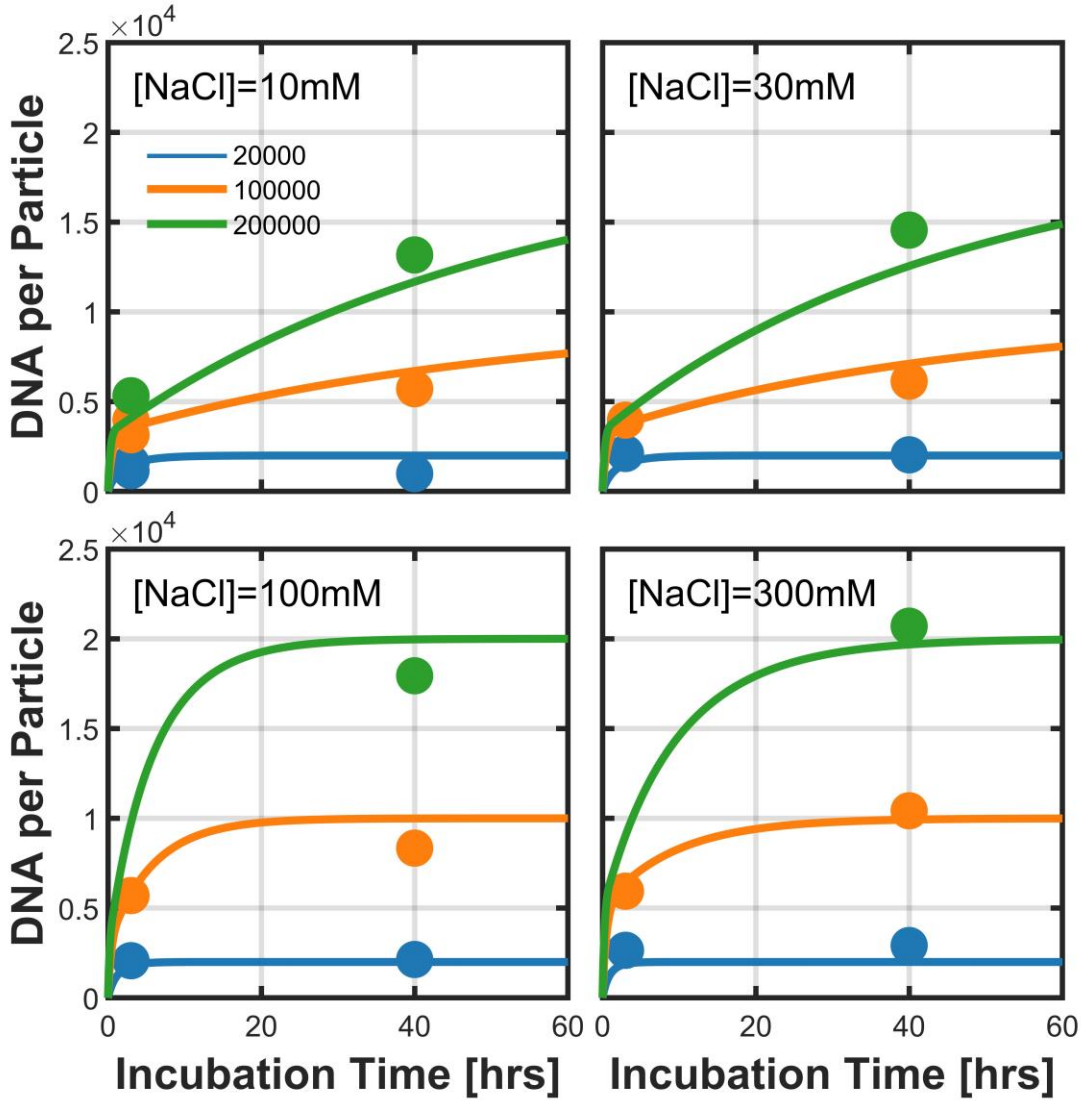

Figure 6.1 Results of adsorbing PS-PEO-DNA onto polystyrene particles. Curves show a fit of the two stage RSA model. The legend shows the initial DNA to particle stoichiometry during the adsorption

Table 6.2 Two-Stage RSA Fitting Parameters. M1 and M2 are in units of DNA/Particle and K1 and K2 are in units of Particle/DNA-s

NaCl [mM]	d	Yield	K1	M1	K2	M2
10		10%	4.73E-08	3561	5.3E-11	99712
30				3750	6.1E-11	

	441	5.2E
100	0	-10
	629	3.2E
300	6	-10

Overall, the model does fit the data well and captures the expected trends. For instance, we see that in the first stage of the adsorption, the maximum allowable DNA density increases with salt as expected. Similarly, the rate constant in the second stage of the adsorption increase with salt. However, to fully validate this model, more data points would be required. Additionally, this model and the characteristic time of diffusion of DNA suggests that this first stage of the adsorption occurs extremely rapidly, so to probe this regime more thoroughly, it is likely that diluting the system by several orders of magnitude is necessary.

6.1.4 Conclusion

We have investigated the swelling process for adsorbing polystyrene-poly (ethylene oxide)- DNA polymers onto polystyrene microspheres. We looked at the effect of the incubation concentration of the DNA polymer, the salt concentration during incubation and the incubation time. We found that increasing the DNA concentration leads to an increase in the overall adsorption on the particles, however this increase is not necessarily linear, owing to the crowding of the surface. Increasing the ionic strength of the solution can mitigate some of this crowding effect leading to a higher overall DNA density on the particle, a result of the decreased electro-steric size of the DNA strands. This data could not be modeled using a random sequential adsorption

process, however, we were able to model this process using a two-stage random sequential adsorption process, the first stage whereby the DNA rapidly adsorbs onto the particle up to the density allowed by its radius of gyration. The second stage then packs the particle surface further with DNA at a much slower rate. Overall though, more experiments, and better time resolution would be necessary to further validate this model.

6.2 DNA Functionalized Gold Nanoparticles

6.2.1 Introduction

Nanomaterials and nanostructured materials composed of inorganic nanoparticles are an exciting area of research for their emergent properties different from the nanoparticles individual and the bulk materials properties (144), particularly with respect to their interactions with light. These materials hold promise in applications in electronics, photonics and medicine (145). There are two general approaches for creating these materials; top-down nanofabrication techniques, and bottom-up self-assembly. The Mirkin lab in particular invented a DNA based method for the self-assembly of gold nanoparticles (146-148). In their process, they use citrate gold nanoparticles and then functionalize them with thiol modified DNA, and then by engineering the DNA sticky ends and nanoparticle size and shape appropriately, they can create a wide array of self-assembled structures. In this process, it is well known that a high DNA density on the particle (35, 149, 150) improves the kinetics of DNA

directed self-assembly of colloidal particles. The Mirkin group has investigated (151) the effect of some of the parameters in loading DNA onto gold nanoparticles, including salt, DNA spacer composition, and nanoparticle size, finding that these parameters can be used to tune the final DNA density on the particles.

This section provides an investigation of one method for producing DNA functionalized gold nanoparticles. We present the method used for creating citrate capped gold nanoparticles and the subsequent functionalization of these nanoparticles with DNA using the gold thiol reaction. During this functionalization, there are several process parameters which affect the final yield of the gold nanoparticle thiol modified DNA reaction: the relative stoichiometry of the reactants, the size of the DNA strand being attached, the ionic concentration and pH of the reaction solution, and the reaction time. We present the results of this functionalization for a range of these parameters and discuss potential explanations for their effect on the yield.

6.2.2 Method for Synthesizing Citrate-Capped Gold Nanoparticle Synthesis

The method to synthesize citrate-capped gold nanoparticles, diameter ~12 nanometers, using the citrate reduction method (152, 153), is adopted from literature (154). Briefly, first all glassware was cleaned with aqua regia (1:3 v/v nitric acid to hydrochloric acid) and rinsed thoroughly in deionized water. Then, 98.5 mg (250 µmoles) of gold (III) chloride trihydrate was dissolved in 250 mL of deionized water in a 1-liter round bottom flask. The flask was connected to a condenser through which cool

water was run, allowing for full reflux, and then preheated using a 100 °C silicone oil bath, using a stir bar to constantly mix the contents of the flask. 279 mg (950 µmoles) of sodium citrate tribasic dihydrate was dissolved in 25 mL of deionized water and quickly added to the flask. The solution underwent a color change from clear to a deep red wine color. After the color change, the reaction was continued for 15 minutes before the oil bath was removed to stop heating, and the solution was cooled slowly to room temperature. The solution was then filtered using a 0.22 µm syringe filter (Millex® GP). The particles were then pelleted in a centrifuge at 13000 rpm for 20 minutes, the supernatant removed, and the particles redispersed in deionized water and again filtered, prior to storing at room temperature in an amber glass bottle. The concentration of the particles was measured using UV-Vis spectroscopy, assuming an extinction coefficient of the particles of ~ 2.01×10^{-8} $M^{-1}cm^{-1}$ at wavelength 520 nm. Note that if at any point during the procedure, the particles turned black and fell out of solution, this was a result of particle aggregation, likely from salt or other contaminants entering the system.

6.2.3 Method for Functionalizing Gold Nanoparticle with Thiol Modified DNA

The method for covalently linking thiol modified single stranded DNA to citrate capped gold nanoparticles was adopted from (154). While the operating parameters of the functionalization where changed during these experiments the general procedure is

as follows. First, a 1000 µL, 21 nM solution of the gold nanoparticles in deionized water was made. Then, 8.5µL of 1000 µM thiol modified DNA (obtained from Integrated DNA Technologies) was added to the nanoparticle solution. Then, a 230 µL, 3 M NaCl solution and a 137 µL 10X phosphate buffer (pH=7.4) were made and combined. Then, the nanoparticle solution was mixed on a vortex and every the NaCl, phosphate buffer solution was added to the nanoparticle solution in 10 installments, with ten minutes between each addition. The final solution had a gold nanoparticle to DNA stoichiometry of 1:400, [NaCl] of 500 mM, and 1 x phosphate buffer concentration. The solution was then pelleted in a centrifuge as before, and the supernatant removed for analysis under UV/Vis to determine the amount of DNA adsorbed to the particles. The particles were resuspended in 0.3 M PBS.

Depending on the operating conditions analyzed, the stoichiometry of nanoparticles to DNA was varied from 1:110, 1:315, and 1:609. The final salt concentration was varied from 0, 10, 30, 100 and 300 mM. The use of the phosphate buffer or deionized water was used to control the incubation pH at 7.4 or 5.5, respectively. Additionally, it was also tested if allowing the solution to react overnight prior to washing had an effect. Finally, the size of the DNA strand was also investigated with a 6 and 26 base pair strand being used, as shown in Table 6.3. A summary of the reaction conditions is shown in Table 6.4.

Table 6.3 DNA design for gold nanoparticle experiments

DNA Strand Name	5’ Modification	Sequence	3’ Modification
PC Gold Short	5’-ThioMC6-D	CTGCAG	
PC Gold Long	5’-ThioMC6-D	20T-CTGCAG	

6.2.4 Results and Discussion

A summary of the DNA yield on gold nanoparticles for the various process parameters investigated is shown in Table 6.4 and Figure 6.2. In general, we find that adding more DNA to the incubation results in a higher DNA density on the particles, but this relationship is sublinear. Additionally, increasing the ionic concentration of the incubation solution results in higher DNA density on the particle. Using shorter strands of DNA also results in more DNA being able to bind to the particle. Allowing the reaction to go overnight also increases the yield somewhat, as does controlling the pH to be 7.4 as opposed to the pH of deionized water of 5.5 (from dissolved CO_2).

Table 6.4 Summary of DNA functionalization of gold nanoparticles process parameters and results

Strand	DNA Added/AuNP	[NaCl] [M]	pH	Rested	DNA/AuNP Result
PC Gold Long	110	0	5.5	No	0
		0.1		No	53
	315	0.3		No	79
				Yes	121
		1		No	116
				Yes	141
	315	0.3	5.5	No	171

PC Gold Short				Yes	177
		1		No	202
	609	1	5.5	No	250
				Yes	405
			7.4	No	289
				Yes	437

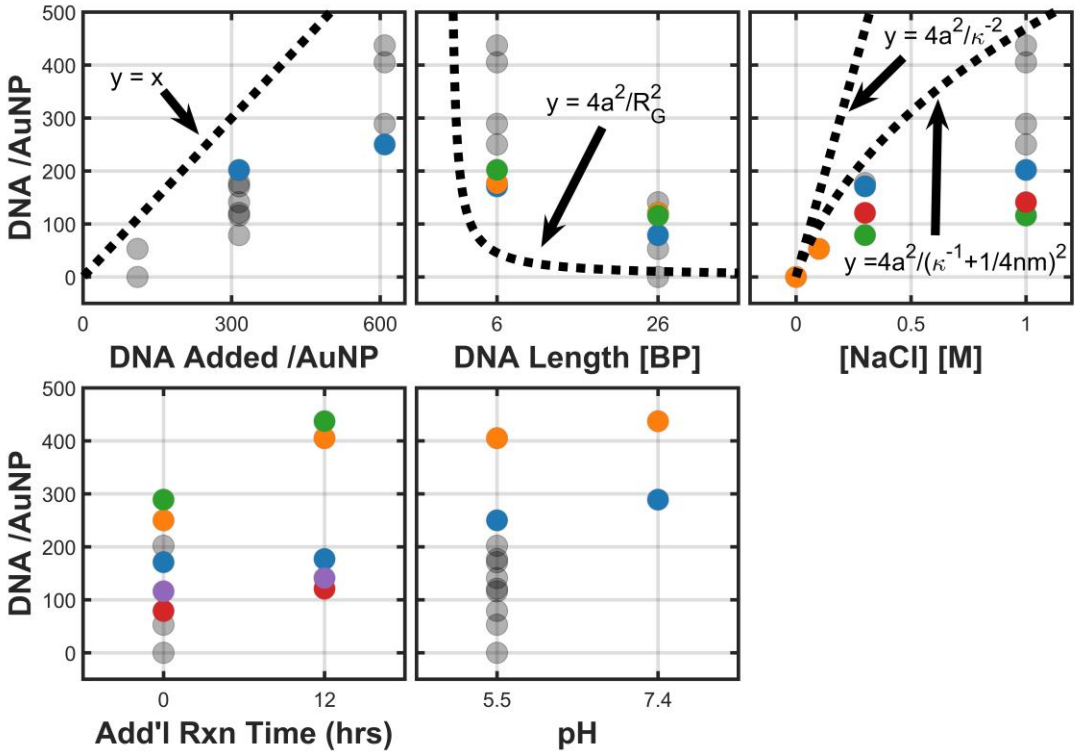

Figure 6.2 Summary of results from covalently bonding thiol modified DNA to gold nanoparticles. In each panel, the colored data points correspond to data points where the parameter shown in the X-axis is the only parameter changed between the data points of the same color. The grey data points show all the other experimental values. In the top left plot, the dashed line indicates the y=x line, where all the DNA added would end up on the particle. In the top center plot, the dashed line indicates the maximum DNA density on the gold nanoparticles if the DNA occupied a disk the size of its radius of gyration, i.e. the mushroom limit. Data points above this line are in the mushroom/brush regime. In the top right plot, the dashed line indicates the DNA density if each DNA strand occupied a disk the size of the Debye length at that particular ionic strength or the Debye length plus 250 Angstroms.

These results can be explained by considering the reaction mechanism of this process. The overall reaction is described by Au + HS-R $\rightleftharpoons$Au-S-R + H^+ (155). Using this overall reaction, it makes sense that adding more DNA to the reaction will result in more DNA on the particle, as will increasing the pH. When the DNA functionalized particles were exposed to a highly acidic solution (HCl), it was observed that they rapidly flocculated, suggesting that at low pH the DNA strands can dissociate from the particles.

Next, we consider this problem as a random parking process, where there are a finite number of "parking spaces" that the DNA can occupy on the surface of the particle. This helps to explain why using larger DNA strands, which will occupy a larger area on the particle, yields fewer DNA strands on the particle. However, this analogy only makes sense in the mushroom and the mushroom/brush limit. In the brush limit, where each DNA strand is sticking straight out, we would not expect the equilibrium DNA density to be affected by size, but this process would still be kinetically limited.

Initially, the surface of the gold nanoparticle is electrically stabilized by the negatively charged citrate caps and the DNA strands are also negatively charged. As the thiol-DNA strands bind to the surface they displace these citrate caps, and sterically stabilize the particle. These negative charges create an energy barrier

that the thiol-DNA must overcome to get close enough to the nanoparticle to react. This is the reason that the salt must be added incrementally in the process. Adding to much salt to rapidly causes the particles to flocculate before the DNA has a chance to bind to and stabilize the particle suspension. Additionally, if we reconsider the process as a parking problem, we might expect the effective exclusion size of a DNA strand to be dependent on the Debye length, since the DNA strands are negatively charged, helping explain why increasing the ionic strength of the solution increases the DNA yield on the particles.

6.3 DNA Functionalization of Glass

6.3.1 Introduction

DNA microarrays are a technology born in the 1990's and early 2000's as a means of determining the composition of genomes (127). In one generation of this technology, various DNA probes were "spotted" onto a glass slide in gridded array (156). Then a fluorescently tagged version of the DNA being analyzed could be introduced and it would preferentially bind to the array where there was complementary DNA. Then, the relative number of the various sequences could be measured and used to infer properties of the genomic sequence. This method of gene expression profiling has a number of limitations, such as its ability to only detect sequences it was designed for, it is an indirect measure of the relative concentration of genes in a sequence which can be

convoluted by the relative kinetics and thermodynamics of DNA hybridization, and there is often a high degree of non-specificity in the binding (multiple genes may bind to the same “spot” or bind the substrate nonspecifically. For these reasons, microarrays have largely been replaced by direct sequencing techniques except in genotyping assays. However, in the development of this technology, a wide array of routes to functionalize glass with DNA were developed and employed (157). In developing the protocol for functionalizing glass with DNA used throughout this dissertation, we were inspired by and leaned heavily on these methods. In particular our goal was to create a system in which an optically transparent substrate could be covalently linked to a single stranded DNA in a high density, in such a way that it would prevent non-specific binding of our DNA functionalized microparticles, while still allowing for the DNA on the glass to bind to the DNA on our particles specifically. In this section, we discuss some of the attempted methods for this process and their shortcomings. We then discuss some of the findings in literature that point to the inherent limitations and difficulties of achieving these goals on glass. At the end, we discuss a potential solution for future studies that might help alleviate these limitations.

6.3.2 Methods for Covalently Linking DNA to Glass

In developing the protocol for functionalizing a glass surface with DNA, many different approaches were attempted, mainly based on the silanization of glass using (3-aminopropyl) triethoxysilane (APTES) and (3-mercaptopropyl) trimethoxysilane

(MPTMS). In evaluating these methods, a fluorescent strand of DNA was used to modify the glass, so that its presence could be detected under fluorescent microscopy. Additionally, complementary and noncomplementary DNA functionalized polystyrene particles were used to observe the relative amounts of specific binding of particles to the surface through DNA bridge formation, and nonspecific binding (Van der Waals, electrostatics, hydrophobic bonding, etc..). The pKa of the protonation of the primary amine group of the APTES is ~9.6 (158), while the pKa of the deprotonation of the thiol group of MPTMS is ~10.6 (159), meaning that the APTES modified glass is generally positively charged while the MPTMS glass is generally neutral or negatively charged.

The first attempts where to silanize the glass with either APTES or MPTMS and then deposit citrate capped gold nanoparticles onto the silanized glass, and then use the gold-thiol DNA reaction discussed in Section 6.2 to functionalize the surface with DNA. In the case of APTES glass, this procedure was able to create a film of DNA gold nanoparticles on the surface which held up to subsequent rinsing in DI water and methanol. However, this procedure led to copious non-specific binding of the DNA functionalized polystyrene particles, likely due to the electrostatic attraction of the positively charged APTES glass and the negatively charged DNA and carboxylate particles. In the case of the MPTMS modified glass, the gold nanoparticles were exposed to the glass in a low salt environment, no apparent deposition was observed, likely because of the electrostatic repulsion of the negatively charged particles to the negatively charged glass. When salt was added to the incubation solution, this did lead

to deposition of the particles onto the surface, however, this was accompanied by a high degree of particle flocculation (observed through a color change of the solution from pink to black). Since our goal was to create a smooth layer of particles on the surface with low non-specific binding of the polystyrene particles, this method was abandoned.

Another method we tried was to again use APTES glass and the 4-Nitrophenylchloroformate (4NPCF) chemistry from Chapter 2 In this approach, the glass was modified with APTES, leaving a primary amine residue on the glass which was then reacted with (4NPCF), leaving an acyl chloride residue. The acyl chloride would then be reacted with a hydroxyl terminated DNA. However, this approach had several issues. First, even when a large excess of 4NPCF was used, there was lots of nonspecific binding of the surface to the DNA colloids. Second, the yield of the hydroxy terminated DNA onto the glass was very low and did not promote specific binding of the DNA colloids. The low yield of DNA is likely due to the competition reaction of water to the acyl chloride group. This problem would persist even if the DNA-NPCF reaction was done first, as the DNA is solubilized in water. The high degree of non-specific binding was likely due to the incomplete reaction of the amine groups on the APTES, leaving the glass positively charged. This is supported by our groups yield of using aminated DNA to bind to 4NPCF activated Pluronic resulting in a ~5% efficiency on a DNA added per DNA achieved on particles basis.

The third method used again started with APTES modified glass. Then, using either glutaric anhydride or succinic anhydride to react with the amine group, leaving a terminal carboxylic acid. At this stage in the procedure, when tested, the glass had very little non-specific binding with the DNA functionalized microspheres. Then, through an esterification reaction with hydroxy modified DNA in the presence of a catalytic amount of sulfuric acid, the DNA should be covalently linked to the surface. While it was observed that DNA was deposited onto the surface, this DNA did not promote specific binding of the microspheres to the surface.

The scheme finally implemented for the studies in this dissertation (as described in Chapter 2 and Chapter 4 were developed by Rogers et al. (132). In this approach, the MPTMS functionalized glass is made and then exposed to disulfide modified DNA is added in either a carbonate or citrate buffered solution, allowing for a thiol/disulfide exchange reaction to take place, and the DNA being labeled to the glass. In this process, there was generally acceptably low levels of microsphere nonspecific binding if fresh MPTMS was used (it polymerizes with catalytic amounts of water, and using this polymerized version creates a very sticky surface for the particles and low DNA yield in the disulfide exchange reaction) and in general there was reasonable amounts of DNA on the surface to promote specific binding of the microspheres.

However, in our testing, it was found that only ~5-20% of the DNA bound to the glass surface was available for hybridization. This value was determined by using the

above process. Then using a microfluidic channel, exposing the DNA functionalized glass to a complementary fluorescent DNA probe in a salt solution. The DNA was allowed hybridize, and then the channel was rinsed with phosphate buffered saline, removing any non-adsorbed DNA. At this point it was found that the stoichiometry of the thiol DNA to soluble DNA probe stoichiometry was ~4:1. Then, the channel was rinsed in deionized water, which would dehybridize any DNA complexes and rinse away the unbound DNA. However, during this step, only ~1/3 of the DNA probe was removed. This suggests that ~1/12 of the DNA on the MPTMS surface was available for binding, and that the other ~11/12 of the DNA covalently linked to the glass and ~2/3 of the DNA probe were nonspecifically bound to the surface. Finally, exposing the microchannel to a high concentration of high molecular weight pluronic removed most of the DNA probe, suggesting hydrophobic interactions between the DNA and the glass.

6.3.3 Non-Specific Interaction of Glass

So why is such a high percentage of the DNA covalently linked to our glass not available for hybridization? And why do so many other techniques (157) report similar results of low availability of DNA on the surface? The answer may lie in DNA's propensity to bind nonspecifically to glass. In fact, one method of purifying DNA is to do chromatography of the DNA over silica surfaces (160, 161). A number of papers have experimentally investigated the effect of pH, buffer composition, and ionic strength (162-166) on the kinetics and thermodynamics of DNA adsorbing to the surface.

A particularly nice paper by Shi et al (51) used molecular dynamics simulations to investigate the binding mechanism of single stranded DNA to silica. In their study, they found that there were three separate pathways for this binding to occur. The first is through a phosphate silanol interaction. They found that this pathway has a free energy minimum of ~-20kJ/mol. The second pathway is through hydrophobic bonding. Due to natural statistical variations, the silica or glass surface is likely to have regions that are depleted of silanol groups. These regions tend to be hydrophobic, and thus promote hydrophobic stacking with the DNA base pairs. Additionally, they found that the base pairs bound to this hydrophobic region have a propensity to form hydrogen bonds with the adjacent silanol groups, further stabilizing this pathway of adsorption. The third pathway is through the hydrogen bonding of the deoxyribose sugar backbone to the silanol groups on the silica surface.

6.3.4 Conclusions

In retrospect, it appears that glass may have been poor substrate for attaching DNA to owing to its inherent proclivity for non-specific binding. However, glass is useful because there are a multitude of chemistries available for covalently linking ligands to it, techniques such as layer by layer deposition (167) and spin coating (168) to change the surface entirely, and it has good optical properties when an experiment calls for in-situ microscopy. In the future how might create a system which has a high density of DNA on the substrate surface with a high percentage of DNA available for binding and a low

degree of non-specific binding for DNA and particles alike? One potential method may be to replace the (3-mercaptopropyl) trimethoxysilane with a silane-PEG-thiol. These chemicals are commercially available for molecular weights of 400 to 20000 Daltons, corresponding to 2 to 450 PEG units, compared to MPTMS having only a three-carbon chain between the thiol and silane group. This replacement would have the benefit of effectively PEGylating the glass surface, providing a steric repulsion to prevent particles from adhering non-specifically. Additionally, if the PEG were in a sufficient density to approach the brush limit, it would also prevent the DNA covalently linked to the thiol group from being able to reach and subsequently bind to the glass surface.

Chapter 7 Directed assembly of particles using directional DNA interactions

This chapter is adapted from article: Porter CL, Crocker JC. Directed assembly of particles using directional DNA interactions. Current Opinion in Colloid and Interface Science. 2017;30:34-44. https://doi.org/10.1016/j.cocis.2017.04.005.

7.1 Abstract

The use of synthetic DNA to direct the spontaneous self-assembly of synthetic particles into surprisingly complex structures is a rapidly maturing field. Notable recent breakthroughs involve the use of DNA to realize well-controlled interactions between particles that are both chemically specific and directional in nature, the use of hierarchical self-assembly approaches, as well as computational studies to map out the broad palette of accessible structures and assemblies.

7.2 Introduction

Much of the excitement of the nanotechnology field is the idea of being able to spontaneously 'grow' useful nanostructured materials and devices from simple starting materials or building blocks. We dream of being able to grow a useful machine from a tiny seed and abundant materials and energy, like growing an oak from an acorn. Less ambitiously, we could imagine synthesizing molecular-scale computing equipment or memory elements and assembling them into a form we could interface with and use

without billion dollar nanolithography fabrication lines. While we have not practically realized such 'bottom up' directed self-assembly, there have been notable theoretical and experimental advances over the last several years. The most mature and versatile non-biological self-assembly approach is clearly DNA nanotechnology (33, 169), where DNA strands self-assemble into building blocks that themselves have different symmetries, and these building blocks in turn assemble into still larger hierarchical structures, with both assembly processes driven and directed by the sequence specific hybridization of the constituent DNA strands. Unsurprisingly perhaps, much of the work to develop a general-purpose directed self-assembly technology seeks to leverage DNA nanotechnology to assemble other available synthetic nanoscale and microscale building blocks.

This review is concerned with techniques that form nanocomposite materials and structures not solely from DNA, but which incorporate nanoparticle and microparticle building blocks as key functional components of the final product. These non-DNA materials can provide desirable optical, electronic, chemical, or even structural properties needed for future material or device applications. Specifically, we will consider the theoretical strategies that have been discovered for versatile directed self-assembly, the limits to those strategies, as well as experimental approaches for forming useful DNA-decorated building blocks, and the successful results of experiments to assemble them in practice.

7.3 Overview of DNA-directed particle self-assembly

A wide variety of different building-block shapes as well as different strategies for assembling them have been reported, both in simulation and experiment. To make sense of this complexity, we can categorize directed self-assembly systems into four groups shown schematically in Figure 7.1.

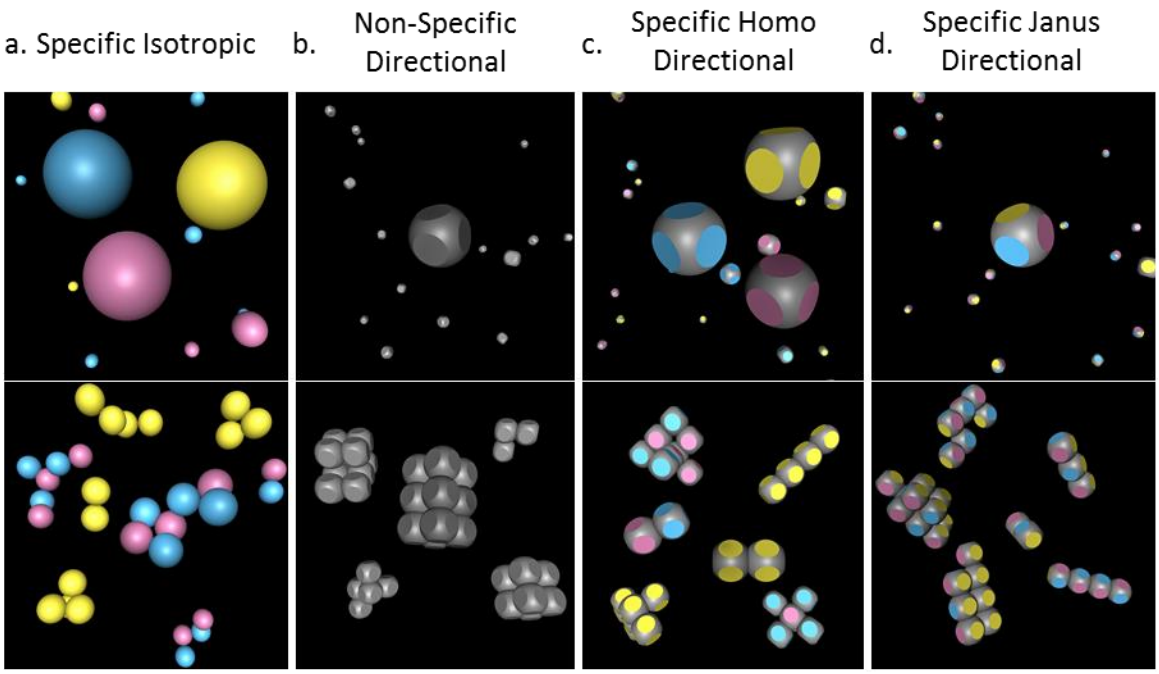

Figure 7.1 Schematic of different classes of self-assembly building blocks. The first row shows the types of building blocks, and the second row shows some example structures these building blocks might form. The notional matrix of interactions for each is yellow binds yellow, and pink and blue bind each other.

The first group would simply be a mixture of different populations of spherical particles (represented by different colors), whose pairwise attractive interactions are isotropic, but chemically specific: only particles pairs bearing complementary DNA strands will bind one another. This approach was first realized for gold nanoparticles by

Mirkin (146) and Alivisatos (170) in the 1990s, and has matured significantly in the last five years. For the binary case (two interacting spheres) oppositely charged colloids can form an alternative realization of this approach (171, 172). The binary specific interaction approach using DNA has been shown to form a variety of crystals from spherical nanoparticles (148, 173, 174) and colloids (91, 141, 175, 176, 177*, 178*) that are typically isomorphic to the crystals of ionic and intermetallic compounds.

The second group would be a collection of particles whose assembly is dictated by their shape, but which do not necessarily have long-ranged attractions or repulsions. Shape is a high-dimensional variable providing a great deal of design freedom (179) parametrically, and in principle a correspondingly wide variety of different final structures. Indeed, Murray(180, 181), Kotov (182), Rossi (183) and others have demonstrated that nanoparticles can form a variety of complex crystalline structures controlled by their shape (sometimes with an admixture of electrostatic interactions). Extensive simulation work by Glotzer(184*) considered the equilibrium structures formed by a variety of polyhedral shapes, uncovering general principles for predicting the final crystal structure (if any) and leading to a key insight—that liquid structural correlations in these particle suspensions can lead to directional interactions of an entropic nature that determine the structures that subsequently form (185*). While purely shape-based assembly is also not our primary focus, Glotzer's work suggest that directional DNA interactions should produce a wide variety of complex structures analogous to those previously reported for polyhedral particles.

The third approach to directed assembly seeks to combine the chemical specificity allowed by using DNA-induced attractive interactions with the design versatility afforded by directional interactions. In general, multiple species of such directional building blocks can be combined to create more complex assemblies than those possible just with entropic interactions. Three general approaches for creating such building blocks have been reported in the last five years. The first, by Pine (186**), creates roughly spherical microparticles with DNA decorating patches on their surfaces, arranged in a chosen polyhedral symmetry, Figure 7.3(a, b). A second approach assembles DNA-covered microspheres into a cluster displaying polyhedral symmetry (140**, 187, 188**), leading to spatially defined sites on the surface with strong binding, Figure 7.4(a, b). A third approach, by Gang (189**), uses DNA-origami methods to build a polyhedral cage around a nanoparticle; different cages interact via complementary DNA strands on their corners, Figure 7.4(c). Most recently, the latter two approaches have also been reported by Gang (190**, 191**) and Pine (188**) to form ordered crystalline assemblies, notably having the symmetry of the diamond and closely related lattices.

The fourth and final approach to directed assembly requires a further generalization: the ability to controllably place different DNA strands on different regions on the building block, such that an ‘A’ particle might interact with a ‘B’ particle only through one patch, and with a ‘C’ particle through a different patch. This approach describes many self-assembly processes from the self-assembly of proteins, DNA

nanotechnology constructs, as well as Janus particles and nanoparticles with both positively and negatively charged faces. While building blocks with 'Janus-directional' interactions have been realized using Gang's DNA origami nanocage approach (189**), their use in self-assembly has yet to be explored. We will review the theoretical work studying the structures possible with this ultimate, 'Janus-directional' self-assembly approach, and consider potential methods for forming suitable building blocks by hierarchical self-assembly.

The central questions of DNA directed self-assembly are "What structures can we make?", "What building blocks and DNA designs do we need to make it?" and "What process conditions are needed to drive robust assembly?". Given the high dimensionality of the building block shape space and the potentially large number of possible building block combinations and mutual interactions, it is obviously foolish to expect fully complete and satisfying answers to these questions. Instead, we start to move forward with analogies from atomic, molecular, and biological self-assembly. Inspired by the progression in Figure 7.1, we might (provisionally) suppose:

*systems with single-component spherical building blocks with non-specific (e.g. depletion) attractions will recapitulate noble gas phase diagrams and 'Lennard-Jonesium'.

*systems with two or more types of spherical building blocks with isotropic, specific interactions (as in Figure 7.1 (a)) will recapitulate the ionic as well as many intermetallic compound and alloy crystals.

*systems of one or more building blocks imbued with non-specific directional interactions via their shape (as in Figure 7.1 (b)) will form a wide variety of dense crystal structures, as well as liquid crystals, and exotic quasi-ordered phases.

*systems of up to a few types of building blocks with specific 'homo-directional' interactions (as in Figure 7.1 (c)) should be able to form all the structures above and recapitulate nearly all the atomic compound crystals known as well as many crystals for which no atomic analog exists.

*systems of up to a few types of building blocks with specific 'Janus-directional' interactions (as in Figure 7.1 (d)) should be able to form all the structures above as well as recapitulate most known molecular crystals and surfactant mesophases, with extensions to more than two components and sub-phases.

*systems with a larger number of building block types should be able to self-assemble almost arbitrary forms, potentially useful as hierarchical building blocks, circuits, microrobots or computing devices. The limits on the complexity and defect density within these assemblies, and the conditions for forming them with isotropic, or homo-directional, or Janus-directional interactions remains a major open question.

7.4 Insights from Theory and Simulation

In the field of DNA directed particle self-assembly, simulation (and theory approaches for computing phase behavior) has generally run ahead of experiment, with many available predictions for interesting structures forming from a variety of different building blocks. Simulations may either contain explicit DNA strands (192*) (typically in a coarse-grained representation), or may subsume the effect of the DNA into an empirical potential (193*). The explicit DNA approach is the more accurate, and sometimes necessary approach, especially under conditions that the DNA density is very low or very high, or the building blocks are small, such that DNA interactions may be non-additive or next-nearest neighbor interactions may play a role. For example, depending on the relative size of the DNA strands and the particle core, the hybridization of DNA between the particles can 'steal' available sticky ends, precluding the binding of additional particles in some locations. This effect has been used to drive directional structure assembly and is best captured with an explicit DNA representation. Conversely, for larger particle systems where it is valid, the empirical potential approach is more easily implemented in simulation (and amenable to analytic methods), numerically far less costly and thus facilitates the exploration of the potentially vast, multi-dimensional phase diagrams or design parameter spaces considered.

At the field's current exploratory stage, concerned with global features of the phase diagram and possible assembled structures, the accuracy of the DNA-induced

potential model is sensibly not a major concern. Different authors use different functional forms such as square-well, Lennard-Jones (or modifications thereof) or empirical potentials generated from models (193*) or direct measurements (130*) of interacting DNA brushes. Parameterizing the spatial and angular extent of the interactions (and optionally binding valence, dihedral angle constraints, etc.) between building blocks, and defining the matrix of relative energetic strengths of the attractions between different particle populations should suffice for mapping out phase behavior and structure formation; with the phase boundaries presumably only being weakly sensitive to the exact form chosen for the potential. Indeed, it seems likely that we can sometimes gain fruitful insights from earlier studies of simpler directed assembly processes with hard polyhedral interactions or isotropic DNA interactions (as in Figure 7.1 (a, b)), which completely neglect the DNA potential or its directionality.

Notably, ordered clusters of spheres can themselves act as directional interacting building blocks when covered with DNA, functionally equivalent to the more conventional 'patchy sphere' concept. Intuitively, when spheres approach clusters having complementary DNA, there are locations on the cluster surface where the sphere can bind 3 (or more) of the cluster's constituent particles. The fact that clusters of uniformly DNA coated spheres could act in many ways like DNA patchy colloids was pointed out in groundbreaking work by Geissler (194**), who reports such clusters form a wide variety of different structures in simulation. Subsequent experimental work by Crocker (140**) and simulation work by Sinno (195**) has corroborated this idea. Pine

has shown in simulation that DNA-colloidal clusters from multiple complex phases in simulation (188**).

The simplest way to form an ordered polyhedral cluster is simply to have two species of spherical particles, in which a minority particle interacts strongly with a majority species that is present in significant excess. In this case, the number of majority particles that can sterically fit around the minority core depends on the size ratio of the two particles and whether the binding is reversible or not. In the reversible case, the final state has a maximum density and polyhedral symmetry given by the long-studied 'kissing sphere' or Tammes problem (196*). In the irreversible case, the final state is the result of a so-called parking problem; if the first few spheres arrive in unfavorable locations, they can block the addition of later particles, leading to a final state with fewer surrounding spheres than the equilibrium case. In a fascinating result (197*), Manoharan computed that for a special majority/minority size ratio, the minimum valence possible with irreversible binding is four, and also corresponds to the maximum possible case, suggesting that a directed assembly process would yield clusters with valence four at essentially 100% yield. Chemical means for controlling valence could also serve the same purpose (198*, 199*), and will be discussed in Section 7.5.3 . Notably, however, the degree of disorder of these self-assembled clusters is an important variable in applications, and will generally be higher for irreversible assemblies and will depend on how close the particles are to the limiting diameter ratios and valences specified by the Tammes solutions.

We will divide the work predicting the outcome of DNA-directed self-assembly into three groups, according to the class of final structure being targeted: ordered assemblies (e.g. nanoparticle or colloidal crystals), mesophase-like assemblies (e.g. filaments or membranes) or 'custom' structures having a high degree of complexity.

7.4.1 Ordered Assemblies:

Nanoparticle and colloidal particle assemblies have been proposed to form plasmonic, photonic or phononic metamaterials, so much work seeks to direct the assembly of the structures needed for those applications. For plasmonic structures, one goal is to form ordered polyhedral clusters of particles (200), (discussed above) and then to optionally assemble them into higher order structures. For photonic materials, the emphasis is on forming assemblies that are isomorphic to the structure of cubic diamond or structures with similar symmetry (201), which are notoriously difficult to form by self-assembly and have been the subject of much attention. For phononic metamaterials, the simple cubic lattice and related structures are also of particular interest (202).

Self-assembling colloidal crystals having the structure of a diamond lattice has been a goal in the field for two decades. One unusual feature of the diamond lattice is its packing density (about 0.34 of volume fraction for touching spherical 'atoms') or exactly half that of body-centered cubic (bcc). This makes it unlikely to form as the result of simple dense packing (which favors higher volume fraction structures) or due to

isotropic attractive interactions (which favor coordination numbers greater than 4). A long-standing idea (203) is that directionally interacting particles, whose interactions mimic those of the bonds in atomic diamond, might self-assemble into a diamond lattice as well. Extensive studies by Sciortino and coworkers have considered building blocks having tetrahedrally arranged directional interactions. Early work (204*) showed that such patchy spheres do not only form diamond; hexagonal diamond (205**), disordered networks (206) and two liquid phases (207) compete with cubic diamond formation. Another study (208**) has shown that dihedral angle control is key to stabilizing the diamond structure. That is, when two building blocks come together, they must not be able to freely rotate about the line connecting their centers. Specifically, if pairs of patchy spheres prefer to have their other three patches rotated by 120° relative to one another, then the system can form conventional (cubic) diamond. Conversely, if the patches are designed to align the two patchy spheres' other three patches, the particles will tend to form a different structure—hexagonal diamond. In a joint experimental-computational study, Glotzer and Murray (209) demonstrated that nanocrystals can be self-assembled into quasicrystalline structures, and that this process can be understood through biases for certain vertex configurations. Notably, Frenkel (210**) shows that Janus-directional building blocks (as in Figure 7.1(d)) can stably form cubic diamond even in the absence of dihedral angle control, and offers two working building block designs.

The low density of some expected lattices can lead to unexpected complexity. Kahl (211*) points out that it is geometrically possible to interleave two cubic diamond lattices within one another, forming a bcc structure if the two lattices are formed of the same particle; such a tetrahedrally coordinated bcc lattice and its variants are observed in some regions of the phase diagram. Such complex phase behavior is not limited to tetravalent patchy spheres, Louis shows a similarly complex phase diagram for octahedrally patchy particles that might be expected to form simple cubic lattices (212*), and Mao (213) demonstrated that triblock Janus particles undergo a phase transition from open to close packed lattices. Lastly, an extensive survey of different patch geometries and interactions, by Dijkstra and Kahl (214**), confirms the structures predicted by others, as well as body-centered tetragonal (BCT) and still more structures.

These diamond-like tetrahedral bcc phases suggest another approach for self-assembling diamond: form a different denser lattice that contains a diamond lattice of one species as well as other building blocks filling the interstitial space. In practice, one can suppose self-assembling the composite structure and then chemically removing the non-diamond structure. Work by van Blaaderen and Dijkstra (215*, 216*) suggests such an approach, specifically the formation of a structure isomorphic to an $MgCu_2$ Laves or C15 lattice. In one realization, the $MgCu_2$ phase consists of a diamond lattice of touching large spherical building blocks, with smaller spheres arranged in tetrahedral groups and nearly filling the tetrahedral interstitial spaces in the diamond lattice. The situation however is rendered more complicated by competing Laves phases ($MgZn_2$ or C14; $MgNi_2$

or C36) that do not contain a diamond sub-lattice, but which have very similar density, particle coordination and free energy (not unlike the fcc-hcp stacking degeneracy in hard spheres or spheres with non-specific isotropic attraction). The authors have proposed two approaches to breaking the degeneracy, in one they nucleate crystal formation on a patterned surface to select $MgCu_2$; in the second they proposed to pre-form the smaller atoms into close-packed tetrahedral clusters (which are present only in $MgCu_2$). While van Blaaderen and Dijkstra have proposed simple packing of the building blocks to form $MgCu_2$, Pine has shown that a similar approach may be used with DNA interactions (188**), taking advantage of the directional interactions inherent to cluster-sphere interactions, which is discussed in greater detail in Section 7.6.3 .

Geissler's pivotal work (194**) reports the formation of low-packing fraction cubic space group crystals from octahedral cluster building blocks consisting of three different types of constituent spheres, Figure 7.7.2(c). When the building blocks have specific Janus-directional interactions (as in Figure 7.1 (d)), individual building blocks can freely rotate about a bond direction axis in the final assembly. Octahedral building blocks containing four different building blocks are found to form an fcc type crystals in which the building-blocks cannot rotate, and which either show compositional long-range order or not depending upon the details of the matrix of constituent interactions.

Sinno (195**) simulated the formation of ordered assemblies from polyhedral clusters via an intuitive approach in which clusters interact with each other only indirectly through small 'bond spheres' that occupy sites between them (which contain

complementary DNA). The appeal of this idea is that the symmetry of the cluster might determine that of the crystal: cubic blocks should form simple cubic, octahedral blocks should form bcc and tetrahedral blocks should form diamond-like crystals. With some adjustments to how the bond sphere and clusters interact, and the shape of the clusters, they were indeed able to form each of these expected crystal types. Unlike the case of Geissler above, the cluster building blocks needed to contain only one or two different interacting species. In the case of diamond-like assemblies, however, the resulting lattice does not contain a compositionally distinct diamond sub-lattice, so it does not provide an obvious route for assembling photonic materials.

7.4.2 Mesophase-like Assemblies:

Another interesting question is what sort of mesostructures can be achieved through directional and specific interactions, and what level of detail do we need in simulations to achieve them. As already discussed in Section 7.4.1 , Geissler (194**) looked extensively at the types of structures clusters of interacting particles could make. Using tetrahedral clusters with one interactive node, micelles were formed. By adding a second interactive node to the cluster, filament-like structures could be formed, and clusters with three interactive nodes formed bilayer sheets. It is also interesting, that by reducing the system to a triangular cluster with two interacting nodes, bilayer sheets also formed, owing to the reduced steric hindrance present in the tetrahedral case. Patchy particles have received a lot of interest for their ability to form rings, helices, and

other such structures. Sciortino (217) and Telo da Gama (218) have both investigated the ability of patchy particles to form rings and the use of Wertheim perturbation theory to describe these systems. Indeed, Sciortino showed that Wertheim theory could be used to great effect in describing simulations of ring and chain forming patchy particles. Sciortino (219) also investigated the use of cylinder particles with interactive ends, finding that using a model of equilibrium polymerization of the cylindrical particles properly gives the experimental results showing that with certain volume fraction and aspect ratio of particles, liquid crystal phases form. Peeters (220**) studied the self-assembly of Janus particles, finding that when confined in channel-like environments these particles form helices, and by tuning the interaction and repulsion energies of the different hemispheres, through salt, the helices pitch and morphology could be tuned. Wales (221) also investigated the formation of helical superstructures using dipolar Janus particles, this time controlling pitch length with external magnetic fields. While these results depend on the interplay of the attractive and repulsive interactions, it remains to be seen if such structures could be formed with DNA patchy particles that do not have the same charge repulsion properties.

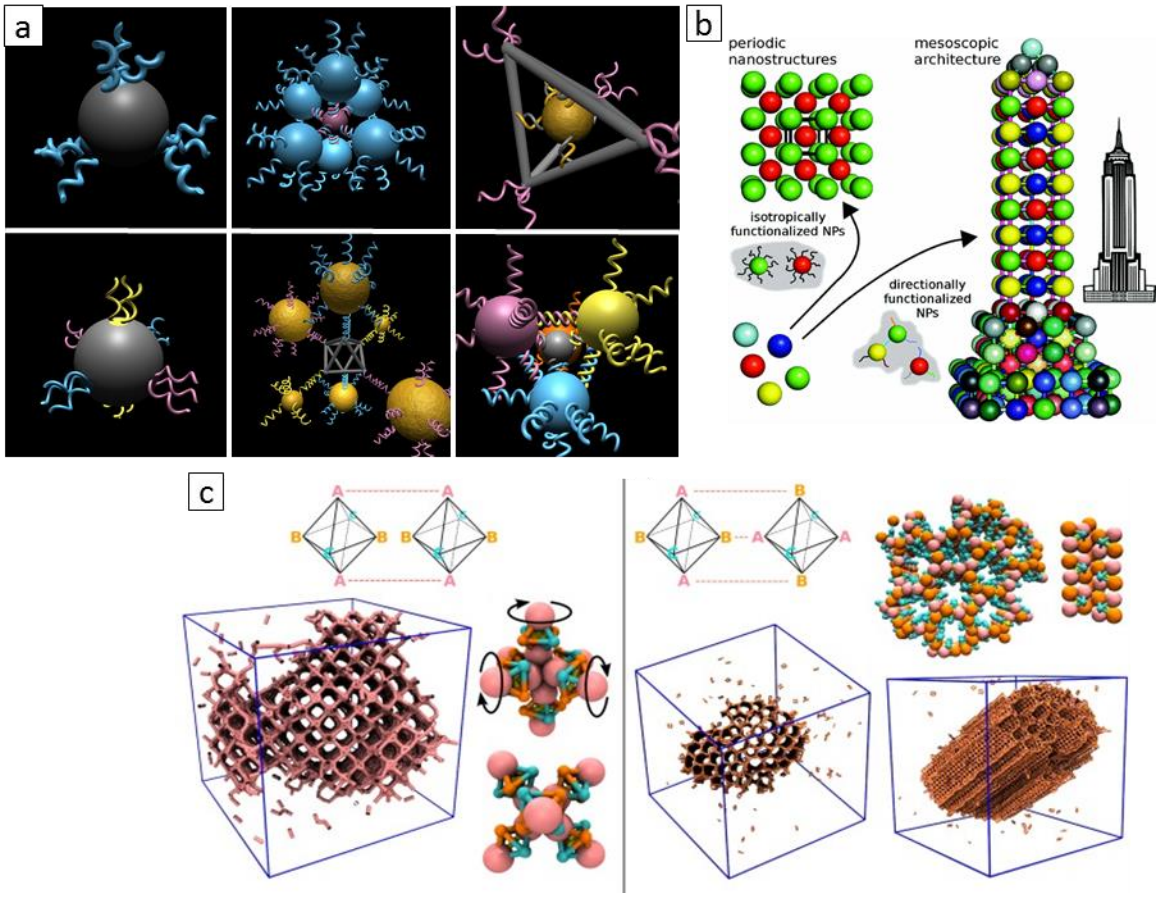

Figure 7.7.2 (a) Top row shows realizations of Specific Homo Directional building blocks (as in Figure 7.1 (c)) that have been shown experimentally, from patchy particles, DNA grafted clusters, and DNA nanocages. The bottom row shows realizations of Specific Janus Directional building blocks. While patchy particles and clusters of this type have not been realized experimentally, DNA nanocages have (189). (b) Simulation results using isotropically and directionally functionalized nanoparticles. Using isotropically functionalized nanoparticles many crystal structures have been made. Using directionally functionalized nanoparticles of many flavors, simulations suggest that structures of arbitrary shape and scale can be formed (222**). (c) Simulated results of anisotropic clusters to form various crystal structures (194**) By controlling the symmetry, and interaction matrix of the clusters, a panoply of crystals and mesophases can be assembled.**

Finally, much work has been done to study the gelling properties of patchy particles (223*). Truskett (224*) used a clever method to emulate particles with limited valence, by using a system of two particles, primary and linker both of which are

isotropic. By controlling the relative stoichiometry of the linker particle to the primary particle, the effective valence of the primary particles could be controlled. Sciortino (225-228) has extensively studied gelation of patchy particles, and temperature dependent patchy particles. By introducing competing interactions, he has shown that patchy particles can exhibit a liquid to gel to liquid phase transition as temperature increases. Additionally, by tuning the interaction energies of each patch on a patchy particle, Sciortino has investigated particles with temperature dependent valence. It seems that the tunability of DNA with temperature, salt, and competing strands, should allow for experimental analogs to these simulations in the future.

7.4.3 Custom or Complex Assemblies:

An open question is what are the limits of directed assembly—can we form a large artifact of essentially arbitrary structure from many distinct building blocks? It is generally believed that if you wish to assemble a single unique artifact or structure from a closed system of *N* particles, then one should design a set of *N* distinct particles having pairwise attractions where each particle is assigned to bind only to its neighbors in the desired target structure. If the interactions are also appropriately directional (or the structure is nearly close-packed), then it should be possible to form the assembly for a suitable interaction strength and waiting time, even if *N* is large. Indeed, this case might be said to describe the situation in DNA nanotechnology—in DNA origami, there can be hundreds of single-valence staple strands, and complex assemblies can be formed at

respectably high yield. The formation of comparably complex assemblies has not yet been demonstrated for DNA-directed particle assembly, but simulation work provides useful insights.

One important question is the limit on the number *N* of distinct interacting particles one can form. Unlike the single DNA strand 'staple' in origami, the large number of interacting DNA strands on particle building blocks admit the possibility that particles with partial sequence complementarity could give rise to weak interactions that frustrate assembly. Moreover, the large number of interacting strands typically requires that the length of the DNA sticky ends be relatively short, restricting the size of the corresponding combinatorial sequence space. This question was addressed by Chaikin and Seeman (229**), who computationally generated a large library of DNA sequences and then screened out ones with 'off target' interactions due to partial complementarity. In the end, they concluded that roughly 100 different specifically interacting strands could be engineered using 11 base 'sticky ends', or conversely, that numbers much larger than 100 were presumably difficult, infeasible or require an expansion of the 'sticky end' length.

Brenner (230**) considers the yield of an equilibrium directed assembly process of a closed system of *N* particles, as described above, into a specific close-packed artifact. Notably, they use spherical building blocks with isotropic but specific interactions, as in Figure 7.1(a). When each particle only interacts with its neighbors in

the target structure, their findings suggest a limit of roughly N = 1000 for equilibrium assembly at high yield. They point out that this figure is greater than the number of available strands in plausible libraries, but argue that sequences can be reused to an extent (e.g. programming interactions between particles A and B as well as between particles E and F) without introducing problematic competing structures. They point out, however, that suitably fast binding kinetics have not yet been demonstrated for systems with large numbers of interacting strands.

Tkachenko also considers the directed assembly of complex artifacts (222**), but with some noteworthy differences from those above. First, they consider a system with excess building blocks, as a proxy for bulk assembly processes that would be performed in effectively unbounded suspensions. Second, they argue that 'Janus-directional' specific interactions (as in Figure 7.1(d)) are required to avoid trapped states that frustrate assembly. This makes intuitive sense, as the resulting valence control would avoid the unwanted binding of excess particles in the wrong location. With these specifications, they demonstrate the reliable formation of assemblies as large as N = 671 constituents, Figure 7.7.2(b). In general, they too argue that fewer than N distinct DNA interactions are required for effective assembly. They report a variety of methods for improving yield and growth kinetics, most notably the modulation of interaction strengths (which can be tuned with temperature) so that nucleation is controlled. In general assembly proceeds in stages, with sequential addition of new particle generations as the simulated program temperature is varied.

In conclusion, it appears that with Janus-directional specific interactions, à la Tkachenko, very complex assemblies can be formed at high yield with practical strategies for DNA sequence library design and processing strategies. As for how to form the Janus-directional building blocks required, the answer is obvious; hierarchical self-assembly, e.g. from spherical building blocks with isotropic, specific interactions into small clusters of specific polyhedral shapes. This should be possible, even in open systems, using the design methods of Brenner (230**) and process methods of Tkachenko (222**), provided certain (e.g. chiral) building block structures are intentionally avoided. It certainly seems plausible that small cluster building blocks with $N = 8$ could be produced in bulk at high yields, and that these would have suitable valence with a comparable number of nearest neighbors (as in Geissler (194**)). Obviously, different building blocks could be assembled in separate bulk suspensions (avoiding the combinatorial challenges of co-assembling them separately in the same suspensions), and then mixed together. Importantly, multiple techniques for permanently crosslinking small DNA particle assemblies have been developed, as well as reprogramming the interactions of given particles through competitive binding, temperature modulation and strand exchange reactions. These methods should suffice to decouple the two stages of assembly, such that interactions can be used to form building blocks, and then different interactions can be activated for the second round of hierarchical assembly.

7.5 Making Building Blocks:

While theory and simulation has been able to take advantage of a limitless array of anisotropic building blocks, experimentalists have been working to realize many of these constructs, with the ultimate goal of making individually tunable directional specific interactions. To this end, there have been numerous recent advances in colloidal cluster, patchy particle, and DNA nanocage formation which, to varying degrees, have realized both directionality and specificity of self-assembly building blocks.

7.5.1 DNA Structures:

DNA has been used to make a variety of DNA superstructures (231). Bellini (232, 233) showed that short DNA oligomers can be used to form liquid crystal structures. DNA origami and DNA nanostructures have been used to make an immense array of nanoscale structures. Chandrasekaran and Levechenko (32) wrote a nice review in 2016 on some of the recent developments in constructing DNA nanocages. Of particular interest to us has been the development of hierarchical DNA structures, and hybrid DNA/nanoparticle structures. Mao (234) showed that DNA nanocages can be engineered to encapsulate DNA functionalized gold nanoparticles. Another nanocluster formation approach (235) takes advantage of DNA nanocages, which can be used to direct cluster formation. Using this approach, tetrahedral, octahedral, and triangular bipyramid clusters have been made. Gang (189**) realized the ultimate anisotropic

building block using DNA frames and nanoparticles. In their approach, they form polyhedral DNA structures where each vertex has a prescribed flavor of DNA strand available for hybridization/binding. They then introduced multiple flavors of DNA-grafted nanoparticles, which then bind to the predetermined vertices of the DNA structure, thus creating clusters with multiflavored directional interactions, Figure 7.4(c). This type of design could easily be imagined for a wide array of DNA frame shapes and allows for the precise control of directionality and specificity of DNA-mediated interactions. This nanocage-nanoparticle motif has been used to self-assemble crystal lattices as will be discussed below in Section 7.6.3 .

7.5.2 Clusters:

There have been a number of developments in creating and understanding disordered clusters. Chaikin and Seeman (229**) first explored the use of “polygamous” particles for cluster formation. They demonstrated that by controlling the interaction matrix between multiple species of particles, cluster formation could be controlled and lead to hierarchical formation such as two-shell systems. The authors also demonstrated the large library of particles this method could take advantage of, conjecturing that ~100 “flavors” of particles could be used in a single system. Hecht and Bausch (236*) extended this polygamous particle approach by adding linker DNA strands to control when different particle species could interact. This allowed the team to build multiple initial clusters, which with additional linker strands, could be made to interact forming

mesoscopic structures. Other groups (237, 238) have investigated the use of nanorods and viruses coated in DNA-grafted nanoparticles and shown that they too can self-assemble.

To create ordered clusters, templating or multistep processes are required. Capasso (200) formed quadrilateral nanoparticle pentamers by mixing two species of complementary particles together to form pentamer clusters. These clusters were then dried, during which capillary forces compressed the clusters into a close-packed two-dimensional configuration. Kotov (239**) made chiral nanoparticle pyramids by first making different dimers which when mixed together, formed tetrahedral clusters. For colloidal-scale cluster formation, crystal templating has shown promise in building a library of ordered colloidal clusters. Crocker (140**, 187*) made clusters, by first making two component crystals through DNA interactions. Then, by introducing ligase into the system, the host and impurity particles are enzymatically stabilized for future purification as shown in Figure 7.4(a). This approach has produced tetrahedral, octahedral, cuboctahedral, triangular orthobicupula, and icosahedral clusters. Additionally, since these clusters exhibit directional interactions, they allow for further hierarchical self-assembly.

Several methods have been reported to form clusters without DNA. Wolf (240) used sequential capillarity-assisted particle assembly to form a wide range structures, including dumbbells, triangles, and chiral tetrahedra. Duguet (241) uses seeded-growth

emulsion polymerization process to form multipod structures consisting of a silica core and polystyrene satellite particles, allowing for the targeted formation of tripods, hexapods, and other symmetries. Bon (242) reported a hierarchical self-assembly method of 'hard-soft' Janus particles into colloidal molecules. These methods in conjunction with Pine's (243) work in grafting DNA to colloids with a wide range of chemical compositions suggests a new frontier in forming DNA functionalized clusters for use in self-assembly.

7.5.3 Patchy Particles:

On a nanoscale, anisotropic DNA-grafted particles are quite developed. Mirkin (244) took advantage of the ability to make an array of nanoparticle shapes which can then be functionalized with DNA. These DNA-functionalized anisotropic nanoparticles then were self-assembled into a range of crystals. They also demonstrated that as the DNA length changes, for a given particle shape, the crystals undergo phase transitions. Another approach for making patchy nanoparticles (245**) takes advantage of DNA origami's flexibility. In this approach, DNA-functionalized nanoparticles are mixed with DNA origami, which, depending on the DNA-origami design, allows for valence and dihedral angle control of the interactive patches, Figure 7.3(d). While these authors used this "DNA Origami Nanoflower" construct to self-assemble 1-D and 2-D lattices, Figure 7.3(e), it is easy to envision it being expanded to 3-D lattices and heterogenous patchy particles.

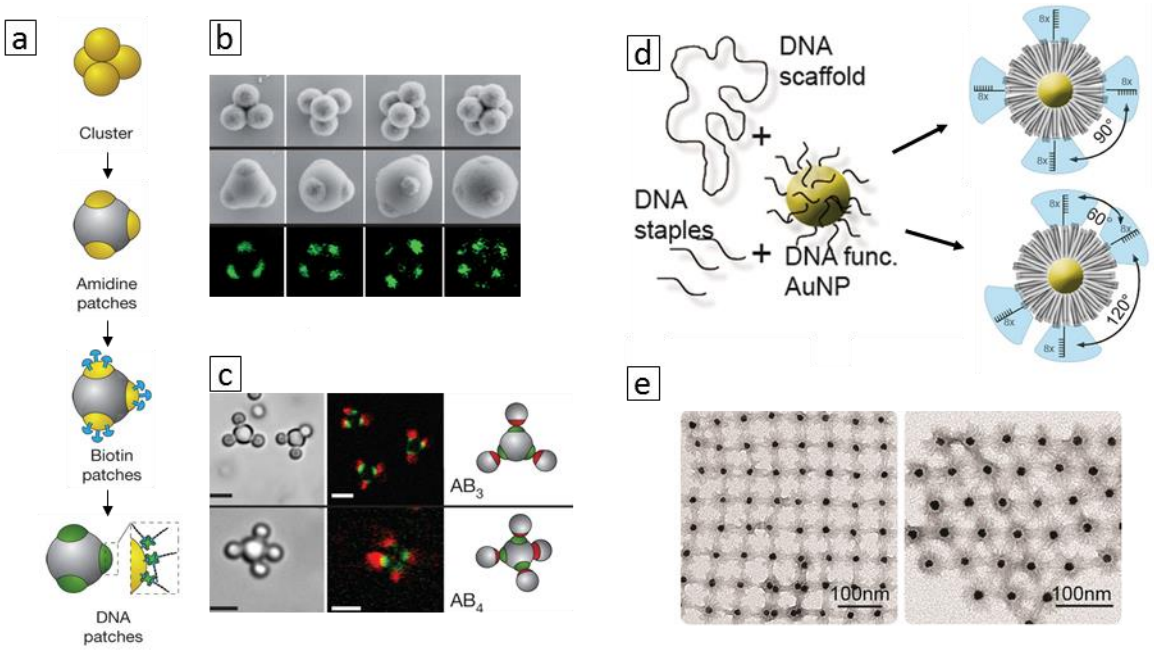

Figure 7.3 (a) Schematic of DNA patchy particle formation via clusters and (b) resulting patchy particles for various starting clusters. Here the valencey and symmetry of the resulting patches are determined by the initial cluster, and the patch size is prescribed b by the degree of swelling and polymerization of the cluster. (c) Use of the patchy particles to form various colloidal molecules (186). (d) Schematic of DNA nanoflower assembly and resulting valence and dihedral angle control. (e) Using the nanoflower patchy particles, one and two dimensional structures were formed based on the valence and dihedral angle (245**).**

On the microscale, Chaikin (142*) used a DNA functionalized surface which allowed for the selective functionalization of DNA onto bound particles. This yielded single patch particles which were then used to form dimers and clusters. Pine's (186**) method for creating patchy particles (Figure 7.3(a)) starts with making an emulsion of particles to form clusters. These clusters are then swollen and polymerized, such that the extremities of the particles that protrude from the center of the swollen cluster can be functionalized with DNA, while the swollen interior portion is inert. By varying the

degree of emulsification and swelling, the valence, symmetry and patch size of these patchy particles can be well controlled. This method has been further developed (246) to form bifunctional patchy particles. Still another method (198*, 199*, 247*) for creating building blocks with controlled valence uses emulsion droplets, the surface of which is covered in DNA strands. When complementary droplets or particles bind together, the DNA on the emulsion droplet can diffuse on the droplet surface to its complement, forming dense patches of hybridized DNA, whose size is determined by a balance of surface tension and hybridization energy. By controlling the DNA inventory of the droplet, the valence of the resulting patchy particle can be controlled. Notably, one can imagine introducing multiple species of DNA into a single droplet to create heterogenous patches on a single particle using this method.

7.6 Assembling Building Blocks:

7.6.1 Spherical Isotropic Specific Building Blocks:

Using DNA functionalized spherical nanoparticles and colloids, many ionic, intermetallic, and alloy crystal symmetries have been recapitulated. Rogers, Shih, and Manoharan (125) recently wrote a nice review of colloidal and nanoparticle self-assembly and highlighted many of the symmetries that have been realized so far, as well as the design rules for engineering such symmetries. Of particular note have been the Mirkin (174) and Pine (141) labs, whom have realized many different colloidal crystals at both nanometer and micrometer size ranges, by varying the stoichiometry and size ratio

of particles. Most recently, the Crocker lab (180**) created a double diamond structure with microscale colloidal particles.

7.6.2 Nonspecific Directional Building Blocks:

Again, while not the focus of this article, there has been much development in the field of shape driven self-assembly. A few of the notable studies include Murray's (248) use of shape-complementary building blocks to form nanocrystal "puzzles" and Pine, Sacanna, and other's (249-252) work on "lock and key" colloids

7.6.3 Specific Directional Building Blocks:

By adding specificity and directionality to building blocks, a variety of crystalline and interesting mesostructures have been made. There are three main approaches that have been used so far: shaped nanoparticles and clusters, patchy particles, and DNA structure assisted architectures.

Using shaped nanoparticles (253), Gang and Tkachenko used DNA-grafted nanorods and nanoparticles to assemble one-dimensional ladder-like structures. Gang (254) showed that mixtures of isotropic spherical and anisotropic shaped building blocks can form interesting DNA mediated structures. The Mirkin group has been very active in using anisotropic DNA functionalized nanoparticles to form crystal lattices. They showed that by varying the shape and aspect ratios of their nanoparticles, they can induce one, two, and three dimensional self-assembly (244). They have also investigated shape

complementarity (255**). In that study, they engineered nanocubes with convex, flat, and concave faces, and investigated how this affected the co-crystallization. Their results showed that as shape complentarity, measured through packing efficiency, decreases crystallinity decreases. In that same study, they also investigated a system of disks and cubes, changing the relative width of the disk to the cube size. Interestingly, they found that as the width of the disk increased, their system went from a disordered, to a three-dimensional crystal, to a one-dimensional stacking. They have also investigated the effect of the DNA corona around the nanoparticles (256), finding that as the DNA length increases for a given size nanocube, the particles assemble into cubic, then body centered cubic, then face centered cubic. The size of this "zone of anisotropy", the regime were the particles do not behave as spheres, was found to be particle shape dependent, with cubic nanoparticles having a smaller zone than octahedral and rhombic dodecahedra, holding the size and DNA per particle constant. Finally, they have demonstrated that by tuning the DNA length and nanoparticle size, the overall crystal habit could be precisely controlled (257*). On the microscale, Crocker (140**) has also used shape and specificity as a means for self-assembly. In this study, crystal templated clusters were shown to have directional interactions allowing for hierarchical assembly of higher level structures, despite the constituent spheres being uniformly coated in DNA, as shown in Figure 7.4(b).

Using patchy particles, here meaning spheroid particles with anisotropic interactive regions, a variety of microscale and nanoscale structures have been formed.

Seeman and Chaikin (142*) make one patch particles to assemble dimers. Pine (186**) demonstrated the use of patchy particles to emulate atomic binding, shown in Figure 7.3(c). By controlling the valence, dihedral angle, and patch size of particles, they were able to create structures analogous to atoms with monovalent *s* or *p* orbitals, as well as multivalent *sp*, sp^2, sp^3, etc. orbitals. As already mentioned, (245**) DNA origami has been combined with nanoparticles to form patchy particles. Turberfield also demonstrated an ability to control the valence and dihedral angle of the formed patchy particles. This control allowed them to form both square and hexagonal lattices and could easily be imagined to be extended to three-dimensional lattices as well.

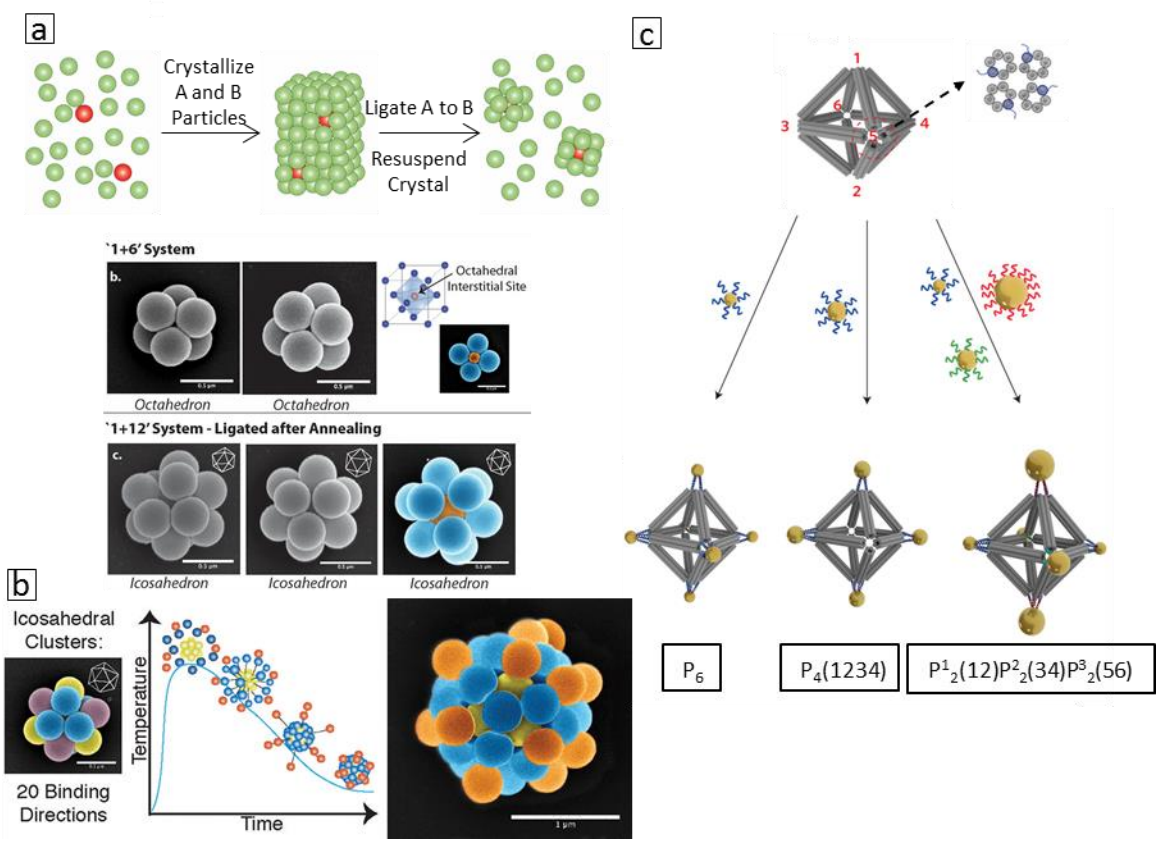

Figure 7.4 (a) Schematic of crystal templated cluster formation, in this case using a sedimentation crystal and resulting clusters formed by controlling for particle size ratio . (b) DNA particle clusters exhibit directional interactions. Cartoon shows schematic of hierarchical assembly. The right image is the result of this hierarchical assembly for an icosahedral cluster, with the yellow particles forming the icosahedral cluster, the blue particles bound to the faces of the icosahedral in a dodecahedral symmetry, and the orange particles bound to the vertices (140). (c) Schematic for using DNA nanocages to assemble nanoparticle clusters of prescribed symmetry. By controlling the complementarity of the vertices of the DNA nanocage to DNA nanoparticles, specific Janus directional clusters can be formed (189**).**

Finally, using DNA structures as a guide for specific directional interactions, a wide array of structures have been formed. Urban et al. (258) used DNA origami to assemble toroidal metamolecules. The resulting toroids had a helical band of interactive DNA around them, which allowed for DNA-grafted nanoparticles to bind to the toroid. The resulting structure, resembling an electrical inductor, was then shown to have plasmonic

properties dependent on which direction the nanoparticles were wound around the toroid. There have also been several studies using DNA origami structures to guide nanoparticle assembly. Takabayashi et al. (259), for instance, assembled one dimensional arrays of DNA-grafted nanoparticles onto DNA nanotubes with high yield and controlled particle spacing. DNA origami has been used in a variety of ways to form two-dimensional lattices. For over a decade, groups have used DNA nanoscaffolds to template nanoparticle lattices (260, 261). Woo and Rothemund (262) used DNA origami rectangles with interactive corners to self-assemble checkerboard lattices. Schulman (263) has also demonstrated the directionality and specificity of DNA structures by assembly DNA nanotubes into DNA “nun chucks”. Mirkin (264) used lithography to assemble lattices of DNA-grafted nanocubes. In their approach, they take gold coated wafers and spin coat a PMMA surface on top. Then, using electron beam lithography, they can define lattice nodes on the surface. The exposed nodes are then functionalized with DNA. Then, when DNA-grafted nanocubes are introduced, the nanocubes adhere to the functionalized region of the substrate, resulting in a well-ordered lattice. In three dimensions, a variety of crystal structures have been made. Gang and Tkachenko (191**) used a system of anisotropic and isotropic building blocks to create diamond and face centered cubic crystal structures. In their system, the anisotropic building blocks were tetrahedral DNA nanocages, which were either empty or filled with a DNA-grafted nanoparticle. Then, the DNA nanocages were combined with nanoparticles complementary to the corners of the nanocages, which then self-assembled into diamond or face centered crystals, depending

on whether the nanocages were filled or empty, respectively. Gang (190**) has also used this architecture with a variety of DNA nanocage shapes and explored the resulting crystal structures.

In an exciting recent paper, Pine and coworkers have demonstrated (188**) the use of preformed tetrahedral clusters, having directional interactions with complementary spheres, to form colloidal crystals isomorphic to the $MgCu_2$ Laves phase (as well as a cubic group crystal with no atomic analogs). As predicted by simulation, the spheres and clusters were arranged such that each sphere bonded to a hollow between three complementary particles on the cluster. They find that in general careful attention must be paid to the relative sizes of the building blocks and their geometry, and that attractive interactions between the spheres are needed to stabilize the final structures. The realized $MgCu_2$ structure is of interest because it contains both a close-packed diamond and pyrochlore lattice, both of which have been shown to form a complete photonic bandgap for building blocks with physically realizable indices of refraction. To realize the long-standing goal of self-assembling a photonic bandgap material, additional work will be needed to replicate the colloidal crystal in high index materials, crosslink the desired sublattice, selectively dissolve the other sublattice and dry the result.

7.6.4 Janus-Directional Building Blocks:

While nano-particles with “Janus-Directional” interactions have been realized in experiment (191**), their use as a building block has not been fully explored. However, at the DNA-structure level, this degree of tunability and control has already shown some of the possibilities for the types of structures that can be realized. Sciortino and Bellini (265, 266) have used DNA tetramers to study gelling properties of DNA assemblies. However, owing to inherent flexibility of the DNA arms, simulations show that these architectures will never crystallize (267). Yin (268**) designed a DNA brick system where each brick is a single stranded DNA subdivided into 4 domains. In their system, each DNA brick is unique and can only bind to four other distinct bricks, two in the front and two in the back. This allows for a LEGO® like building process where each layer of bricks is orthogonally oriented from the next layer. Using this system, the team made cuboids of a range of aspect ratios. Additionally, since each of the bricks was unique, by including or excluding specific bricks in the self-assembly process, cuboid structures with pre-determined cavities and voids were made. This process has been replicated in simulation, and displays interesting nucleation and growth behavior of relevance to forming complex DNA-particle assemblies (269).

7.7 Conclusions

DNA has proven itself remarkably versatile for engineering building blocks having specific and directional interactions, at both the nanoscale and microscale, using

‘bottom up’ directed self-assembly. Despite new structures and self-assembly approaches appearing at a steady clip, several crucial open questions remain, many related to the prospects for useful applications. Can the building blocks be fabricated in a scalable manner, in sufficient quantity and at an acceptable cost? Once those hurdles are overcome, can the nucleation and growth of crystals (e.g. for metamaterials) be controlled so as to create suitably large and oriented crystals, and can those crystals be processed into a form (e.g. dry and solid) suitable for the end use? Can mesoscale assemblies be processes to create advanced functional membrane technology? Many advanced materials are integrated with microlithographic processes—can the typically aqueous and wet environments in which DNA materials work be made compatible and integrated with more traditional microlithographic processes? Perhaps alternatively DNA-directed particle assembly can be made compatible with additive manufacturing (3-d printing) or roll-to-roll processes that require its unique photonic activity in a large area, like photovoltaics, or chemical functionality for reactive membranes. It is clear that the versatility and scalability of DNA technology is far from exhausted, and we will find endless ways to employ it in producing new technology.

Chapter 8 Conclusions and Future Work

8.1 Conclusions

In this thesis, we have investigated the adhesion of particles through discrete, multivalent ligand binding in a shear flow. We used DNA as a model ligand to help us understand the underlying physics behind these problems. We built an experimental system where single stranded DNA was ligated to a glass substrate and particles were functionalized with complementary DNA. Then using microfluidic techniques, the particles were perfused over the DNA functionalized glass, and their behavior could be monitored using microscopy techniques.

In our first experiment, we designed the particles to have a strong binding interaction with the glass. This interaction leads to the irreversible deposition of the particles to the glass, creating a sub monolayer on the glass surface. By analyzing the microstructure of this monolayer, we saw that there was a significant effect where once a particle was deposited, it hindered future deposition behind it, and this effect grew stronger as the shear rate increased. This finding was surprising because at the low Reynolds number of this experiment, it might be expected that particle trajectories around a stuck particle would be symmetric. However, our collaborators calculated particle trajectories for a particle near an adhered particle and corroborated our hypothesis that this feature is a result of the particle-to-particle “collision”. In their calculations they showed that a particle flowing past an adhered particle will be “lifted”

by the hydrodynamic interaction between the two particles, and it is this hydrodynamic lift that causes the hinderance of particle deposition. Additionally, we found that the kinetics of the experimental data could not be modeled well in their simulations without including this effect accurately. This result provides guidance for future efforts to model the deposition of particles and cells in a flow field as to what hydrodynamic effects are important to include to capture the experimental system with high fidelity.

The DNA system used in these monolayer experiments was also designed to allow for the turning on of particle-to-particle interactions in a way that would allow stuck particles to "recruit" unadhered particles to the aggregate, analogous to how platelets can signal for more platelets to join the clot. However, in our experimentation, we were not able to get this behavior to work, and so investigated the potential failure modes of the experiment. The DNA design used was intentionally designed to have a large energy of hybridization, to take into account the increasing drag force a subsequent layers of the aggregate would feel, and the geometric impediment for a particle to bind to another particle as opposed to the wall. However, it was determined that this design choice hindered the kinetics of particle-to-particle bridge formation, due to the formation of stable DNA loops on a single particle. One remedy to this may be to tweak the formulation of the particles so that the two DNA strands (*A* and *B*) on a particle are present in differing amounts. Then initially the *B* strand will be blocked so that the particle expresses only the *A* strand allowing for binding to the glass. Then, when the stripper strand unblocks the *B* strand, again loops will form, but the *B* strand

will be in excess, so now the stuck particles will express the *B* strand, allowing for binding with non-adhered but still ”blocked” particles. Then once bound, the particles will continue to equilibrate further stabilizing the aggregate.

Next, we reengineered this experimental platform to allow for particle rolling. This was done by using a DNA architecture that had a significantly lower DNA binding energy compared to the monolayer experiments, and thus shorter-lived particle-wall DNA bridges. The transience of the DNA bridges was critical for promoting particle rolling, as the DNA architecture used in the monolayer experiments was not conducive to this phenomenon. We were able to make two distinct DNA architectures promote particle rolling, one where the DNA overlap was in line with the particle to wall DNA bridge and the bridges were relatively strong, and the other where the overlap was orthogonal to the bridge and the bridges were relatively weak. We observed that these particles had significantly different rolling behavior, with the weaker DNA system rolling faster over a narrow range of low shear rates, while the stronger system rolled slower over a broader range of higher shear rates. Additionally, we noted that there was a high degree of not only particle-to-particle variation in rolling velocity, but also each individual particle took on a broad rolling velocity distribution.

We then constructed a Brownian adhesive dynamics model that included the particle to wall hydrodynamics, Brownian motion, and the DNA kinetics and thermodynamics in a stochastic manner. Then, using several free parameters, notably

the DNA density, energy of hybridization, and force sensitivity (reactive compliance), we fit the model to the experimental mean rolling velocity. Upon doing this fitting operation, we noted that the model was able to capture the experimental particle diffusivity and the individual particle rolling velocity distribution for plausible values of these parameters. Additionally, it captured the end behaviors, where particles stuck at very low shear rates and were not observed in the experiment at high shear rates, despite not explicitly being included in the fit. Then, using the model, we were able to propose potential mechanisms for the observed particle-to-particle variation in mean rolling velocity. Specifically, we were able to rule out the intrinsic variation in particle radius as being the sole contributor of this heterogeneity, and our results suggest that very slight differences in the surface to wall repulsive force, leading to nanometer level variations in mean distance from the wall, could account for this heterogeneity. This result may prove important for future cell experiments which have been modeled quite well in terms of the mean rolling velocity but have typically not investigated the observed cell-to-cell heterogeneity.

We also discussed some of the different methods used throughout this work to functionalize various surfaces with DNA, particularly gold nanoparticles, plastic microbeads, and glass. Due to the electrostatic charge of DNA, the solution ionic strength, amongst other factors, can be effectively used to control the packing density onto a given substrate. Additionally, using the results of DNA silica separation experiments and molecular dynamic simulations from literature, we help illuminate why

in general DNA microarrays on glass have a low percent of DNA availability, and possibly why throughout this thesis, particle non-specific binding was so difficult to eliminate repeatedly.

Finally, much of the technology we have used throughout this work have been repurposed from the field of DNA directed colloidal self-assembly, and we hope that some of the insights we made, particularly in the methods for functionalizing particles with DNA, will be of use to our lab's work in this field. We discussed the different classes of building blocks: spherical isotropic specific, nonspecific directional, specific directional, and Janu-directional. We surveyed a variety of different methods that have been used experimentally to create these classes of building blocks, ranging from DNA origamis and nanoparticle approaches up to crystal templated colloidal clusters, as well as some of the preliminary efforts to assemble these building blocks experimentally. However, as the simulations and theoretical models show, the experiments have barely scrapped the surface in terms of the possibilities, and this will be an exciting area to follow in the years to come.

8.2 Future Work

One of the most obvious avenues to expand upon this work is to continue with the cell-free clotting experiments, but this time including the temporally activated particle-to-particle interactions. Using confocal microscopy, the evolution of the three-dimensional structure of the aggregate could be imaged, and its structure analyzed.

Another extension would be to use platelets in a monolayer experiment and determine if they exhibit the same particle collision effect that we saw in our experiments. The Diamond lab (270) has used $\alpha_{IIb}\beta_3$ in microfluidic experiments to inhibit platelet to platelet aggregation, resulting in monolayer of platelets on collagen and tissue factor. Because platelets are non-spherical, deformable, and significantly larger than the particles used in our experiments, it is unclear if they would be impacted by the symmetry breaking in their flow fields around already adhered platelets.

It would also be interesting to alter the whole system to make it more biologically relevant, and it seems targeted drug delivery may be a potential application, particularly with liposomes. It would be interesting to see the behavior of DNA functionalized liposomes in our aggregation and rolling experiments. Additionally, (271) there have been studies done to functionalize liposomes with aptamers; short DNA strands with high affinity bind specific non-DNA targets. Some aptamer protein systems have been studied using dynamic force spectroscopy to measure the force sensitivity of these complexes, and they showed reactive compliances and binding energies not to different than those used in this thesis. These results seem to suggest that a rolling system could be developed using DNA aptamers and non-DNA ligands and proteins. In the case of liposomes, care would have to be taken to ensure the DNA was anchored strongly to the liposome and does not pull out under forces comparable to the force to cause unbinding.

There is the potential to develop more efficient DNA microarrays on glass through chemistries that lead to a high availability of DNA. As we discussed, there is an intrinsic affinity of the DNA to non-specifically bind to glass strongly. However, by

using high molecular weight mercapto-PEG-thiol groups, or layer-by-layer deposition, it seems possibly to overcome this drawback, and create a system with both high density and high availability of DNA.

BIBLIOGRAPHY

1. Palta, S., R. Saroa, and A. Palta. 2014. Overview of the coagulation system. Indian J Anaesth 58(5):515-523.

2. Muller, W. A. 2013. Getting leukocytes to the site of inflammation. Vet Pathol 50(1):7-22.

3. Olusanya, T. O. B., R. R. Haj Ahmad, D. M. Ibegbu, J. R. Smith, and A. A. Elkordy. 2018. Liposomal Drug Delivery Systems and Anticancer Drugs. Molecules (Basel, Switzerland) 23(4):907.

4. Bell, G. I. 1978. Models for the Specific Adhesion of Cells to Cells. Science 200(4342):618-627.

5. Evans, E., and K. Ritchie. 1997. Dynamic strength of molecular adhesion bonds. Biophysical Journal 72(4):1541-1555.

6. Evans, E. 2001. Probing the Relation Between Force—Lifetime—and Chemistry in Single Molecular Bonds. Annual Review of Biophysics and Biomolecular Structure 30(1):105-128.

7. Bell, G. I., M. Dembo, and P. Bongrand. 1984. Cell adhesion. Competition between nonspecific repulsion and specific bonding. Biophysical journal 45(6):1051-1064.

8. Dembo, M., D. C. Torney, K. Saxman, and D. Hammer. 1988. The Reaction-Limited Kinetics of Membrane-to-Surface Adhesion and Detachment. Proceedings of the Royal Society of London. Series B, Biological Sciences 234(1274):55-83.

9. Dembo, M. 1994. On peeling an adherent cell from a surface. Lectures on Mathematics in the Life Sciences, Some Mathematical Problems in Biology 26:51-77.

10. Hammer, D. A., and D. A. Lauffenburger. 1987. A dynamical model for receptor-mediated cell adhesion to surfaces. Biophysical Journal 52(3):475-487.

11. Forrester, J. V., and J. M. Lackie. 1984. Adhesion of neutrophil leucocytes under conditions of flow. Journal of Cell Science 70(1):93-110.

12. Hertz, C. M., D. J. Graves, D. A. Lauffenburger, and F. T. Serota. 1985. Use of cell affinity chromatography for separation of lymphocyte subpopulations. Biotechnology and bioengineering 27(5):603-612.

13. Brunk, D. K., and D. A. Hammer. 1997. Quantifying rolling adhesion with a cell-free assay: E-selectin and its carbohydrate ligands. Biophys J 72(6):2820-2833.

14. Zhang, Y., V. T. Milam, D. J. Graves, and D. A. Hammer. 2006. Differential adhesion of microspheres mediated by DNA hybridization I: experiment. Biophysical journal 90(11):4128-4136.

15. Zhang, Y., A. O. Eniola, D. J. Graves, and D. A. Hammer. 2003. Specific Adhesion of Micron-Sized Colloids to Surfaces Mediated by Hybridizing DNA Chains. Langmuir 19(17):6905-6911.

16. Hammer, D. A., and S. M. Apte. 1992. Simulation of cell rolling and adhesion on surfaces in shear flow: general results and analysis of selectin-mediated neutrophil adhesion. Biophysical journal 63(1):35-57.

17. Dasanna, A. K., C. Lansche, M. Lanzer, and U. S. Schwarz. 2017. Rolling Adhesion of Schizont Stage Malaria-Infected Red Blood Cells in Shear Flow. Biophysical Journal 112(9):1908-1919.

18. Dasanna, A. K., and U. S. Schwarz. 2018. Adhesion-based sorting of blood cells: an adhesive dynamics simulation study. Soft Matter 14(44):9061-9070. 10.1039/C8SM01524D.

19. English, T. J., and D. A. Hammer. 2004. Brownian adhesive dynamics (BRAD) for simulating the receptor-mediated binding of viruses. Biophysical journal 86(6):3359-3372.

20. Chang, K. C., and D. A. Hammer. 2000. Adhesive dynamics simulations of sialyl-Lewis(x)/E-selectin-mediated rolling in a cell-free system. Biophys J 79(4):1891-1902.

21. Brenner, H. 1961. The slow motion of a sphere through a viscous fluid towards a plane surface. Chemical Engineering Science 16(3):242-251.

22. Goldman, A. J., R. G. Cox, and H. Brenner. 1967. Slow viscous motion of a sphere parallel to a plane wall—I Motion through a quiescent fluid. Chemical Engineering Science 22(4):637-651.

23. Goldman, A. J., R. G. Cox, and H. Brenner. 1967. Slow viscous motion of a sphere parallel to a plane wall—II Couette flow. Chemical Engineering Science 22(4):653-660.

24. De Corato, M., F. Greco, G. D'Avino, and P. L. Maffettone. 2015. Hydrodynamics and Brownian motions of a spheroid near a rigid wall. J. Chem. Phys. 142(19):14. Article.

25. DePamphilis, M. L. 2000. Review: Nuclear Structure and DNA Replication. Journal of Structural Biology 129(2):186-197.

26. Travers, A., and G. Muskhelishvili. 2015. DNA structure and function. The FEBS Journal 282(12):2279-2295.

27. Watson, J. D., and F. H. C. Crick. 1953. Molecular Structure of Nucleic Acids: A Structure for Deoxyribose Nucleic Acid. Nature 171(4356):737-738.

28. SantaLucia, J., H. T. Allawi, and P. A. Seneviratne. 1996. Improved Nearest-Neighbor Parameters for Predicting DNA Duplex Stability†. Biochemistry 35(11):3555-3562.

29. Peyret, N., P. A. Seneviratne, H. T. Allawi, and J. SantaLucia. 1999. Nearest-neighbor thermodynamics and NMR of DNA sequences with internal A center dot A, C center dot C, G center dot G, and T center dot T mismatches. Biochemistry 38(12):3468-3477.

30. SantaLucia, J., Jr., and D. Hicks. 2004. The thermodynamics of DNA structural motifs. Annu Rev Biophys Biomol Struct 33(1):415-440.

31. SantaLucia, J., Jr. 1998. A unified view of polymer, dumbbell, and oligonucleotide DNA nearest-neighbor thermodynamics. Proc Natl Acad Sci U S A 95(4):1460-1465.

32. Chandrasekaran, A. R., and O. Levchenko. 2016. DNA Nanocages. Chemistry of Materials 28(16):5569-5581.

33. Torring, T., N. V. Voigt, J. Nangreave, H. Yan, and K. V. Gothelf. 2011. DNA origami: a quantum leap for self-assembly of complex structures. Chem Soc Rev 40(12):5636-5646.

34. Zhang, J. X., J. Z. Fang, W. Duan, L. R. Wu, A. W. Zhang, N. Dalchau, B. Yordanov, R. Petersen, A. Phillips, and D. Y. Zhang. 2017. Predicting DNA hybridization kinetics from sequence. Nature Chemistry 10:91. Article.

35. Rogers, W. B., T. Sinno, and J. C. Crocker. 2013. Kinetics and non-exponential binding of DNA-coated colloids. Soft Matter 9(28):6412-6417.

36. Tinland, B., A. Pluen, J. Sturm, and G. Weill. 1997. Persistence Length of Single-Stranded DNA. Macromolecules 30(19):5763-5765.

37. Smith, S. B., Y. Cui, and C. Bustamante. 1996. Overstretching B-DNA: the elastic response of individual double-stranded and single-stranded DNA molecules. Science 271(5250):795-799.

38. Bustamante, C., S. B. Smith, J. Liphardt, and D. Smith. 2000. Single-molecule studies of DNA mechanics. Current Opinion in Structural Biology 10(3):279-285.

39. Wang, M. D., H. Yin, R. Landick, J. Gelles, and S. M. Block. 1997. Stretching DNA with optical tweezers. Biophysical Journal 72(3):1335-1346.

40. Konrad, M. W., and J. I. Bolonick. 1996. Molecular dynamics simulation of DNA stretching is consistent with the tension observed for extension and strand separation and predicts a novel ladder structure. Journal of the American Chemical Society 118(45):10989-10994. Article.

41. Bensimon, D., A. J. Simon, V. Croquette, and A. Bensimon. 1995. Stretching DNA with a receding meniscus: Experiments and models. Phys. Rev. Lett. 74(23):4754-4757. Article.

42. Lee, G. U., L. A. Chrisey, and R. J. Colton. 1994. Direct measurement of the forces between complementary strands of DNA. Science 266(5186):771-773. Article.

43. Bercy, M., and U. Bockelmann. 2015. Hairpins under tension: RNA versus DNA. Nucleic acids research 43(20):9928-9936.

44. Strunz, T., K. Oroszlan, R. Schäfer, and H.-J. Güntherodt. 1999. Dynamic force spectroscopy of single DNA molecules. Proceedings of the National Academy of Sciences 96(20):11277-11282.

45. Neher, R. A., and U. Gerland. 2004. Dynamics of Force-Induced DNA Slippage. Phys. Rev. Lett. 93(19):198102.

46. Kühner, F., J. Morfill, R. A. Neher, K. Blank, and H. E. Gaub. 2007. Force-Induced DNA Slippage. Biophysical Journal 92(7):2491-2497.

47. Pope, L. H., M. C. Davies, C. A. Laughton, C. J. Roberts, S. J. Tendler, and P. M. Williams. 2001. Force-induced melting of a short DNA double helix. European biophysics journal : EBJ 30(1):53-62.

48. Whitesides, G. M. 2006. The origins and the future of microfluidics. Nature 442(7101):368-373.

49. David J. Beebe, a. Glennys A. Mensing, and G. M. Walker. 2002. Physics and Applications of Microfluidics in Biology. Annual Review of Biomedical Engineering 4(1):261-286.

50. Convery, N., and N. Gadegaard. 2019. 30 years of microfluidics. Micro and Nano Engineering 2:76-91.

51. Shi, B., Y. K. Shin, A. A. Hassanali, and S. J. Singer. 2015. DNA Binding to the Silica Surface. The Journal of Physical Chemistry B 119(34):11030-11040.

52. Chen, V., A. Fane, S. Madaeni, and I. Wenten. 1997. Particle deposition during membrane filtration of colloids: transition between concentration polarization and cake formation. Journal of Membrane Science 125(1):109-122.

53. Wyss, H. M., D. L. Blair, J. F. Morris, H. A. Stone, and D. A. Weitz. 2006. Mechanism for clogging of microchannels. Physical review E 74(6):061402.

54. Riley, D. J., and R. G. Carbonell. 1993. Mechanisms of particle deposition from ultrapure chemicals onto semiconductor wafers: Deposition from bulk liquid during wafer submersion. Journal of colloid and interface science 158(2):259-273.

55. Bryers, J. D. 1987. Biologically active surfaces: processes governing the formation and persistence of biofilms. Biotechnology Progress 3(2):57-68.

56. Vrijenhoek, E. M., S. Hong, and M. Elimelech. 2001. Influence of membrane surface properties on initial rate of colloidal fouling of reverse osmosis and nanofiltration membranes. Journal of membrane science 188(1):115-128.

57. Harding, J. L., and M. M. Reynolds. 2014. Combating medical device fouling. Trends in biotechnology 32(3):140-146.

58. Mustin, B., and B. Stoeber. 2010. Deposition of particles from polydisperse suspensions in microfluidic systems. Microfluidics and nanofluidics 9(4-5):905-913.

59. Flamm, M. H., T. V. Colace, M. S. Chatterjee, H. Jing, S. Zhou, D. Jaeger, L. F. Brass, T. Sinno, and S. L. Diamond. 2012. Multiscale prediction of patient-specific platelet function under flow. Blood 120(1):190-198.

60. Zhu, S., Y. Lu, T. Sinno, and S. L. Diamond. 2016. Dynamics of thrombin generation and flux from clots during whole human blood flow over collagen/tissue factor surfaces. Journal of Biological Chemistry 291(44):23027-23035.

61. Unni, H., and C. Yang. 2005. Brownian dynamics simulation and experimental study of colloidal particle deposition in a microchannel flow. Journal of colloid and interface science 291(1):28-36.

62. Muangnapoh, T., A. L. Weldon, and J. F. Gilchrist. 2013. Enhanced colloidal monolayer assembly via vibration-assisted convective deposition. Applied Physics Letters 103(18):181603.

63. Russel, W. B., D. A. Saville, and W. R. Schowalter. 1989. Colloidal dispersions. Cambridge university press.

64. Elimelech, M., J. Gregory, and X. Jia. 2013. Particle deposition and aggregation: measurement, modelling and simulation. Butterworth-Heinemann.

65. Sriram, I., and E. M. Furst. 2015. Two spheres translating in tandem through a colloidal suspension. Physical Review E 91(4):042303.

66. Xu, B., and J. F. Gilchrist. 2014. Microstructure of sheared monosized colloidal suspensions resulting from hydrodynamic and electrostatic interactions. The Journal of chemical physics 140(20):204903.

67. Unni, H., and C. Yang. 2007. Kinetics of colloidal particle deposition to a solid surface from pressure driven microchannel flows. The Canadian Journal of Chemical Engineering 85(5):609-616.

68. Adamczyk, Z., M. Zembala, B. Siwek, and J. Czarnecki. 1986. Kinetics of latex particle deposition from flowing suspensions. Journal of colloid and interface science 110(1):188-200.

69. Dabroś, T., and Z. Adamczyk. 1979. Noninertial particle transfer to the rotating disc under an external force field (laminar flow). Chemical Engineering Science 34(8):1041-1049.

70. Prieve, D. C., and M. M. Lin. 1980. Adsorption of Brownian hydrosols onto a rotating disc aided by a uniform applied force. Journal of Colloid and Interface Science 76(1):32-47.

71. Colace, T. V., G. W. Tormoen, O. J. McCarty, and S. L. Diamond. 2013. Microfluidics and coagulation biology. Annual review of biomedical engineering 15:283-303.

72. Muthard, R. W., and S. L. Diamond. 2013. Side view thrombosis microfluidic device with controllable wall shear rate and transthrombus pressure gradient. Lab on a Chip 13(10):1883-1891.

73. Lu, Y., M. Y. Lee, S. Zhu, T. Sinno, and S. L. Diamond. 2016. Multiscale simulation of thrombus growth and vessel occlusion triggered by collagen/tissue factor using a data-driven model of combinatorial platelet signalling. Mathematical Medicine and Biology: A Journal of the IMA 34(4):523-546.

74. Vahidkhah, K., S. L. Diamond, and P. Bagchi. 2014. Platelet dynamics in three-dimensional simulation of whole blood. Biophysical journal 106(11):2529-2540.

75. Fogelson, A. L., and K. B. Neeves. 2015. Fluid mechanics of blood clot formation. Annual review of fluid mechanics 47:377-403.

76. Kim, A. J., V. N. Manoharan, and J. C. Crocker. 2005. Swelling-based method for preparing stable, functionalized polymer colloids. Journal of the American Chemical Society 127(6):1592-1593.

77. Li, D., S. Banon, and S. L. Biswal. 2010. Bending dynamics of DNA-linked colloidal particle chains. Soft Matter 6(17):4197-4204.

78. Wang, Y., Y. Wang, X. Zheng, É. Ducrot, J. S. Yodh, M. Weck, and D. J. Pine. 2015. Crystallization of DNA-coated colloids. Nature communications 6:7253.

79. Schlauch, E., M. Ernst, R. Seto, H. Briesen, M. Sommerfeld, and M. Behr. 2013. Comparison of three simulation methods for colloidal aggregates in Stokes flow: Finite elements, lattice Boltzmann and Stokesian dynamics. Computers & Fluids 86:199-209.

80. Bolintineanu, D. S., G. S. Grest, J. B. Lechman, F. Pierce, S. J. Plimpton, and P. R. Schunk. 2014. Particle dynamics modeling methods for colloid suspensions. Computational Particle Mechanics 1(3):321-356.

81. Mittal, R., and G. Iaccarino. 2005. Immersed boundary methods. Annu. Rev. Fluid Mech. 37:239-261.

82. Hou, G., J. Wang, and A. Layton. 2012. Numerical methods for fluid-structure interaction—a review. Communications in Computational Physics 12(2):337-377.

83. Jung, S. Y., Y.-J. Won, J. H. Jang, J. H. Yoo, K. H. Ahn, and C.-H. Lee. 2015. Particle deposition on the patterned membrane surface: Simulation and experiments. Desalination 370:17-24.

84. Yurke, B., and A. P. Mills. 2003. Using DNA to Power Nanostructures. Genetic Programming and Evolvable Machines 4(2):111-122. journal article.

85. Rogers, W. B., and J. C. Crocker. 2011. Direct measurements of DNA-mediated colloidal interactions and their quantitative modeling. Proceedings of the National Academy of Sciences 108(38):15687-15692.

86. Evangelidis, G. 2013. IAT: A Matlab toolbox for image alignment.

87. Pelletier, V., N. Gal, P. Fournier, and M. L. Kilfoil. 2009. Microrheology of microtubule solutions and actin-microtubule composite networks. Physical review letters 102(18):188303.

88. Crocker, J. C., and D. G. Grier. 1996. Methods of digital video microscopy for colloidal studies. Journal of colloid and interface science 179(1):298-310.

89. Ermak, D. L., and J. McCammon. 1978. Brownian dynamics with hydrodynamic interactions. The Journal of chemical physics 69(4):1352-1360.

90. Rubinstein, R. Y., and D. P. Kroese. 2016. Simulation and the Monte Carlo method. John Wiley & Sons.

91. Biancaniello, P. L., A. J. Kim, and J. C. Crocker. 2005. Colloidal interactions and self-assembly using DNA hybridization. Phys. Rev. Lett. 94(5):058302.

92. Kim, A. J., R. Scarlett, P. L. Biancaniello, T. Sinno, and J. C. Crocker. 2009. Probing interfacial equilibration in microsphere crystals formed by DNA-directed assembly. Nature materials 8(1):52.

93. Scarlett, R. T., J. C. Crocker, and T. Sinno. 2010. Computational analysis of binary segregation during colloidal crystallization with DNA-mediated interactions. The Journal of chemical physics 132(23):234705.

94. Scarlett, R. T., M. T. Ung, J. C. Crocker, and T. Sinno. 2011. A mechanistic view of binary colloidal superlattice formation using DNA-directed interactions. Soft Matter 7(5):1912-1925.

95. Jenkins, I. C., M. T. Casey, J. T. McGinley, J. C. Crocker, and T. Sinno. 2014. Hydrodynamics selects the pathway for displacive transformations in DNA-linked colloidal crystallites. Proceedings of the National Academy of Sciences 111(13):4803-4808.

96. Bevan, M. A., and D. C. Prieve. 1999. Direct Measurement of Retarded van der Waals Attraction. Langmuir 15(23):7925-7936.

97. Assemi, S., J. Nalaskowski, and W. P. Johnson. 2006. Direct force measurements between carboxylate-modified latex microspheres and glass using atomic force microscopy. Colloids and Surfaces A: Physicochemical and Engineering Aspects 286(1):70-77.

98. Kim, K., Y. Nakayama, and R. Yamamoto. 2006. Direct numerical simulations of electrophoresis of charged colloids. Physical review letters 96(20):208302.

99. Nakayama, Y., and R. Yamamoto. 2005. Simulation method to resolve hydrodynamic interactions in colloidal dispersions. Physical Review E 71(3):036707.

100. Lee, Y. K., J. Nam, K. Hyun, K. H. Ahn, and S. J. Lee. 2015. Rheology and microstructure of non-Brownian suspensions in the liquid and crystal coexistence region: strain stiffening in large amplitude oscillatory shear. Soft matter 11(20):4061-4074.

101. Sholl, D. S., M. K. Fenwick, E. Atman, and D. C. Prieve. 2000. Brownian dynamics simulation of the motion of a rigid sphere in a viscous fluid very near a wall. The Journal of Chemical Physics 113(20):9268-9278.

102. Malevanets, A., and R. Kapral. 1999. Mesoscopic model for solvent dynamics. The Journal of chemical physics 110(17):8605-8613.

103. Ripoll, M., K. Mussawisade, R. Winkler, and G. Gompper. 2005. Dynamic regimes of fluids simulated by multiparticle-collision dynamics. Physical Review E 72(1):016701.

104. Ladd, A., and R. Verberg. 2001. Lattice-Boltzmann simulations of particle-fluid suspensions. Journal of Statistical Physics 104(5-6):1191-1251.

105. Dunn, P. F., and M. P. Davis. 2017. Measurement and data analysis for engineering and science. CRC press.

106. Roma, A. M., C. S. Peskin, and M. J. Berger. 1999. An adaptive version of the immersed boundary method. Journal of computational physics 153(2):509-534.

107. Peskin, C. S. 2002. The immersed boundary method. Acta numerica 11:479-517.

108. Nguyen, N.-Q., and A. Ladd. 2002. Lubrication corrections for lattice-Boltzmann simulations of particle suspensions. Physical Review E 66(4):046708.

109. Qian, Y., D. d'Humières, and P. Lallemand. 1992. Lattice BGK models for Navier-Stokes equation. EPL (Europhysics Letters) 17(6):479.

110. Zou, Q., and X. He. 1997. On pressure and velocity boundary conditions for the lattice Boltzmann BGK model. Physics of fluids 9(6):1591-1598.

111. Succi, S. 2001. The lattice Boltzmann equation: for fluid dynamics and beyond. Oxford university press.

112. Aidun, C. K., and J. R. Clausen. 2010. Lattice-Boltzmann method for complex flows. Annual review of fluid mechanics 42:439-472.

113. Goren, S. L., and M. E. O'Neill. 1971. On the hydrodynamic resistance to a particle of a dilute suspension when in the neighbourhood of a large obstacle. Chemical Engineering Science 26(3):325-338.

114. Zadeh, J. N., C. D. Steenberg, J. S. Bois, B. R. Wolfe, M. B. Pierce, A. R. Khan, R. M. Dirks, and N. A. Pierce. 2011. NUPACK: Analysis and design of nucleic acid systems. Journal of computational chemistry 32(1):170-173.

115. Srinivas, N., T. E. Ouldridge, P. Sulc, J. M. Schaeffer, B. Yurke, A. A. Louis, J. P. K. Doye, and E. Winfree. 2013. On the biophysics and kinetics of toehold-mediated DNA strand displacement. Nucleic acids research 41(22):10641-10658.

116. Oh, J. S., Y. F. Wang, D. J. Pine, and G. R. Yi. 2015. High-Density PEO-b-DNA Brushes on Polymer Particles for Colloidal Superstructures. Chemistry of Materials 27(24):8337-8344.

117. Mody, N. A., and M. R. King. 2007. Influence of Brownian Motion on Blood Platelet Flow Behavior and Adhesive Dynamics near a Planar Wall. Langmuir 23(11):6321-6328.

118. Chang, K. C., and D. A. Hammer. 2000. Adhesive dynamics simulations of sialyl-Lewis(x)/E-selectin-mediated rolling in a cell-free system. Biophysical journal 79(4):1891-1902.

119. King, M. R., and D. A. Hammer. 2001. Multiparticle adhesive dynamics. Interactions between stably rolling cells. Biophysical journal 81(2):799-813.

120. Tees, D. F. J., K.-C. Chang, S. D. Rodgers, and D. A. Hammer. 2002. Simulation of Cell Adhesion to Bioreactive Surfaces in Shear: The Effect of Cell Size. Industrial & Engineering Chemistry Research 41(3):486-493.

121. Hammer, D. A. 2014. Adhesive Dynamics. Journal of Biomechanical Engineering 136(2):0210061-02100610.

122. Porter, C. L., and J. C. Crocker. 2017. Directed assembly of particles using directional DNA interactions. Current Opinion in Colloid and Interface Science 30:34-44. Review.

123. Crocker, J. C. 2008. Nanomaterials: Golden handshake. Nature 451(7178):528-529.

124. Cademartiri, L., and K. J. M. Bishop. 2015. Programmable self-assembly. Nat. Mater. 14(1):2-9. Article.

125. Rogers, W. B., W. M. Shih, and V. N. Manoharan. 2016. Using DNA to program the self-assembly of colloidal nanoparticles and microparticles. Nat. Rev. Mater. 1(3):14. Review.

126. Heller, M. J. 2002. DNA Microarray Technology: Devices, Systems, and Applications. Annual Review of Biomedical Engineering 4(1):129-153.

127. Bumgarner, R. 2013. Overview of DNA microarrays: types, applications, and their future. Current protocols in molecular biology 101(1):22.21. 21-22.21. 11.

128. Zhang, Y., B. S. Lai, and M. Juhas. 2019. Recent Advances in Aptamer Discovery and Applications. Molecules 24(5):941.

129. Hu, Q., H. Li, L. Wang, H. Gu, and C. Fan. 2019. DNA Nanotechnology-Enabled Drug Delivery Systems. Chem Rev 119(10):6459-6506.

130. Rogers, W. B., and J. C. Crocker. 2011. Direct measurements of DNA-mediated colloidal interactions and their quantitative modeling. Proc. Natl. Acad. Sci. U. S. A. 108(38):15687-15692.

131. Lee, Y. K., C. Porter, S. L. Diamond, J. C. Crocker, and T. Sinno. 2018. Deposition of sticky spheres in channel flow: Modeling of surface coverage evolution requires accurate sphere-sphere collision hydrodynamics. Journal of Colloid and Interface Science 530:383-393. Article.

132. Rogers, Y. H., P. Jiang-Baucom, Z. J. Huang, V. Bogdanov, S. Anderson, and M. T. Boyce-Jacino. 1999. Immobilization of oligonucleotides onto a glass support via disulfide bonds: A method for preparation of DNA microarrays. Anal Biochem 266(1):23-30.

133. Chang, K. C., and D. A. Hammer. 1996. Influence of direction and type of applied force on the detachment of macromolecularly-bound particles from surfaces. Langmuir 12(9):2271-2282. Article.

134. Murphy, M. C., I. Rasnik, W. Cheng, T. M. Lohman, and T. Ha. 2004. Probing single-stranded DNA conformational flexibility using fluorescence spectroscopy. Biophys J 86(4):2530-2537.

135. Haynes, W. 2016. CRC Handbook of Chemistry and Physics, revise ed. CRC Press, Boca Raton, Florida.

136. Saleh, O. A., D. B. McIntosh, P. Pincus, and N. Ribeck. 2009. Nonlinear Low-Force Elasticity of Single-Stranded DNA Molecules. Phys. Rev. Lett. 102(6):068301.

137. Petrosyan, R. 2017. Improved approximations for some polymer extension models. Rheologica Acta 56(1):21-26. journal article.

138. Kazoe, Y., and M. Yoda. 2011. Measurements of the near-wall hindered diffusion of colloidal particles in the presence of an electric field. Appl Phys Lett 99(12):124104.

139. Assemi, S., J. Nalaskowski, and W. P. Johnson. 2006. Direct force measurements between carboxylate-modified latex microspheres and glass using atomic force microscopy. Colloid Surface A 286(1-3):70-77.

140. McGinley, J. T., Y. Wang, I. C. Jenkins, T. Sinno, and J. C. Crocker. 2015. Crystal-Templated Colloidal Clusters Exhibit Directional DNA Interactions. ACS Nano 9(11):10817-10825.

141. Wang, Y., Y. Wang, X. Zheng, E. Ducrot, J. S. Yodh, M. Weck, and D. J. Pine. 2015. Crystallization of DNA-coated colloids. Nat Commun 6:7253.

142. Feng, L., R. Dreyfus, R. Sha, N. C. Seeman, and P. M. Chaikin. 2013. DNA patchy particles. Adv Mater 25(20):2779-2783.

143. Kim, A. J., V. N. Manoharan, and J. C. Crocker. 2005. Swelling-based method for preparing stable, functionalized polymer colloids. J Am Chem Soc 127(6):1592-1593.

144. Nie, Z. H., A. Petukhova, and E. Kumacheva. 2010. Properties and emerging applications of self-assembled structures made from inorganic nanoparticles. Nature Nanotechnology 5(1):15-25.

145. Mishra, Y. K., N. A. Murugan, J. Kotakoski, and J. Adam. 2017. Progress in electronics and photonics with nanomaterials. Vacuum 146:304-307.

146. Mirkin, C. A., R. L. Letsinger, R. C. Mucic, and J. J. Storhoff. 1996. A DNA-based method for rationally assembling nanoparticles into macroscopic materials. Nature 382(6592):607-609.

147. Mirkin, C. A. 2000. Programming the assembly of two- and three-dimensional architectures with DNA and nanoscale inorganic building blocks. Inorg Chem 39(11):2258-2272.

148. Park, S. Y., A. K. Lytton-Jean, B. Lee, S. Weigand, G. C. Schatz, and C. A. Mirkin. 2008. DNA-programmable nanoparticle crystallization. Nature 451(7178):553-556.

149. Kim, A. J., P. L. Biancaniello, and J. C. Crocker. 2006. Engineering DNA-mediated colloidal crystallization. Langmuir 22(5):1991-2001.

150. Wu, K.-T., L. Feng, R. Sha, R. Dreyfus, A. Y. Grosberg, N. C. Seeman, and P. M. Chaikin. 2013. Kinetics of DNA-coated sticky particles. Physical Review E 88(2):022304.

151. Hurst, S. J., A. K. R. Lytton-Jean, and C. A. Mirkin. 2006. Maximizing DNA Loading on a Range of Gold Nanoparticle Sizes. Analytical Chemistry 78(24):8313-8318.

152. Zhang, Y., S. Pal, B. Srinivasan, T. Vo, S. Kumar, and O. Gang. 2015. Selective transformations between nanoparticle superlattices via the reprogramming of DNA-mediated interactions. Nat. Mater. 14(8):840.

153. Kim, Y., R. J. Macfarlane, M. R. Jones, and C. A. Mirkin. 2016. Transmutable nanoparticles with reconfigurable surface ligands. Science 351(6273):579-582.

154. Shim, T. S., Z. G. Estephan, Z. Qian, J. H. Prosser, S. Y. Lee, D. M. Chenoweth, D. Lee, S.-J. Park, and J. C. Crocker. 2017. Shape changing thin films powered by DNA hybridization. Nature Nanotechnology 12(1):41-47.

155. Xue, Y., X. Li, H. Li, and W. Zhang. 2014. Quantifying thiol–gold interactions towards the efficient strength control. Nature Communications 5(1):4348.

156. DeRisi, J., L. Penland, P. O. Brown, M. L. Bittner, P. S. Meltzer, M. Ray, Y. Chen, Y. A. Su, and J. M. Trent. 1996. Use of a cDNA microarray to analyse gene expression patterns in human cancer. Nat Genet 14(4):457-460.

157. Nimse, S. B., K. Song, M. D. Sonawane, D. R. Sayyed, and T. Kim. 2014. Immobilization Techniques for Microarray: Challenges and Applications. Sensors 14(12):22208-22229. Review.

158. Valtiner, M., X. Banquy, K. Kristiansen, G. W. Greene, and J. N. Israelachvili. 2012. The Electrochemical Surface Forces Apparatus: The Effect of Surface Roughness, Electrostatic Surface Potentials, and Anodic Oxide Growth on Interaction Forces, and Friction between Dissimilar Surfaces in Aqueous Solutions. Langmuir 28(36):13080-13093.

159. Chen, W.-H., Y.-T. Tseng, S. Hsieh, W.-C. Liu, C.-W. Hsieh, C.-W. Wu, C.-H. Huang, H.-Y. Lin, C.-W. Chen, P.-Y. Lin, and L.-K. Chau. 2014. Silanization of solid surfaces via mercaptopropylsilatrane: a new approach of constructing gold colloid monolayers. RSC Adv. 4(87):46527-46535.

160. Karp, A., P. G. Isaac, and D. S. Ingram. 1998. Isolation of nucleic acids using silica-gel based membranes: methods based on the use of QIAamp spin columns. Molecular Tools for Screening Biodiversity. Springer, pp. 59-63.

161. Liu, L., Z. Guo, Z. Huang, J. Zhuang, and W. Yang. 2016. Size-selective separation of DNA fragments by using lysine-functionalized silica particles. Scientific Reports 6(1):22029.

162. Vandeventer, P. E., J. S. Lin, T. J. Zwang, A. Nadim, M. S. Johal, and A. Niemz. 2012. Multiphasic DNA adsorption to silica surfaces under varying buffer, pH, and ionic strength conditions. J Phys Chem B 116(19):5661-5670.

163. Vandeventer, P. E., J. Mejia, A. Nadim, M. S. Johal, and A. Niemz. 2013. DNA adsorption to and elution from silica surfaces: influence of amino acid buffers. J Phys Chem B 117(37):10742-10749.

164. Wu, J., H. Wang, A. Zhu, and F. Long. 2018. Adsorption Kinetics of Single-Stranded DNA on Functional Silica Surfaces and Its Influence Factors: An Evanescent-Wave Biosensor Study. ACS Omega 3(5):5605-5614.

165. Kang, S. H., M. R. Shortreed, and E. S. Yeung. 2001. Real-Time Dynamics of Single-DNA Molecules Undergoing Adsorption and Desorption at Liquid−Solid Interfaces. Analytical Chemistry 73(6):1091-1099.

166. Isailovic, S., H.-W. Li, and E. S. Yeung. 2007. Adsorption of single DNA molecules at the water/fused-silica interface. Journal of Chromatography A 1150(1):259-266.

167. Michel, M., V. Toniazzo, D. Ruch, and V. Ball. 2012. Deposition mechanisms in layer-by-layer or step-by-step deposition methods: From elastic and impermeable films to soft membranes with ion exchange properties. ISRN Materials Science 2012.

168. Nguyen, N.-T. 2012. Chapter 4 - Fabrication technologies. Micromixers (Second Edition). N.-T. Nguyen, editor. William Andrew Publishing, Oxford, pp. 113-161.

169. Jones, M. R., N. C. Seeman, and C. A. Mirkin. 2015. Nanomaterials. Programmable materials and the nature of the DNA bond. Science 347(6224):1260901.

170. Alivisatos, A. P., K. P. Johnsson, X. G. Peng, T. E. Wilson, C. J. Loweth, M. P. Bruchez, and P. G. Schultz. 1996. Organization of 'nanocrystal molecules' using DNA. Nature 382(6592):609-611.

171. Leunissen, M. E., C. G. Christova, A. P. Hynninen, C. P. Royall, A. I. Campbell, A. Imhof, M. Dijkstra, R. van Roij, and A. van Blaaderen. 2005. Ionic colloidal crystals of oppositely charged particles. Nature 437(7056):235-240.

172. Hynninen, A. P., M. E. Leunissen, A. van Blaaderen, and M. Dijkstra. 2006. CuAu structure in the restricted primitive model and oppositely charged colloids. Phys. Rev. Lett. 96(1):-.

173. Nykypanchuk, D., M. M. Maye, D. van der Lelie, and O. Gang. 2008. DNA-guided crystallization of colloidal nanoparticles. Nature 451(7178):549-552.

174. Macfarlane, R. J., B. Lee, M. R. Jones, N. Harris, G. C. Schatz, and C. A. Mirkin. 2011. Nanoparticle superlattice engineering with DNA. Science 334(6053):204-208.

175. Casey, M. T., R. T. Scarlett, W. B. Rogers, I. Jenkins, T. Sinno, and J. C. Crocker. 2012. Driving diffusionless transformations in colloidal crystals using DNA handshaking. Nature Communications 3:1209.

176. Song, M., Y. Ding, H. Zerze, M. A. Snyder, and J. Mittal. 2017. Binary superlattice design by controlling DNA-mediated interactions. arXiv preprint arXiv:1703.03465.

177. Rogers, W. B., and V. N. Manoharan. 2015. Programming colloidal phase transitions with DNA strand displacement. Science 347(6222):639-642.

178. Wang, Y. F., I. C. Jenkins, J. T. McGinley, T. Sinno, and J. C. Crocker. 2017. Colloidal crystals with diamond symmetry at optical lengthscales. Nature Communications 8.

179. Glotzer, S. C., and M. J. Solomon. 2007. Anisotropy of building blocks and their assembly into complex structures. Nat Mater 6(8):557-562.

180. Murray, C. B., C. R. Kagan, and M. G. Bawendi. 1995. Self-Organization of Cdse Nanocrystallites into 3-Dimensional Quantum-Dot Superlattices. Science 270(5240):1335-1338.

181. Shevchenko, E. V., D. V. Talapin, N. A. Kotov, S. O'Brien, and C. B. Murray. 2006. Structural diversity in binary nanoparticle superlattices. Nature 439(7072):55-59.

182. Tang, Z., Y. Wang, S. Shanbhag, M. Giersig, and N. A. Kotov. 2006. Spontaneous transformation of CdTe nanoparticles into angled Te nanocrystals: from particles and rods to checkmarks, X-marks, and other unusual shapes. J Am Chem Soc 128(20):6730-6736.

183. Rossi, L., S. Sacanna, W. T. M. Irvine, P. M. Chaikin, D. J. Pine, and A. P. Philipse. 2011. Cubic crystals from cubic colloids. Soft Matter 7(9):4139-4142.

184. Damasceno, P. F., M. Engel, and S. C. Glotzer. 2012. Predictive self-assembly of polyhedra into complex structures. Science 337(6093):453-457.

185. van Anders, G., N. K. Ahmed, R. Smith, M. Engel, and S. C. Glotzer. 2014. Entropically patchy particles: engineering valence through shape entropy. ACS Nano 8(1):931-940.

186. Wang, Y., Y. Wang, D. R. Breed, V. N. Manoharan, L. Feng, A. D. Hollingsworth, M. Weck, and D. J. Pine. 2012. Colloids with valence and specific directional bonding. Nature 491(7422):51-55.

187. McGinley, J. T., I. Jenkins, T. Sinno, and J. C. Crocker. 2013. Assembling colloidal clusters using crystalline templates and reprogrammable DNA interactions. Soft Matter 9(38):9119-9128. 10.1039/C3SM50950H.

188. Ducrot, É., M. He, G.-R. Yi, and D. J. Pine. 2017. Colloidal alloys with preassembled clusters and spheres. Nat. Mater.

189. Tian, Y., T. Wang, W. Liu, H. L. Xin, H. Li, Y. Ke, W. M. Shih, and O. Gang. 2015. Prescribed nanoparticle cluster architectures and low-dimensional arrays built using octahedral DNA origami frames. Nature nanotechnology 10(7):637-644.

190. Tian, Y., Y. Zhang, T. Wang, H. L. Xin, H. Li, and O. Gang. 2016. Lattice engineering through nanoparticle-DNA frameworks. Nat. Mater. 15(6):654-661.

191. Liu, W., M. Tagawa, H. L. Xin, T. Wang, H. Emamy, H. Li, K. G. Yager, F. W. Starr, A. V. Tkachenko, and O. Gang. 2016. Diamond family of nanoparticle superlattices. Science 351(6273):582-586.

192. Mladek, B. M., J. Fornleitner, F. J. Martinez-Veracoechea, A. Dawid, and D. Frenkel. 2012. Quantitative prediction of the phase diagram of DNA-functionalized nanosized colloids. Phys Rev Lett 108(26):268301.

193. Leunissen, M. E., and D. Frenkel. 2011. Numerical study of DNA-functionalized microparticles and nanoparticles: explicit pair potentials and their implications for phase behavior. J Chem Phys 134(8):084702.

194. Grunwald, M., and P. L. Geissler. 2014. Patterns without patches: hierarchical self-assembly of complex structures from simple building blocks. ACS Nano 8(6):5891-5897. Article.

195. Zanjani, M. B., I. C. Jenkins, J. C. Crocker, and T. Sinno. 2016. Colloidal Cluster Assembly into Ordered Superstructures via Engineered Directional Binding. ACS nano.

196. Phillips, C. L., E. Jankowski, M. Marval, and S. C. Glotzer. 2012. Self-assembled clusters of spheres related to spherical codes. Phys. Rev. E 86(4 Pt 1):041124.

197. Schade, N. B., M. C. Holmes-Cerfon, E. R. Chen, D. Aronzon, J. W. Collins, J. A. Fan, F. Capasso, and V. N. Manoharan. 2013. Tetrahedral Colloidal Clusters from Random Parking of Bidisperse Spheres. Phys. Rev. Lett. 110(14).

198. Angioletti-Uberti, S., P. Varilly, B. M. Mognetti, and D. Frenkel. 2014. Mobile linkers on DNA-coated colloids: valency without patches. Phys Rev Lett 113(12):128303. Article.

199. Feng, L., L. L. Pontani, R. Dreyfus, P. M. Chaikin, and J. Brujic. 2013. Specificity, flexibility and valence of DNA bonds guide emulsion architecture. Eur. Biophys. J. Biophys. Lett. 42:S140-S140. Meeting Abstract.

200. Fan, J. A., Y. He, K. Bao, C. H. Wu, J. M. Bao, N. B. Schade, V. N. Manoharan, G. Shvets, P. Nordlander, D. R. Liu, and F. Capasso. 2011. DNA-Enabled Self-Assembly of Plasmonic Nanoclusters. Nano Letters 11(11):4859-4864. Article.

201. Yablonovitch, E. 1993. Photonic Band-Gap Structures. J Opt Soc Am B 10(2):283-295.

202. Hussein, M. I., M. J. Leamy, and M. Ruzzene. 2014. Dynamics of phononic materials and structures: Historical origins, recent progress and future outlook. Appl. Mech. Rev. 66:040802.

203. Zhang, Z. L., and S. C. Glotzer. 2004. Self-assembly of patchy particles. Nano Letters 4(8):1407-1413.

204. Romano, F., E. Sanz, and F. Sciortino. 2010. Phase diagram of a tetrahedral patchy particle model for different interaction ranges. J. Chem. Phys. 132(18):184501-(184501-184509).

205. Romano, F., E. Sanz, and F. Sciortino. 2011. Crystallization of tetrahedral patchy particles in silico. J Chem Phys 134(17):174502. Article.

206. Smallenburg, F., and F. Sciortino. 2013. Liquids more stable than crystals in particles with limited valence and flexible bonds. Nat. Phys. 9(9):554-558. Article.

207. Starr, F. W., and F. Sciortino. 2014. "Crystal-clear" liquid-liquid transition in a tetrahedral fluid. Soft Matter 10(47):9413-9422.

208. Romano, F., and F. Sciortino. 2012. Patterning symmetry in the rational design of colloidal crystals. Nat Commun 3:975.

209. Ye, X., J. Chen, M. E. Irrgang, M. Engel, A. Dong, S. C. Glotzer, and C. B. Murray. 2016. Quasicrystalline nanocrystal superlattice with partial matching rules. Nat. Mater.

210. Dorsaz, N., L. Filion, F. Smallenburg, and D. Frenkel. 2012. Spiers Memorial Lecture: Effect of interaction specificity on the phase behaviour of patchy particles. Faraday Discuss. 159:9-21. Article.

211. Doppelbauer, G., E. G. Noya, E. Bianchi, and G. Kahl. 2012. Competing ordered structures formed by particles with a regular tetrahedral patch decoration. J. Phys.-Condes. Matter 24(28).

212. Noya, E. G., C. Vega, J. P. Doye, and A. A. Louis. 2007. Phase diagram of model anisotropic particles with octahedral symmetry. J Chem Phys 127(5):054501. Article.

213. Rocklin, D. Z., and X. Mao. 2014. Self-assembly of three-dimensional open structures using patchy colloidal particles. Soft matter 10(38):7569-7576.

214. Bianchi, E., G. Doppelbauer, L. Filion, M. Dijkstra, and G. Kahl. 2012. Predicting patchy particle crystals: Variable box shape simulations and evolutionary algorithms. J. Chem. Phys. 136(21).

215. Hynninen, A. P., J. H. J. Thijssen, E. C. M. Vermolen, M. Dijkstra, and A. Van Blaaderen. 2007. Self-assembly route for photonic crystals with a bandgap in the visible region. Nat. Mater. 6:202-205.

216. Avvisati, G., and M. Dijkstra. 2016. Colloidal Laves phases as precursors of photonic crystals. arXiv:1603.07591.

217. Tavares, J. M., L. Rovigatti, and F. Sciortino. 2012. Quantitative description of the self-assembly of patchy particles into chains and rings. J. Chem. Phys. 137(4).

218. Tavares, J., N. G. Almarza, and M. T. da Gama. 2015. Generalization of Wertheim's theory for the assembly of various types of rings. Soft matter 11(29):5828-5838.

219. De Michele, C., T. Bellini, and F. Sciortino. 2012. Self-Assembly of Bifunctional Patchy Particles with Anisotropic Shape into Polymers Chains: Theory, Simulations, and Experiments. Macromolecules 45(2):1090-1106. Article.

220. Fernandez, M. S., V. R. Misko, and F. M. Peeters. 2015. Self-assembly of Janus particles into helices with tunable pitch. Physical Review E 92(4):6. Article.

221. Fejer, S. N., D. Chakrabarti, H. Kusumaatmaja, and D. J. Wales. 2014. Design principles for Bernal spirals and helices with tunable pitch. Nanoscale 6(16):9448-9456.

222. Halverson, J. D., and A. V. Tkachenko. 2013. DNA-programmed mesoscopic architecture. Phys. Rev. E 87(6):062310. Article.

223. Audus, D. J., F. W. Starr, and J. F. Douglas. 2016. Coupling of isotropic and directional interactions and its effect on phase separation and self-assembly. J Chem Phys 144(7):074901. Article.

224. Lindquist, B. A., R. B. Jadrich, D. J. Milliron, and T. M. Truskett. 2016. On the formation of equilibrium gels via a macroscopic bond limitation. J. Chem. Phys. 145(7):12. Article.

225. Roldan-Vargas, S., F. Smallenburg, W. Kob, and F. Sciortino. 2013. Phase diagram of a reentrant gel of patchy particles. J. Chem. Phys. 139(24):12. Article.

226. Russo, J., J. M. Tavares, P. I. C. Teixeira, M. M. T. da Gama, and F. Sciortino. 2011. Re-entrant phase behaviour of network fluids: A patchy particle model with temperature-dependent valence. J. Chem. Phys. 135(3):13. Article.

227. Roldan-Vargas, S., F. Smallenburg, W. Kob, and F. Sciortino. 2013. Gelling by heating. Sci Rep 3:2451. Article.

228. Sciortino, F., and E. Zaccarelli. 2011. Reversible gels of patchy particles. Curr. Opin. Solid State Mat. Sci. 15(6):246-253. Review.

229. Wu, K. T., L. Feng, R. Sha, R. Dreyfus, A. Y. Grosberg, N. C. Seeman, and P. M. Chaikin. 2012. Polygamous particles. Proc Natl Acad Sci U S A 109(46):18731-18736.

230. Zeravcic, Z., V. N. Manoharan, and M. P. Brenner. 2014. Size limits of self-assembled colloidal structures made using specific interactions. Proc. Natl. Acad. Sci. U. S. A. 111(45):15918-15923. Article.

231. Bellini, T., R. Cerbino, and G. Zanchetta. 2011. DNA-based soft phases. Liquid Crystals. Springer, pp. 225-279.

232. Fraccia, T. P., G. P. Smith, L. Bethge, G. Zanchetta, G. Nava, S. Klussmann, N. A. Clark, and T. Bellini. 2016. Liquid Crystal Ordering and Isotropic Gelation in Solutions of Four-Base-Long DNA Oligomers. ACS Nano 10(9):8508-8516.

233. Nakata, M., G. Zanchetta, B. D. Chapman, C. D. Jones, J. O. Cross, R. Pindak, T. Bellini, and N. A. Clark. 2007. End-to-end stacking and liquid crystal condensation of 6–to 20–base pair DNA duplexes. Science 318(5854):1276-1279.

234. Zhang, C., X. Li, C. Tian, G. M. Yu, Y. L. Li, W. Jiang, and C. D. Mao. 2014. DNA Nanocages Swallow Gold Nanoparticles (AuNPs) to Form AuNP@DNA Cage Core-Shell Structures. Acs Nano 8(2):1130-1135. Article.

235. Li, Y. L., Z. Y. Liu, G. M. Yu, W. Jiang, and C. D. Mao. 2015. Self-Assembly of Molecule-like Nanoparticle Clusters Directed by DNA Nanocages. Journal of the American Chemical Society 137(13):4320-4323. Article.

236. Hecht, F. M., and A. R. Bausch. 2016. Kinetically guided colloidal structure formation. Proc. Natl. Acad. Sci. U. S. A. 113(31):8577-8582. Article.

237. Pierrat, S., I. Zins, A. Breivogel, and C. Sonnichsen. 2007. Self-assembly of small gold colloids with functionalized gold nanorods. Nano Lett 7(2):259-263.

238. Ruff, Z., S. H. Nathan, R. R. Unwin, M. Zupkauskas, D. Joshi, G. P. C. Salmond, C. P. Grey, and E. Eiser. 2016. Designing disordered materials using DNA-coated colloids of bacteriophage fd and gold. Faraday Discuss. 186:473-488.

239. Yan, W., L. Xu, C. Xu, W. Ma, H. Kuang, L. Wang, and N. A. Kotov. 2012. Self-assembly of chiral nanoparticle pyramids with strong R/S optical activity. J Am Chem Soc 134(36):15114-15121.

240. Ni, S., J. Leemann, I. Buttinoni, L. Isa, and H. Wolf. 2016. Programmable colloidal molecules from sequential capillarity-assisted particle assembly. Science advances 2(4):e1501779.

241. Désert, A., J. Morele, J.-C. Taveau, O. Lambert, M. Lansalot, E. Bourgeat-Lami, A. Thill, O. Spalla, L. Belloni, and S. Ravaine. 2016. Multipod-like silica/polystyrene clusters. Nanoscale 8(10):5454-5469.

242. Skelhon, T. S., Y. Chen, and S. A. Bon. 2014. Hierarchical self-assembly of 'hard–soft'Janus particles into colloidal molecules and larger supracolloidal structures. Soft Matter 10(39):7730-7735.

243. Wang, Y., Y. Wang, X. Zheng, E. t. Ducrot, M.-G. Lee, G.-R. Yi, M. Weck, and D. J. Pine. 2015. Synthetic strategies toward DNA-coated colloids that crystallize. Journal of the American Chemical Society 137(33):10760-10766.

244. Jones, M. R., R. J. Macfarlane, B. Lee, J. Zhang, K. L. Young, A. J. Senesi, and C. A. Mirkin. 2010. DNA-nanoparticle superlattices formed from anisotropic building blocks. Nat Mater 9(11):913--917.

245. Schreiber, R., I. Santiago, A. Ardavan, and A. J. Turberfield. 2016. Ordering Gold Nanoparticles with DNA Origami Nanoflowers. Acs Nano 10(8):7303-7306. Article.

246. Zheng, X. L., Y. F. Wang, Y. Wang, D. J. Pine, and M. Weck. 2016. Thermal Regulation of Colloidal Materials Architecture through Orthogonal Functionalizable Patchy Particles. Chemistry of Materials 28(11):3984-3989.

247. Joshi, D., D. Bargteil, A. Caciagli, J. Burelbach, Z. Y. Xing, A. S. Nunes, D. E. P. Pinto, N. A. M. Araujo, J. Brujic, and E. Eiser. 2016. Kinetic control of the coverage of oil droplets by DNA-functionalized colloids. Science Advances 2(8).

248. Paik, T., and C. B. Murray. 2013. Shape-directed binary assembly of anisotropic nanoplates: a nanocrystal puzzle with shape-complementary building blocks. Nano Lett 13(6):2952-2956.

249. Colon-Melendez, L., D. J. Beltran-Villegas, G. van Anders, J. Liu, M. Spellings, S. Sacanna, D. J. Pine, S. C. Glotzer, R. G. Larson, and M. J. Solomon. 2015. Binding kinetics of lock and key colloids. J Chem Phys 142(17):174909.

250. Wang, Y., Y. Wang, X. Zheng, G. R. Yi, S. Sacanna, D. J. Pine, and M. Weck. 2014. Three-dimensional lock and key colloids. J Am Chem Soc 136(19):6866-6869.

251. Sacanna, S., W. T. M. Irvine, P. M. Chaikin, and D. J. Pine. 2010. Lock and key colloids. Nature 464(7288):575--578.

252. Sacanna, S., M. Korpics, K. Rodriguez, L. Colon-Melendez, S. H. Kim, D. J. Pine, and G. R. Yi. 2013. Shaping colloids for self-assembly. Nat Commun 4:1688.

253. Vial, S., D. Nykypanchuk, K. G. Yager, A. V. Tkachenko, and O. Gang. 2013. Linear Mesostructures in DNA-Nanorod Self-Assembly. Acs Nano 7(6):5437-5445. Article.

254. Lu, F., K. G. Yager, Y. Zhang, H. Xin, and O. Gang. 2015. Superlattices assembled through shape-induced directional binding. Nat Commun 6:6912. Article.

255. O'Brien, M. N., M. R. Jones, B. Lee, and C. A. Mirkin. 2015. Anisotropic nanoparticle complementarity in DNA-mediated co-crystallization. Nat Mater 14(8):833-839.

256. O'Brien, M. N., M. Girard, H. X. Lin, J. A. Millan, M. Olvera de la Cruz, B. Lee, and C. A. Mirkin. 2016. Exploring the zone of anisotropy and broken symmetries in DNA-mediated nanoparticle crystallization. Proc Natl Acad Sci U S A 113(38):10485-10490.

257. O'Brien, M. N., H. X. Lin, M. Girard, M. O. de la Cruz, and C. A. Mirkin. 2016. Programming Colloidal Crystal Habit with Anisotropic Nanoparticle Building Blocks and DNA Bonds. Journal of the American Chemical Society 138(44):14562-14565.

258. Urban, M. J., P. K. Dutta, P. F. Wang, X. Y. Duan, X. B. Shen, B. Q. Ding, Y. G. Ke, and N. Liu. 2016. Plasmonic Toroidal Metamolecules Assembled by DNA Origami. Journal of the American Chemical Society 138(17):5495-5498. Article.

259. Takabayashi, S., W. P. Klein, C. Onodera, B. Rapp, J. Flores-Estrada, E. Lindau, L. Snowball, J. T. Sam, J. E. Padilla, J. Lee, W. B. Knowlton, E. Graugnard, B. Yurke, W. Kuang, and W. L. Hughes. 2014. High precision and high yield fabrication of dense nanoparticle arrays onto DNA origami at statistically independent binding sites. Nanoscale 6(22):13928-13938.

260. Sharma, J., R. Chhabra, C. S. Andersen, K. V. Gothelf, H. Yan, and Y. Liu. 2008. Toward reliable gold nanoparticle patterning on self-assembled DNA nanoscaffold. J Am Chem Soc 130(25):7820-7821.

261. Zhang, J., Y. Liu, Y. Ke, and H. Yan. 2006. Periodic square-like gold nanoparticle arrays templated by self-assembled 2D DNA Nanogrids on a surface. Nano Lett 6(2):248-251.

262. Woo, S., and P. W. K. Rothemund. 2014. Self-assembly of two-dimensional DNA origami lattices using cation-controlled surface diffusion (vol 5, 4889, 2014). Nature Communications 5.

263. Mohammed, A., L. Velazquez, A. Chisenhall, D. Schiffels, D. Fygenson, and R. Schulman. 2017. Self-assembly of precisely defined DNA nanotube superstructures using DNA origami seeds. Nanoscale.

264. Lin, Q. Y., Z. Y. Li, K. A. Brown, M. N. O'Brien, M. B. Ross, Y. Z. S. Butun, S. Butun, P. C. Chen, G. C. Schatz, V. P. Dravid, K. Aydin, and C. A. Mirkin. 2015. Strong Coupling between Plasmonic Gap Modes and Photonic Lattice Modes in DNA-Assembled Gold Nanocube Arrays. Nano Letters 15(7):4699-4703.

265. Fernandez-Castanon, J., F. Bomboi, L. Rovigatti, M. Zanatta, A. Paciaroni, L. Comez, L. Porcar, C. J. Jafta, G. C. Fadda, T. Bellini, and F. Sciortino. 2016. Small-angle neutron scattering and molecular dynamics structural study of gelling DNA nanostars. J Chem Phys 145(8):084910.

266. Biffi, S., R. Cerbino, F. Bomboi, E. M. Paraboschi, R. Asselta, F. Sciortino, and T. Bellini. 2013. Phase behavior and critical activated dynamics of limited-valence DNA nanostars. Proceedings of the National Academy of Sciences 110(39):15633-15637.

267. Rovigatti, L., F. Smallenburg, F. Romano, and F. Sciortino. 2014. Gels of DNA nanostars never crystallize. ACS nano 8(4):3567-3574.

268. Ke, Y., L. L. Ong, W. M. Shih, and P. Yin. 2012. Three-dimensional structures self-assembled from DNA bricks. Science 338(6111):1177-1183. Article.

269. Jacobs, W. M., and D. Frenkel. 2016. Self-Assembly of Structures with Addressable Complexity. Journal of the American Chemical Society 138(8):2457-2467.

270. Zhu, S., Y. Lu, T. Sinno, and S. L. Diamond. 2016. Dynamics of Thrombin Generation and Flux from Clots during Whole Human Blood Flow over Collagen/Tissue Factor Surfaces. J Biol Chem 291(44):23027-23035. Article.

271. Catuogno, S., C. L. Esposito, and V. de Franciscis. 2016. Aptamer-Mediated Targeted Delivery of Therapeutics: An Update. Pharmaceuticals (Basel) 9(4):69.